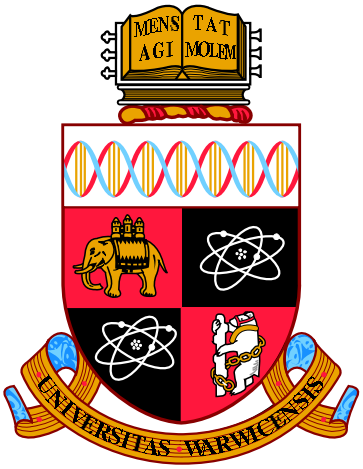

Accreting Neutron Stars and Black Holes

by

Zhuqing Wang

Thesis

Submitted to the University of Warwick

for the degree of

Doctor of Philosophy

Department of Physics

May 2018

THE UNIVERSITY OF WARWICK

"A journey is a person in itself; no two are alike.
And all plans, safeguards, policies and coercion are fruitless.
We find after years of struggle that we do not take a trip; a trip takes us."

John Steinbeck

Contents

List of Tables

List of Figures

Acknowledgments

I would like to take this opportunity to wholeheartedly thank my supervisor, Danny Steeghs, for all his guidance and encouragement throughout this adventure. My gratitude goes also to Prof. Tom Marsh, for making the new softwares available, and for taking the time to answer my additional questions. Without their expertise and constant support, this work would not have been possible.

I would also like to thank my main collaborators: Jorge Casares, Duncan Galloway, Teo Muñoz-Darias, and Felipe Jiménez-Ibarra. It was fantastic to have the opportunity to work with you. Thanks for providing the data that enabled me to carry out the work described here, and most importantly, for all your advice, patience and support.

To my fellow graduate students, Kristine, Chris and James for lots of little talks over the coffee break and sharing your knowledge and experience. To my office mates, Odette, Mark and David for being there whenever I needed advice, companionship, or distractions. With a special mention to Anna, who never fails to cheer me up. Thanks for making every day of work more interesting. I cannot wait to hear about your future adventures!

My special thanks go to all my housemates at #87. Katy & Maria: I miss our interesting chats and all the laughs we had. Lily & Shuwen for your signature cheese cake and fried chicken. Lisa & Rain who inspired me to start my plant-based journey. And Jenna for being a constant source of distraction. Best of luck for the road ahead!

To my dearest friends Aggie and Jessie. Thank you for taking chances and risks, both with me and in your own life.

And finally, to my parents, for everything you've done to inspire me at every stage of my life, for putting up with my anxiety and silliness. Thank you, Dad, for being my greatest cheerleader. And Mum, for being just the way you are. I love you both very much.

Declarations

This thesis is submitted to the University of Warwick in support of my application for the degree of Doctor of Philosophy. It has been composed by myself and has not been submitted in any previous application for any degree. This thesis represents my own work except where stated otherwise.

Part of **Section 3.3** has been published in: Jiménez-Ibarra, F., Muñoz-Darias, T., Wang, L., Casares, J., Mata Sánchez, D. and Steeghs, D. et al.; *Bowen emission from Aquila X-1: evidence for multiple components and constraint on the accretion disc vertical structure*; 2018, Monthly Notices of the Royal Astronomical Society, 474, 4717.

Chapter 4 is based on: Wang L., Steeghs D., Casares J., Charles P. A., Muñoz-Darias T., Marsh T. R., Hynes R. I., O'Brien K.; *System mass constraints for the accreting millisecond pulsar XTE J1814-338 using Bowen fluorescence*; 2017, Monthly Notices of the Royal Astronomical Society, 466, 2261. Observations and reduction of the VLT data were carried out by J. Casares.

Chapter 5 is based on: Wang L., Steeghs D., Galloway D. K., Marsh T. R., Casares J.; *Precision ephemerides for gravitational-wave searches – III. Revised system parameters of Sco X-1*; Monthly Notices of the Royal Astronomical Society, in review.

Abstract

X-ray binary systems offer the best way to measure the masses of the accreting compact objects. Following the discovery of the narrow Bowen emission lines in the prototypical low-mass X-ray binary, Sco X-1, arising from the X-ray illuminated atmosphere of the donor star, the Bowen diagnostic has been used as a general tool to obtain dynamical information for persistent sources and/or transients during outburst. Here I exploit the Doppler tomography technique and develop Monte Carlo style bootstrap tests in order to obtain the most robust binary parameter constraints even in the low signal-to-noise ratio regime. Using a new set of analysis tools, I show that we can push the limit of observations to moderately faint (B $\sim$ 19) persistent sources with 8-m class telescopes.

The method has also been applied to the case of the accreting millisecond X-ray pulsar XTE J1814−338, where the Bowen technique played a crucial role in the derivation of the radial velocity of the secondary, K_2. The resulting constraints on the binary component masses suggest the presence of a 'redback' millisecond pulsar in XTE J1814−338 during an X-ray quiescent state. Sco X-1 remains the most important Bowen blend system for benchmarking our method as well as a critical target for continuous gravitational wave searches. I provide revised constraints on key orbital parameters in direct support of continuous-wave observations of Sco X-1 in the Advanced-LIGO era. In light of the new constraints on orbital parameters, the ranges of search parameters T_0 and P_{orb} should be updated with the refined period and ephemeris. More importantly, the range for the projected semi-major axis ($a_x \sin i$) needs to be expanded in order to cover the full parameter space.

In the last chapter, I present a summary of the method and the key results of its application to all 7 systems (including two transients). The list of Bowen targets can be expanded as new transient outbursts are detected, which may provide us with the opportunities to find stellar-mass black holes. Finally, I remark that the method developed in this thesis can be used to characterize other features in Doppler maps, e.g., the accretion disc and spiral arms.

Abbreviations

ADC ..... Accretion disk corona
AMXP ..... Accreting millisecond X-ray pulsar
BH ..... Black hole
BHC ..... Black hole candidate
CoS ..... Centre of symmetry
CV ..... Cataclysmic variable
CW ..... Continuous-wave
DIM ..... Disc instability model
EOS ..... Equation of states
E-ELT ..... European Extremely Large Telescope
ESO ..... European Southern Observatory
FORS2 ..... FOcal Reducer and low dispersion Spectrograph 2
FWHM ..... Full width half maximum
GTC ..... Gran Telescopio Canarias
GW ..... Gravitational-wave
HJD ..... Heliocentric Julian Date
HMXB ..... High-mass X-ray binary
ISIS ..... Intermediate dispersion Spectrograph and Imaging System
LIGO ..... Laser Interferometer Gravitational–Wave Observatory
LMXB ..... Low-mass X-ray binary
MCMC ..... Markov–chain Monte Carlo
MEM ..... Maximum entropy method
MSP ..... Millisecond pulsar
NIR ..... Near–infrared
NS ..... Neutron star

OSIRIS ..... Optical System for Imaging and low-Intermediate Resolution Integrated Spectroscopy

RLOF ..... Roche-lobe overflow

RV ..... Radial velocity

RXTE ..... Rossi X-ray Timing Explorer

SNR ..... Signal–to–noise ratio

SXT ..... Soft X-ray transient

tMSP ..... Transitional millisecond pulsar

UTC ..... Universal time coordinated

UVES ..... Ultraviolet and Visual Echelle Spectrograph

VLT ..... Very Large Telescope

WHT ..... William Herschel telescope

ZAMS ..... Zero-age main-sequence

Chapter 1

Introduction

Compact objects (white dwarfs, neutron stars and black holes) are the end-products of stellar evolution. A post-main sequence star will evolve to a red giant when its H-exhausted core exceeds the Schönberg-Chandrasekhar limit after a period of Hydrogen shell burning. For stars less massive than $\sim 5\ M_{\odot}$, the stellar core contracts down towards forming a white dwarf when contraction of the core is stopped by electron degeneracy. More massive stars fuse progressively heavier elements until iron builds up in the core and a supernova explosion can be triggered when the mass of the star is greater than the Chandrasekhar limit of $1.44\ M_{\odot}$ (ignoring chemical composition). Once the central density exceeds $\sim 10^{12}$ kg m^{-3}, electrons will combine with protons to form neutrons and neutrinos that are packed very close together. The neutron degeneracy ultimately stops further collapse, and the resulting collection of neutrons will remain as a neutron star. If the remnant of a supernova explosion exceeds 2–3 $M_{\odot}$, even the neutron degeneracy cannot withstand the gravitational force. The core will collapse further towards zero spatial extent, and form a black hole. Since black holes, by their very nature, do not emit electromagnetic radiation, their presence and properties can be best inferred by inspecting the characteristics of a secondary star revolving about an accreting primary in a mass-exchange binary system. In this project, we focus on observational studies of mass-exchanging binary systems where a neutron star or a black hole accretes material from a normal companion star.

1.1 Binaries

1.1.1 Roche geometry

For a binary system with masses M_1 and M_2 and separation a, the Roche potential including the effects of both the gravitational and centrifugal force is given by

$$\Phi(r) = -\frac{GM_1}{|\vec{r} - \vec{r_1}|} - \frac{GM_2}{|\vec{r} - \vec{r_2}|} - \frac{1}{2}(\vec{\omega} \times \vec{r})^2 \tag{1.1}$$

where G is the universal gravitational constant, ω is the angular frequency of the orbit (= $2\pi/\mathrm{P_{orb}}$), and from Kepler's third law, $\omega^2 = \mathrm{G}(M_1+M_2)/a^3$. The dimensionless form of the Roche potential,

$$\Phi_N(x, y, z) = \frac{2}{(1+q)}\frac{1}{r_1} + \frac{2q}{(1+q)}\frac{1}{r_2} + \left(x - \frac{q}{(1+q)}\right)^2 + y^2, \tag{1.2}$$

describes the shape of the potential surfaces, dependent only on the ratio of masses of the two components, $q = M_2/M_1 < 1$. While the binary separation a determines their sizes. Figure 1.1 shows the equipotential surfaces of the Roche potential ($\Phi_R(r)$ = constant) for a binary system with $q = 0.25$. Close to each component, the equipotential surfaces are nearly spherical as the gravitational potential of one of the component is dominant. Further outwards, the combined gravitational influence of M_1 and M_2 distorts the surfaces into teardrop shapes.

There are 5 equilibrium points (L_1 to L_5) where the gravity and the centrifugal force cancel each other out ($\nabla\Phi_R = 0$). The critical surface that envelopes both stars and joins at the inner Lagrangian point L_1 (between the two stars) defines the *Roche lobe* of each star. If one star starts to fill its Roche lobe (and the potential of L_1 is lower than L_3), then matter passing through the L_1-point will move from a region where it is gravitationally bound to M_2 into the gravitational potential well of M_1. This process of transferring mass from one star to the other is called *Roche-lobe overflow* (RLOF). The equivalent radius[1] of the secondary's Roche lobe is approximated (to better than 1%) by

$$\frac{R_{L2}}{a} \cong \frac{0.49q^{2/3}}{0.6q^{2/3} + \ln(1+q^{1/3})}, \quad 0 < q < \infty \tag{1.3}$$

(Eggleton, 1983), valid over the entire range of mass ratios q; or

$$\frac{R_{L2}}{a} \cong 0.462\left(\frac{q}{1+q}\right)^{1/3}, \quad 0.1 \leq q \leq 0.8 \tag{1.4}$$

[1]The circular radius of a sphere which has the same volume as the Roche lobe.

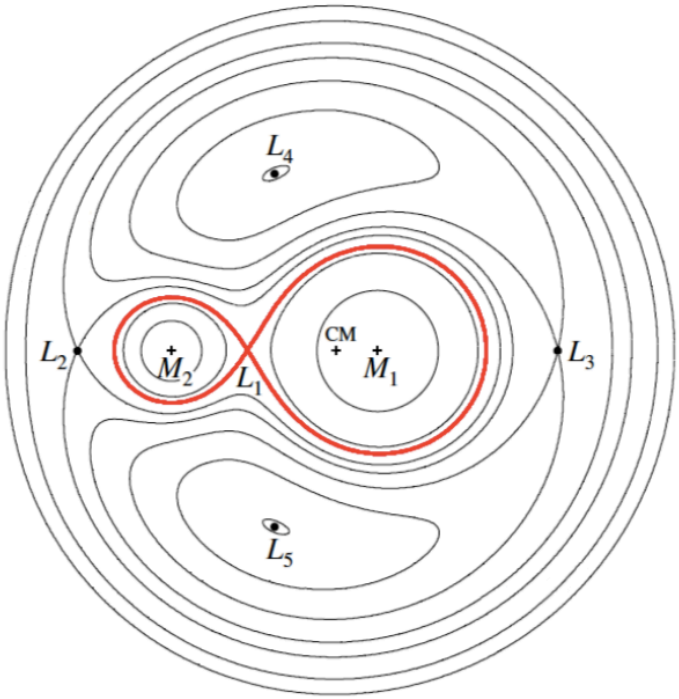

Figure 1.1: Lines of constant gravitational potential for a binary. Indicated are the positions of the primary and the secondary star and the center of mass of the system (CM). The equipotential surface that encloses both stars and intersects at a point L_1 defines the Roche lobe of each star (red). There are 5 equilibrium points ($L_1 - L_5$) where the gravity and the centrifugal force cancel out, and these are known as the Lagrangian points. If star M_2 fills its Roche lobe, a particle passing through the first (or inner) Lagrangian point L_1 will move from a region where it is gravitationally bound to M_2 into the gravitational potential well of the star M_1. Figure from Frank et al. (2002).

(Paczyński, 1971), which is accurate to a few per cent but more convenient than equation (1.3).

1.1.2 Binary evolution

The binary angular momentum J can be expressed as:

$$J = M_1 M_2 \sqrt{\frac{Ga}{M}}, \tag{1.5}$$

where $M = M_1 + M_2$ is the total mass of the system. Differentiating the expression for the angular momentum, the rate of change in the binary separation can be derived as

$$\frac{\dot{a}}{a} = \frac{2\dot{J}}{J} - \frac{2\dot{M}_1}{M_1} - \frac{2\dot{M}_2}{M_2} + \frac{\dot{M}}{M}, \tag{1.6}$$

and dots represent derivative with respect to time. The mass ratio, the orbital separation and the binary period changes during the periods of mass transfer, and stable mass transfer is subject to the balance between the loss of angular momentum, response of the donor to mass loss and changes of separation. Under the assumption that all the mass lost by one star is gained by the other and that the total angular momentum of the system is conserved ($\dot{J} = 0$), equation (1.6) becomes

$$\frac{\dot{a}}{a} = -\frac{2\dot{M}_2}{M_2}(1 - q). \tag{1.7}$$

it is clear that the orbit expands ($\dot{a} > 0$) when $M_2 < M_1$ (and $\dot{M}_2 < 0$) while the binary shrinks when $M_2 > M_1$. Further, using the expression for the secondary's Roche lobe (equation 1.4), the variation of the Roche lobe radius can be derived as:

$$\frac{\dot{R}_L}{R_L} = 2\frac{\dot{J}}{J} + 2\frac{-\dot{M}_2}{M_2}\left(\frac{5}{6} - q\right). \tag{1.8}$$

Thus if $q < 5/6$ (and $\dot{J} = 0$), the size of the secondary's Roche lobe will expand ($\dot{R}_2 > 0$). Sustained and stable mass transfer (which requires that the mass-losing secondary stays in touch with its Roche lobe) is possible if the system shrinks by losing angular momentum.

Three time scales are important for the study of binary evolution. The dynamical time scale over which a star responds to deviations from hydrostatic equilibrium:

$$\tau_{dyn} = \sqrt{\frac{2R^3}{GM}} \tag{1.9}$$

The thermal time scale is the time required for a star with given mass, radius and luminosity

to radiate away its gravitational energy:

$$\tau_{th} = \frac{GM^2}{RL} \tag{1.10}$$

The third time scale is the main sequence lifetime of a star:

$$\tau_{nuc} \approx 7 \times 10^9 \mathrm{yr} \frac{M}{M_\odot} \frac{L_\odot}{L} \tag{1.11}$$

The heavier star evolves more rapidly because the high mass stars have higher core temperatures and thus burn hydrogen more efficiently. Mass transfer will begin with $M_2 > M_1$, and when material is moved further away from the centre of mass, the stellar separation has to be reduced. This decreases the Roche lobe size; the heavier star overfills its Roche lobe even more, driving further mass transfer. As the lower-mass companion is unable to adjust thermally to the accreted mass, the material overfills both Roche lobes. Within the cloud surrounding the binary components, the more massive star and the secondary spiral toward each other, simultaneously expanding and expelling the 'common envelope (CE)'. Steady, long-lived mass transfer can occur when the donor expands to fill the Roche lobe due to stellar evolution; or the orbit, and thus the secondary's Roche lobe, shrinks due to angular momentum loss. There are two main causes of angular momentum loss in a binary: magnetic braking and gravitational radiation.

Magnetic braking

A late-type secondary star filling its Roche lobe in a close binary system is expected to be tidally locked to the orbital period, forcing the star to co-rotate with the orbit. Ionised particles in the stellar wind are forced to follow the magnetic-field lines, and co-rotate with the secondary star. Since these lines are closed near the rotational equator, the particles are mainly released from the stellar poles (with large velocities), essentially extracting angular momentum from the binary orbit, which then shrinks, and the period decreases. A prescription for the angular-momentum loss due to magnetic braking is given by Rappaport et al. (1983):

$$\dot{J}_{MB} = -3.8 \times 10^{-30} M_2 R_\odot^4 \left(\frac{R_2}{R_\odot}\right)^\gamma \Omega^3 \text{ dyne cm}, \tag{1.12}$$

where Ω is the stellar rotational velocity, and the dimensionless γ parameter (from 0 to 4) governs the efficiency of the process.

Gravitational Radiation

As binaries evolve to sufficiently short periods, gravitational radiation becomes a dominant source of angular momentum loss. According to Einstein's general theory of relativity, matter curves space and the orbital motion of a binary system causes ripples in the fabric of space-time. The energy and angular momentum carried by these ripples is extracted from the binary orbit, causing the stars to spiral inwards, hence decreasing the orbital separation and period. General relativity predicts that the rate of angular momentum loss due to the emission of gravitational waves is described by:

$$\dot{J}_{GWR} = -\frac{32}{5}\frac{G^{7/2}}{c^5}\frac{M_1^2 M_2^2 M^{1/2}}{a^{7/2}} \tag{1.13}$$

Paczyński (1967), where c is the speed of light in a vacuum. Dense and compact objects like neutron stars and black holes are strong distorters of space-time, and gravitational waves produced by orbiting pairs of these objects have been observed by the Laser Interferometer Gravitational-Wave Observatory (see Section 1.4).

1.1.3 Accretion discs

If the primary in a *semi-detached* binary ($R_{\star 1} < R_{L1}$ and $R_{\star 2} > R_{L2}$) is a compact object, the stream of gas lost from the companion star, via L_1, does not accrete directly onto the primary. The material will instead go into a circular orbit around it and settle at a distance R_{circ} (the circularization radius), at which the orbiting matter has the same angular momentum as its angular momentum at the L_1 point. Within the ring of gas, several dissipative processes (e.g. collisions, shocks, and viscous dissipation) will take place, converting orbital energy into internal gas energy. Some of the energy is eventually radiated, and the material has to sink deeper into the gravity of the compact object (due to loss of kinetic energy). As the stream spirals inwards, a small amount of gas also moves outwards to conserve angular momentum. An *accretion disc* is then formed. Matter is ultimately accreted onto the primary from the inner layers of the disc. The outward expansion of the disc is disrupted at a maximum radius (r_{tidal}), where tidal interactions with the mass donor removes the angular momentum transported outwards and keeps the disk from overflowing the Roche lobe. For a schematic illustration of the disc formation process by RLOF, see Figure 1 from Verbunt (1982).

The luminosity, L_{acc}, resulting from the accretion can be written as:

$$L_{acc} = \eta \dot{M} c^2, \tag{1.14}$$

where $\eta = GM_1/(R_1 c^2)$ is the efficiency of conversion of the rest mass energy of the accreted

matter into heat for a compact object of mass M_1 and radius R_1, and $\dot{M}$ is the mass accretion rate. The enormous gravitational field of neutron stars and black holes can yield much higher luminosities compared to what white dwarfs can produce from a given amount of in-falling material.

One of the most characteristic phenomena displayed by cataclysmic variables (that have a white dwarf and a normal star companion) and some of the low-mass X-ray binaries (soft X-ray transients; see Section 1.2.1) is the semi-regular outburst where their luminosity increases by several orders of magnitude. However, steady-state accretion flows cannot describe these time-dependent phenomena. Osaki (1974) suggested a cause for the outburst based on an instability in the accretion disc. The rationale is that if the mass transfer rate into the disc from the donor is higher than mass transfer rate through the disc onto the compact primary by viscous interactions, then material would pile up in the disc. For accretion discs with vertical height H, the viscosity is parametrized as

$$\nu = \alpha c_s H, \tag{1.15}$$

where c_s is the sound speed in the gas, and $\alpha \lesssim 1$ denotes the size of the viscosity as a fraction of the limiting case. The pile-up might eventually cause the disc to become unstable, increasing the viscosity and angular-momentum transport, and spreading the excess material both inwards and outwards. The increased accretion onto the compact primary enhances the luminosity of the system and drains the disc of its material. The disc will then return to a quiescent, low-viscosity state. During quiescence, interaction between the gas stream and the disc causes the disc to gradually shrink (since the stream material has angular momentum corresponding to the circularisation radius, which is less than the specific angular momentum at the disc edge) until the next outburst occurs.

Disc instability

The transient behaviour can be understood as the 'limit-cycle' between the surface density and the surface temperature (or equivalently, the accretion rate through the disc) for an annulus of the disc (see Figure 1.2). The S-curve is the line of thermal equilibrium, where the viscous heating balances the radiation from the surface. On the branch with $dT_{eff}/d\Sigma < 0$, for a small positive perturbation of Σ, the annulus would have to seek equilibrium at a lower T_{eff}. However, a small increase in Σ causes an increase in heating and hence a movement away from the curve. Such a region is therefore unstable. In contrast, the branches with $dT_{eff}/d\Sigma > 0$ are stable.

The cycles of quiescence and outburst in soft X-ray transients can be seen as a cycle on the plot of the disc surface density versus disc temperature. During quiescence,

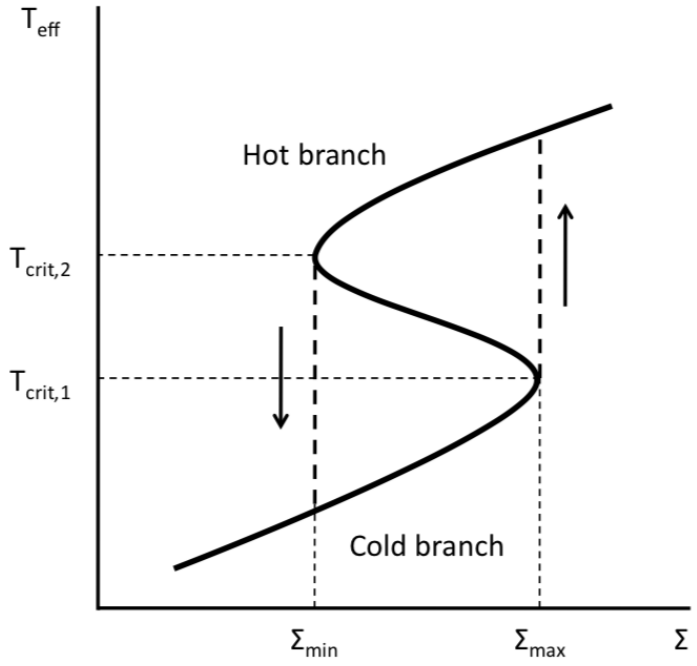

Figure 1.2: A plot of the disc's surface density versus its surface temperature. The S-shaped thermal equilibrium curve forces the disc to follow the limit cycle, see text.

the low-mass X-ray binary lies on the lower branch. However, suppose that the rate of mass transfer arriving at the outer edge of an annulus is greater than $\dot{M}_{crit,1}$, the surface density will increase as the annulus cannot pass mass to inner annuli at the same rate as it receives it. Eventually the disc moves towards the maximum surface density Σ_{max} on the lower branch. At this point, any further rise in Σ produces a runaway rise in temperature. Since the timescale for heating is far shorter than the time for viscous exchange of material, Σ stays constant and the ring heats on a thermal timescale until a new equilibrium on the top branch of the S-curve is reached. Here however, with the condition $\dot{M} < \dot{M}_{crit,2}$, the annulus evolves towards lower T until it reaches the left turning point at Σ_{min}, where T and $\dot{M}$ must adjust on a thermal timescale again, cooling to the lower branch; and the whole cycle repeats.

In fact, an outburst is initiated in one annulus that reaches the critical surface density. The higher viscosity then spreads hot material into neighbouring annuli, sending heating waves inwards and outwards until most of the disc is on the upper branch. The transition into quiescence is triggered when the surface density is reduced to Σ_{min} at some disc ring, which is always in the outer disc (since Σ_{min} is the highest here). This annulus returns to the lower branch; and a cooling wave can propagate inwards, returning the whole disc to quiescence.

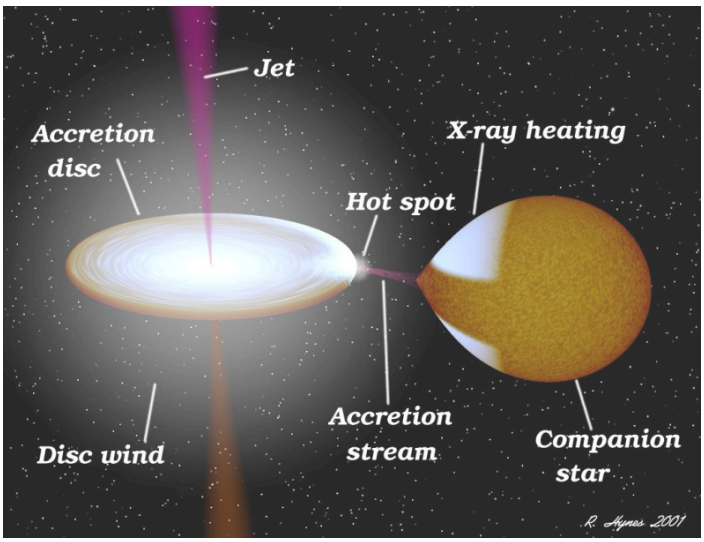

Figure 1.3: An artist's impression of a typical low-mass X-ray binary showing a compact object (either a neutron star or a black hole) accreting matter from a Roche-lobe filling low-mass companion star. (Credit: Rob Hynes).

1.2 Low-mass X-ray binaries

X-ray Binaries have either a neutron star (NS) or black hole (BH) component, and can be separated into two main groups according to properties of the compact object's companion star: high-mass X-ray binaries (HMXBs) and **low-mass X-ray binaries (LMXBs)**, the main topic of this thesis. In high-mass X-ray binaries, the compact object accretes via a strong stellar wind from a massive star ($M_2 \gtrsim 10M_\odot$; usually an O or B type, or a Be type star), driven by the radiation pressure from photons escaping the star.

A low-mass X-ray binary has a low-mass secondary star ($M_2 \lesssim 2M_\odot$; typically with spectral type G, K or M) that evolves to fill its Roche lobe, and transfers matter to the compact object through the L_1 point in the form of a stream. The escaping material carries high angular momentum from the companion and feeds into a circular orbit around the compact object, thereby forming an accretion disc. The production of jets (collimated outflows of accelerated particles) appears to be a common consequence of accretion of material onto a compact object. Where the gas stream impacts the outer edge of the disc a 'bright spot' is formed, radiating away the excess kinetic energy of the stream. Figure 1.3 shows an artist impression of a low-mass X-ray binary.

1.2.1 X-ray transients

LMXBs can be divided into two populations based on their long-term behavior: those that accrete *persistently* at high mass-accretion rates ($L_X \sim 10^{36}$ erg s^{-1}) and the *transient* systems. LMXB transients (often referred to as soft X-ray transients; SXTs) spend most of their lives in a dim quiescent state ($L_X \sim 10^{30}$ – 10^{32} erg s^{-1}), but undergo sporadic outbursts when their X-ray luminosity increases by several orders of magnitude on timescales of days to months (or years), making them indistinguishable from persistent sources.

The sporadic outbursts are thought to be triggered by thermal-viscous instabilities in the accretion disc that leads to an increased mass accretion rate onto the compact accretor (see e.g. Lasota 2001). Dynamical studies have shown that *accreting black holes are mostly found ($\gtrsim$ 70%) in transient LMXBs; whereas persistent LMXBs mostly contain neutron stars*, as implied by the detection of coherent pulsations or bursts. The high incidence of BHs among XRTs is a consequence of the low mass transfer rates expected for their evolved low-mass companions. In BH binaries, the lack of a hard stellar surface in the compact star inhibits disc stabilization through X-ray irradiation (which differs sharply for NS and BH systems) at *low* accretion rates (King et al., 1996, 1997a,b). Thus the transient behavior of dynamical BH candidates (BHCs) appears to provide direct confirmation of the fundamental property of black holes (which is the lack of a material surface). Using a sample of 52 X-ray binaries, it was shown that the Disc Instability Model (DIM) modified by irradiation effects could successfully explain the transient/persistent dichotomy (Coriat et al., 2012).

Transients are discovered during outburst by X-ray or γ ray all-sky monitors such as those on board GRO, *Swift* and XTE. Monitoring of tens of known transients has allowed detailed studies of the spectral and timing properties over the outburst period. During periods of quiescence when the optical brightness decreases by ~ 7 magnitudes, the faint donor star may be entirely responsible for the optical flux. This offers the best opportunity to perform radial velocity studies of the donor, thereby constraining the mass of the compact star (see Section 1.2.5). The main focus of this thesis is the mass measurements for systems in active states, which is possible via the **Bowen fluorescence technique**. We will discuss in later chapters in depth the recent developments of the Bowen technique and the applications to persistent LMXBs and/or transients in outburst to obtain robust dynamical system parameter constraints.

1.2.2 Neutron stars in low-mass X-ray binaries

The Galactic LMXBs have a broad latitude distribution, and are strongly concentrated towards the Galactic bulge; while the distribution of HMXBs are more concentrated towards the Galactic plane. The z-distribution of LMXBs with a black hole candidate was found to

be substantially narrower than that of LMXBs with neutron stars (White & van Paradijs, 1996), indicating that NS systems receive much larger kick velocities (when they are born in a supernova) than BH systems may have obtained. If the NS system remains bound after the supernova kick, a binary with a low-mass companion will receive a larger systemic kick than a binary with a high-mass companion (e.g. Brandt & Podsiadlowski 1995; van Paradijs & White 1995). During their lifetime, the systems with the low-mass companion and a long lifetime ($\sim 10^7 - 10^9$ yr) will travel further away from their birth place (assuming they are born in the Galactic plane) compared to X-ray binaries with a high-mass companion and a much shorter lifetime ($10^5 - 10^7$ yr).

Many NS-LMXBs exhibit type I X-ray bursts due to unstable thermonuclear burning on the surface of the neutron star (Lewin, van Paradijs, & Taam, 1993, 1995). The start of the X-ray burst is extremely rapid, with the X-ray flux increasing by at least an order of magnitude (usually within a second) in all energy bands. This is followed by an exponential decay (due to the cooling of the radiating material), lasting from a few seconds to minutes, and persists for a longer time at lower energies (see Figure 1.4 for example Type I burst profiles).

Swank et al. (1977) noted that for a particular burst the X-ray spectrum was best fitted by a cooling blackbody. Assuming a distance of $\sim$ 5–10 kpc, the blackbody radius required to radiate the observed X-rays in the cooling tail of the burst was estimated to be in the range 10–15 km (consistent with the size of a neutron star). Therefore, the radiation observed during the X-ray burst must arise from the surface of the compact object, which must be a neutron star. As a sufficient amount of hydrogen accretes onto the neutron star, an underlying surface layer of helium will be built up (via nuclear fusion) due to the extreme conditions prevailing. Once a critical density and temperature in the helium layer is reached, it also starts burning (fusing into carbon), giving rise to an explosive thermonuclear flash of X-ray emission. Once the burst is over, the NS continues to accrete fresh hydrogen and re-accumulate the helium layer, and another burst will be generated after a similar amount of time. The recurrence time between the X-ray bursts ranges from hours to days (but occasionally minutes) depending on the mass accretion rate.

Both the detection of type I X-ray bursts and X-ray pulsations can be used as certain ways to distinguish a NS-LMXB from a BH-LMXB. Almost all HMXBs show X-ray pulsations, which indicates that the compact primary in these systems are strongly magnetized NSs. Contrary to the HMXBs, periodic X-ray pulsations are rarely seen in LMXBs. Estimation of the spin of NSs in LMXBs has only been obtained with $\sim$ 15 accreting millisecond pulsars (and some additional burst oscillation sources and kHz QPO sources). No coherent pulsations (or bursts) have been observed so far from the prototypical LMXB source Sco X-1. This is typical behaviour for the family of known bright NS-LMXBs, the so-called

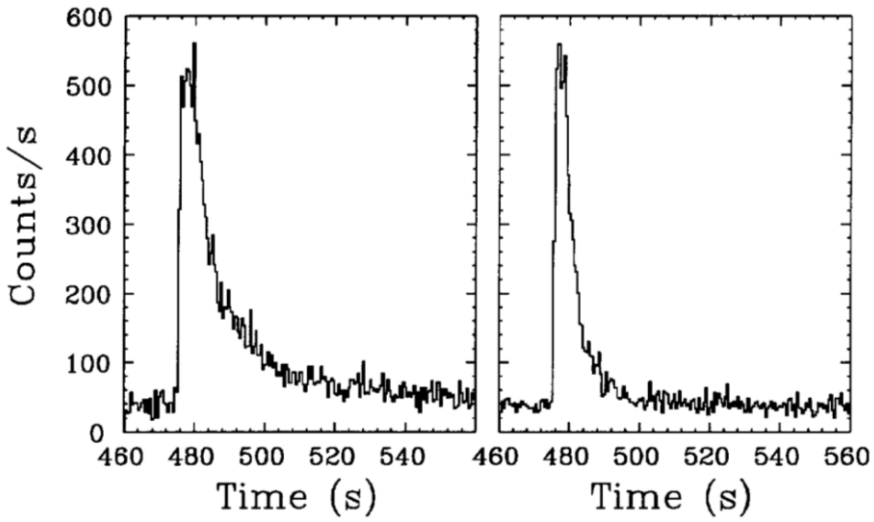

Figure 1.4: (Type I) X-ray burst profiles from 4U 1702−42 observed with EXOSAT in the 1.2–5.3 keV band (*left*) and the 5.3–19.0 keV band (*right*). The burst persists for a longer time at lower energies (it has a cooling tail). Taken from van Paradijs (1998).

'Z-sources' (for the characteristic Z-shaped pattern that the spectral variations trace in the X-ray color-color diagram; Hasinger & van der Klis 1989).

1.2.3 Millisecond pulsars

Figure 1.5 illustrates the evolutionary scenario for the formation of an LMXB, and eventually the formation of a binary millisecond radio pulsar, from an initial binary containing a massive supergiant and a low-mass star ($\lesssim 1\ M_\odot$). Since the radius of the progenitor of the compact object must be much larger than the present size of the LMXB, the system must therefore lose a large amount of angular momentum during its evolution (e.g. Kalogera & Webbink 1998). As described in Section 1.1.2, the more massive star evolves much faster than its companion and is the first to fill its Roche lobe. The mass transfer time scale (dictated by the thermal or dynamical time scale of the supergiant) is considerably shorter than the time scale on which the low-mass companion can adjust thermally to the accreted mass. Consequently, the accreted layer will heat up, and the secondary will expand to fill its Roche lobe, thereby forming a common envelope which engulfs the binary. With the formation of the CE, the secondary rapidly spirals towards the core of the primary due to frictional dissipation. As energy is dissipated in the common envelope, the envelope expands and is eventually ejected from the system. The stripped helium core of the progenitor then undergoes a core-collapse supernova explosion to form a NS primary.

The systems that survive the supernova event can come into contact. The LMXB

phase is initiated when mass starts flowing from the secondary towards the neutron star. Mass transfer is driven either by the expansion of the mass donor or shrinkage of the orbit due to angular momentum loss from the system. Depending on the nature of the secondary, the physical mechanism responsible for angular momentum losses may be magnetic braking and/or gravitational radiation.

Since the discovery of the first millisecond radio pulsar (MSP; Backer et al., 1982), it has been suspected that long periods of mass transfer onto old NSs hosted in LMXBs might be responsible for spinning up the compact object to the ms regime. A 'recycled' MSP is thought to be formed when accretion turns off completely (Alpar et al., 1982). The detection of the first accreting millisecond X-ray pulsar (AMXP) SAX J1808.4-3658 in the course of an X-ray outburst episode (Wijnands & van der Klis, 1998) provided a nice confirmation of the recycling scenario. The radio pulsar/LMXB link was firmly confirmed with more recent discoveries of transitional millisecond pulsar binaries. The most notable examples include the 'missing link pulsar' PSR J1023+0038 that turned on as an MSP after an LMXB phase (Archibald et al., 2009); and the direct evolutionary link IGR J18245-2452, which has shown both an MSP and an AMXP phase (Papitto et al., 2013); and XSS J1227.0-4859 (see, e.g., de Martino et al. 2014; Roy et al. 2015).

The most precise neutron star masses can be determined from several relativistic effects on the pulse arrival times of double NS systems (e.g. Wolszczan 1991; Arzoumanian 1995; Nice et al. 1996). Accurate mass determinations have also been obtained for a few HMXB pulsars from pulse arrival time measurements, combined with RV studies of the massive companion (e.g. van Kerkwijk et al. 1995). However, these methods have certain limitations in the context of finding the maximum NS mass, since the largest mass is expected to be found among MSPs (which have been spun-up through accretion) and NSs in LMXBs – due to sustained episodes of mass accretion. Unfortunately, the relativistic effects that enable precise mass measurements are usually not measurable from these systems (whose orbits are generally circular). Worse still, NSs in LMXBs do not usually pulse, with only a handful of exceptions including X1822-371 and accreting millisecond pulsars. The non-pulsing property has direct consequences for the derivation of binary parameters. For bright NS-LMXBs, we have to rely on optical observations of the companion star to place limits on most of the system parameters (see Chapters 3 and 5). Nevertheless, the groundbreaking discovery has been made with the identification of an extremely high-mass NS PSR J1614-2230 (1.928 ± 0.017 $M_{\odot}$), in a nearly edge-on pulsar binary system, based on detection of the general relativistic Shapiro delay (Demorest et al., 2010). This measurement, along with the subsequent discovery of PSR J0348+0432 (2.01 ± 0.04 $M_{\odot}$; Antoniadis et al. 2013), could eliminate some of the proposed NS matter equations of state (EOSs), and thus provide better constraints on the interior composition of neutron stars

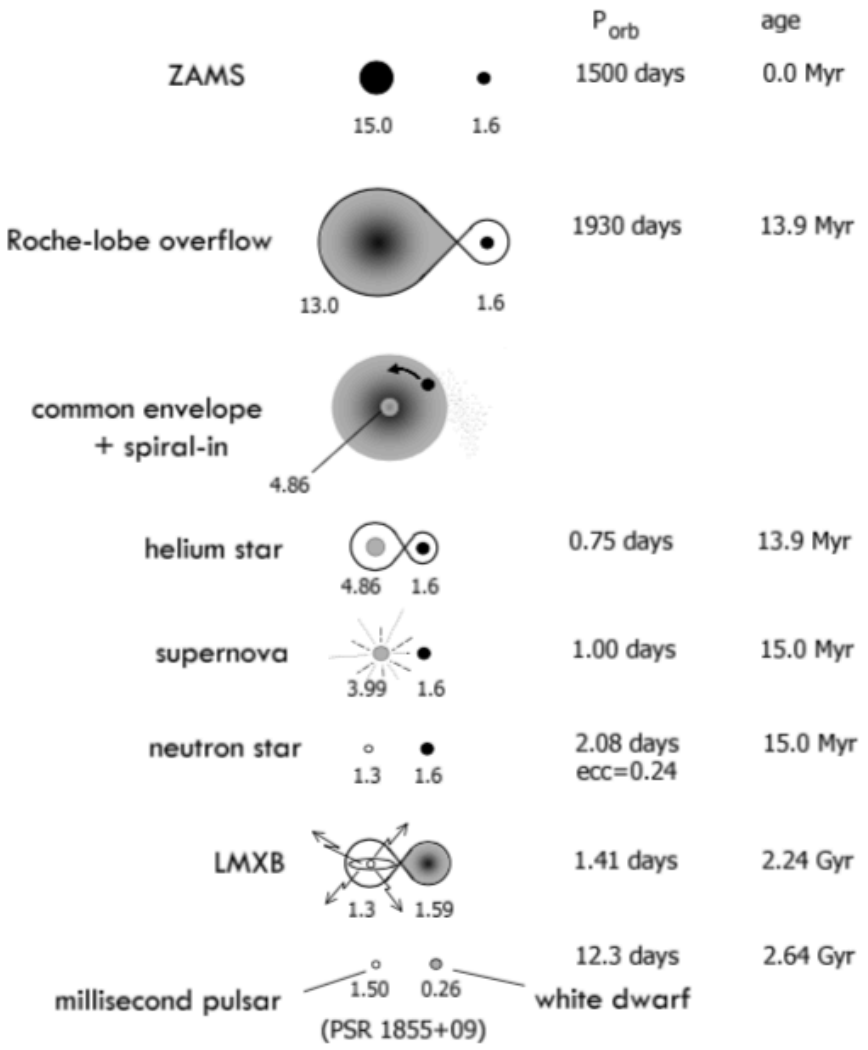

Figure 1.5: A cartoon depicting the evolution of a zero age main sequence (ZAMS) binary system leading to an LMXB and finally the formation of a binary millisecond pulsar. Parameters are given for a scenario leading to the formation of PSR 1855+09. The stellar masses given are in solar units. Taken from Tauris & van den Heuvel (2006).

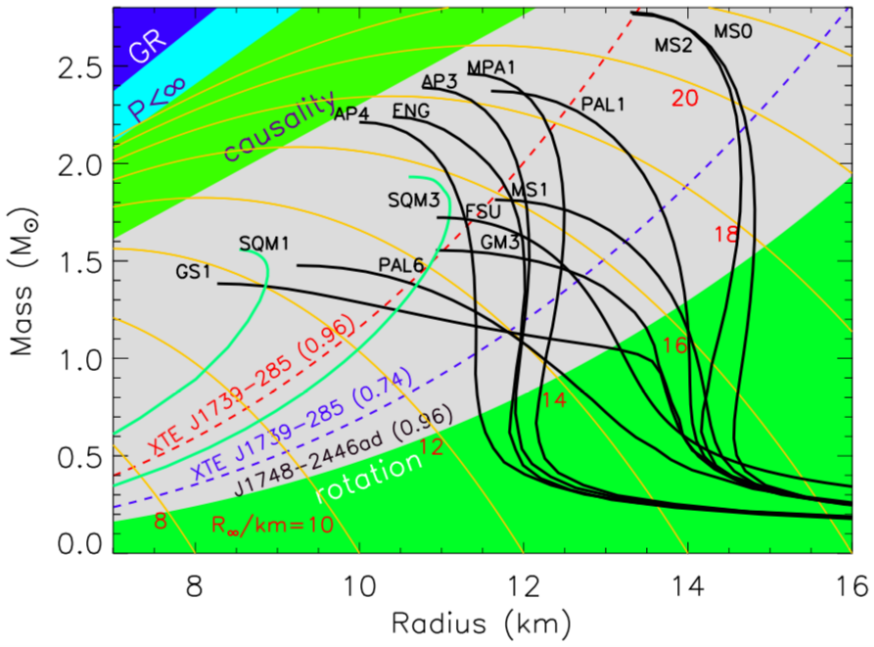

Figure 1.6: Mass-radius curves for neutron stars for typical EOSs (black) and strange quark matter EOSs (green). Taken from Lattimer & Prakash (2007).

(Lattimer & Prakash, 2004, 2007).

Each available equation of state provides a mass-radius relation for a fixed core density (see Figure 1.6), and the maximum possible NS mass (M_{NS}^{max}) is a function of the assumed EOS ($M_{NS}^{max} \sim 1.5\ M_{\odot}$ for *soft* EOSs and up to $\sim 2.7\ M_{\odot}$ for the *stiffest* EOS). Most EOS curves involving exotic particles (that predict a maximum mass well below 2 $M_{\odot}$) are already ruled out. More mass measurements can help reveal even higher mass NSs (see, e.g., the recent constraint by Linares, Shahbaz, & Casares 2018). The effect of rapid rotation can raise the upper limit up to 20% (Friedman et al., 1986). If the mass is greater than $\simeq 3.2\ M_{\odot}$, then a black hole is formed.

1.2.4 Black hole candidates

The most secure way to demonstrate the existence of BHs is provided by dynamical studies of X-ray binaries. Aside from dynamical arguments, there are other observations that can be used to distinguish accreting BHs from NSs. White & Marshall (1984) showed that the two known BH sources, Cyg X-1 and LMC X-3, were located in the extreme upper-left corner in an X-ray colour-colour diagram (see Figure 1.7), i.e., their X-ray spectra were extremely soft. The classic colour-colour diagram of XRBs (when they are bright) shows a clear difference between BHs and NSs in the evolution of their X-ray spectra, due to

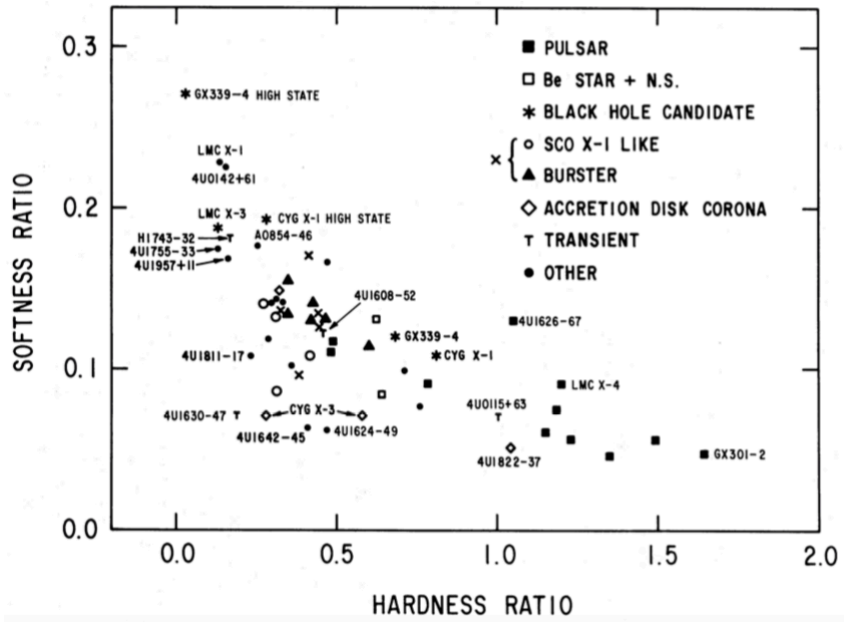

Figure 1.7: An X-ray color-color diagram taken from the High Energy Astronomy Observatory 1 A-2 scanning data. The spectra are averaged over a $\gtrsim 5$ day interval. Cyg X-1 was only observed in the low state; the high-state values were estimated from the high-state spectra given in Sanford et al. (1975).

additional emission from a boundary layer in the NSs (Done & Gierliński, 2003). In spite of the fact that some X-ray spectral characteristics of BHs are also seen in some NSs, the combined presence of these spectral characteristics and rapid variability of the X-ray flux has remained effective in identifying black hole candidates in new transient sources.

Reliable BH masses have been measured in $\sim$ 22 XRBs. These are displayed in Figure 1.8 along with the observed NS masses. The fact that NS masses tend to be higher in LMXBs than in HMXBs could be a manifestation of the pulsar recycling scenario. Neutron stars in HMXBs are less modified by accretion and thus their masses lie closer to the birth values. Figure 1.8 also shows that there is a gap (between $\sim$ 2–5 $M_\odot$) in the current distribution of compact remnant masses (see also Farr et al. 2011). This property contrasts with numerical simulations by Fryer & Kalogera (2001) – including mass loss from stellar winds and binarity effects – which lead to *continuous* model distributions. The discrepancy may be caused by selection effects since low-mass black holes might be hiding among other X-ray sources, although several XRBs (e.g. LS 5039, 4U 1957+115 and GX 339−4) have been reported to contain BHs with masses likely between 2–5$M_\odot$ (Casares et al., 2005; Gomez et al., 2015; Heida et al., 2017). However, on the other hand, if the mass gap is real, it has important implications for core-collapse supernovae models. Belczynski et al. (2012) proposed a theoretical explanation (for the lack of compact objects at $\sim$ 2–5$M_\odot$) that

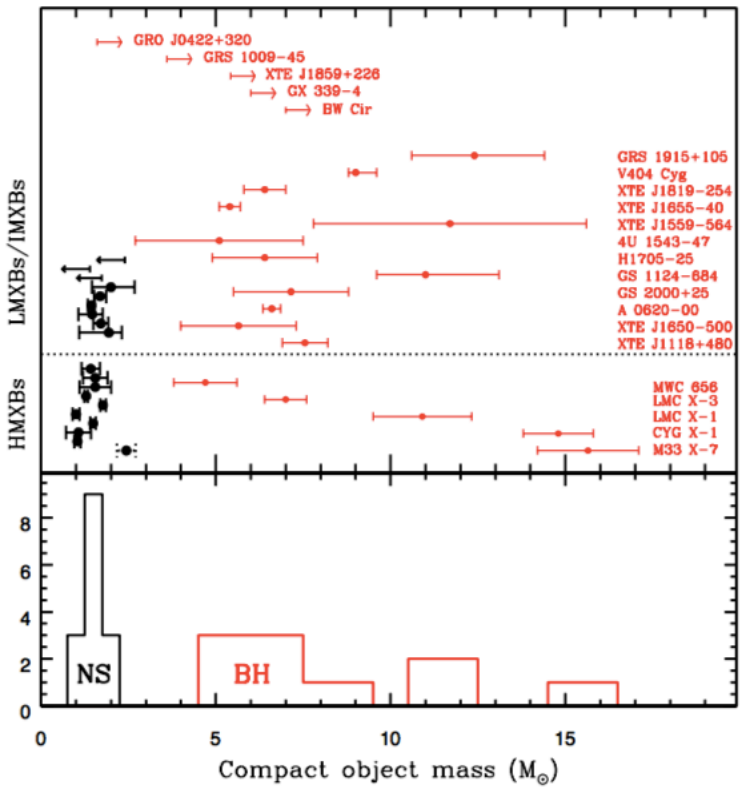

Figure 1.8: Masses of neutron stars (black) and black holes (red) measured in X-ray binaries (*Top*). Observed mass distribution of compact objects in X-ray binaries (*Bottom*). Taken from Casares, Jonker, & Israelian (2017).

depends solely on the growth timescale of the instabilities driving the explosion of massive stars. Instabilities that develop within the first ~ 10–20 ms after the bounce and leads to a rapid explosion within 200 ms of the initial stellar collapse can account for the data. For slower-growing turbulent instabilities, significant fallback is expected and compact objects with masses falling between the observed gap are predicted.

Another main feature of the distribution is that the highest mass BHs ($\gtrsim 15\ M_\odot$) are found only in HMXBs. BH masses in LMXBs are limited to $\sim 12\ M_\odot$ by mass loss from the progenitor after the CE phase, whereas BHs in HMXBs can be formed from more massive stars (especially in low-metallicity environments). Many more observations and secure BH masses are needed before the observed mass spectrum can be used to test models of supernovae explosions and close-binary evolution.

1.2.5 Dynamical mass measurements

With two stars orbiting about the common centre of mass, we have $M_1/M_2 = a_2/a_1$, where M is the stellar mass, a is the distance between the stellar components. As observed at an inclination i, the orbital velocity (K) projected along the line of sight is

$$K_1 = \frac{2\pi a_1}{\mathrm{P_{orb}}} \sin i \quad \text{and} \quad \mathrm{K_2} = \frac{2\pi a_2}{\mathrm{P_{orb}}} \sin i \tag{1.16}$$

for the primary and the secondary star, respectively. Combining equation (1.16) and Kepler's law (and using $a = a_1 \frac{M_1+M_2}{M_2}$), we can obtain the mass function

$$f(M) = \frac{K_2^3 \, \mathrm{P_{orb}}}{2\pi G} = \frac{M_1^3 \sin^3 i}{(M_1 + M_2)^2} = \frac{M_1 \sin^3 i}{(1+q)^2}, \tag{1.17}$$

where $q = M_2/M_1 = K_1/K_2$ is the mass ratio of the binary components. With measurements of the two observables K_2 and $\mathrm{P_{orb}}$, equation (1.17) gives the absolute minimum allowable mass of the compact primary ($\sin i \lesssim 1$ and $1 + q > 1$). Therefore, a mass function in excess of $\sim 3 M_\odot$ (the upper limit of the NS mass for any standard EOS) is widely considered as the best signature for a BH.

When an X-ray transient fades into quiescence (corresponding to the lowest accretion rates), the contribution to the optical light by the accretion disc significantly decreases, which may offer the best opportunity to directly detect the faint low-mass companion and probe its nature. The Doppler shift of narrow absorption lines from the donor (as it moves around the centre-of-mass) provides information about K_2, the absolute phase zero, and the systemic velocity (γ). Figure 1.9 shows an example radial velocity curve of the donor star in V404 Cyg, obtained by cross-correlation of photospheric absorption lines with the rest wavelength spectrum (of a star of similar spectral type to the companion). Spectroscopic analysis during quiescence revealed a K0 companion star of V404 Cyg moving with a velocity amplitude of 211 km $\mathrm{s^{-1}}$ in a 6.5 d orbit. These two parameters alone imply a mass function of $f(\mathrm{M}) = 6.26 \pm 0.31 \; M_\odot$, well above the upper limit of the NS mass. Hence, the compact object *must* be a BH. This result is so remarkable, as it marks the first unambiguous discovery of a stellar mass BH, where no additional assumptions on the inclination nor M_2 need to be invoked.

As mentioned above, the mass function represents only a lower limit to the mass of the compact object, M_1. Precise measurements of the stellar masses also require the mass ratio q and the inclination i to be accurately determined. The companion star transfers matter onto the compact object and hence it must be filling its Roche lobe. In addition, due to the proximity of the binary components, the companion is tidally locked, which makes the absorption lines significantly broader than in single stars that are slowly rotating. The

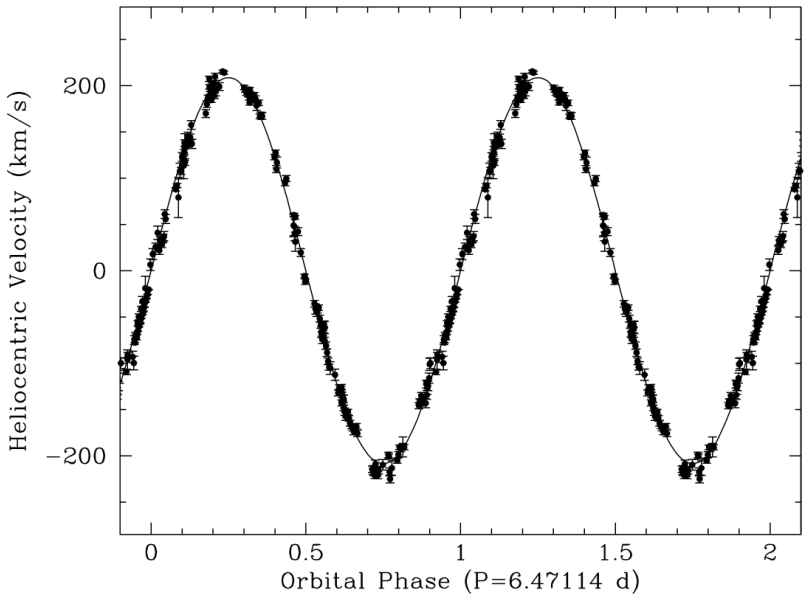

Figure 1.9: Radial velocity curve of the secondary star in V404 Cygni. The radial velocity semi-amplitude $K_2 = 211 \pm 4$ km s^{-1} and the orbital period 6.473 ± 0.001 d yield a mass function of $f(\mathrm{M}) = 6.26 \pm 0.31\ M_\odot$. Adapted from Casares et al. (1992).

ratio of K_2 to the rotational broadening of absorption lines ($\mathrm{V_{rot}sin}i$) can be approximated by a function of q:

$$\frac{\mathrm{V_{rot}\ sin}i}{K_2} \simeq 0.462\,[(1+q)^2 q]^{\frac{1}{3}} \tag{1.18}$$

(Wade & Horne, 1988)[2]. Therefore the usual step towards finding the mass ratio is via the determination of $\mathrm{V_{rot}sin}i$.

The rotational broadening can be measured by comparing the spectrum of the Roche-lobe-filling secondary with that of a slowly rotating single star, and determine the optimal broadening that is required for the template to be matched to the target spectrum (through χ^2 minimization; see e.g. Marsh et al. 1994; Casares & Charles 1994). The rotationally broadened versions of the template are computed by convolution with a limb-darkened rotational profile (Gray, 1992).

Lastly, we need the constraint on i (which can be reliably measured only in eclipsing systems) to calculate the true value of the compact object mass M_1. For a few systems, the binary inclination has been inferred from the orientation of radio jets (e.g. Sco X-1, Fomalont et al. 2001; GRS 1915+105, Steeghs et al. 2013). However, in most cases, the estimation of i relies on indirect methods through modelling of ellipsoidal light curves (in the absence of eclipses; Shahbaz et al. 1994; Orosz & Bailyn 1997; Beer & Podsiadlowski

[2]Assuming spherical geometry for the donor star.

2002). In practice, there are sources of contamination that can seriously distort the true ellipsoidal modulation (e.g. near-quiescence super-hump waves, the hot spot, and flaring activities). Worse still, the cubic dependence of the mass function equation on the inclination angle means that uncertainties on the final mass solution are largely dominated by the errors in i. Thus the search for the relatively rare eclipsing systems (that might be hidden from our view) is needed, in order to obtain more accurate estimates for i and hence M_1.

1.3 The Bowen fluorescence technique

The detection of donor star signatures in many LMXBs has remained difficult for decades. For many systems the companion is too faint to study even during quiescence. Sources with bright optical counterparts tend to be the persistent ones, where the mass accretion rate is high. In these active systems, the optical emission is dominated by the reprocessing of hard X-rays in the outer accretion disc, this obviously hampers direct detection of the much fainter companion. **For persistent LMXBs or transients during outburst, the use of Bowen emission lines – first discovered in the prototypical LMXB Scorpius X-1 – as tracers of the companion's motion provides the only opportunity to constrain their system parameters.**

1.3.1 Detection of the mass donor in Sco X-1

Sco X-1 is one of the brightest optical LMXBs harboring a neutron star that accretes matter from a Roche lobe-filling companion at high accretion rates. Phase-resolved, high-resolution spectroscopy of Sco X-1 led to the first discovery of extremely narrow, high-excitation emission components in the Bowen region (4630-4660Å), mainly consisting of a blend of N III and C III lines. These narrow line features show significant Doppler motions as a function of orbital phase, as can be seen from a 2-D trailed spectrogram (Figure 1.10). Closer inspection of the trailed spectra revealed at least 3 narrow N III/C III components moving in phase with each other, but in anti-phase with respect to the underlying broad component.

The radial velocity (RV) variation of the Bowen emission blend can be derived from multiple-Gaussian fitting to individual spectra, which gives the (common) velocity of the three sharp components and its formal error. The resulting radial velocity curve is shown in Figure 1.11 (*upper panel*), together with that of the He II λ4686 emission line (*lower panel*) based on a double-Gaussian fit.

The extreme narrowness of the sharp Bowen components immediately rules out association with the accretion flow or hot spot (expected to be responsible for broad emission components), and points to the inner Roche lobe of the donor star as the reprocessing site.

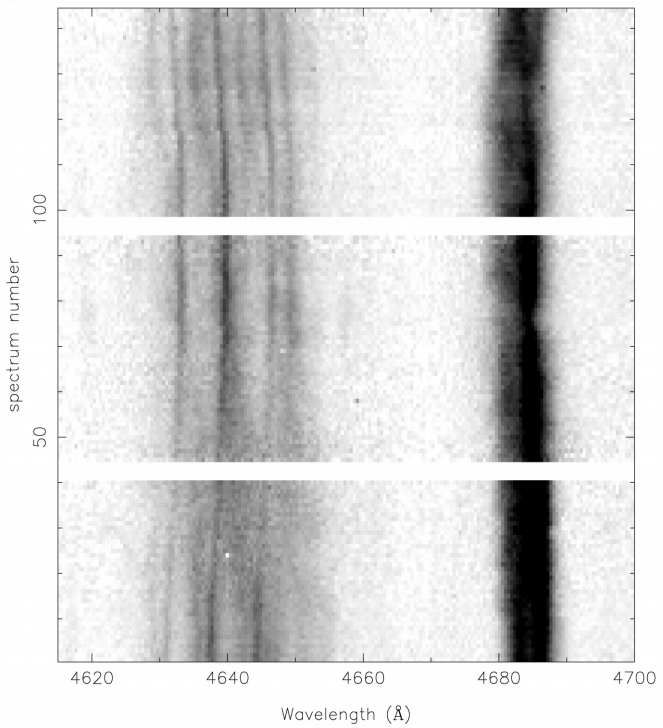

Figure 1.10: Trailed spectrogram of the Bowen blend and He II λ4686 for Sco X-1. At least 3 narrow lines within the broad Bowen region can be seen to be present at all orbital phases. Figure from Steeghs & Casares (2002).

Further support for the hypothesis of donor origin can be drawn from the comparison of the RV curves in Figure 1.11. The blue-to-red crossing point in the RV curve of the narrow lines occurs near the phase of minimum light, at which we face the (un-irradiated) backside of the donor and the visibility of the X-ray heated side of the secondary is minimum. This is therefore the first-ever direct detection of the mass donor in luminous LMXBs. On the other hand, the almost anti-phased line wings of He II emission can be attributed to the accretion flow around the compact object, note that a phase delay of $\sim 0.1 - 0.2$ with respect to the inferior conjunction of the primary is observed in this case (likely due to residual hot spot contamination).

1.3.2 Parameter constraints via the donor signature

A least-squares sinusoidal fit to the RV curve of the Bowen components yields the orbital ephemeris and the radial velocity semi-amplitude of $K_{em} = 77.2 \pm 0.4$ km s^{-1} (Steeghs & Casares 2002). The estimate of the RV semi-amplitude, combined with the inclination derived by Fomalont et al. (2001), provided some of the first binary parameter constraints in Sco X-1, in support of the presence of a 1.4 $M_{\odot}$ neutron star.

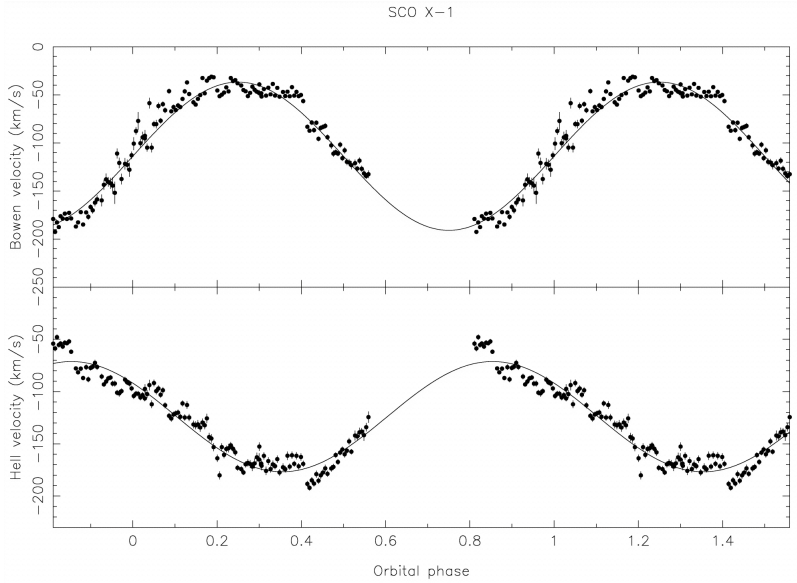

Figure 1.11: Radial velocity curves of the sharp Bowen emission components (*top*) and He II λ4686 emission line (*bottom*). Best-fit sinusoidal waves are overplotted as solid lines. Figure from Steeghs & Casares (2002).

Since we are using emission line diagnostics (instead of the conventional absorption line) and the narrow Bowen components originate from the irradiated front face of the mass donor, the derived K_{em} velocity must be biased towards lower values, i.e., $K_{em} < K_2$ (see e.g. Figure 1.3). In order to transform the measured K_{em} amplitude to the true velocity of the centre of mass of the companion K_2, the so-called **K-correction** needs to be applied to Bowen blend RVs.

By generating synthetic RV curves using simulated emission line profiles formed by (isotropic) radiation on the illuminated hemisphere, the deviation between the reprocessed light centre and the centre of mass of the Roche-lobe-filling donor ($K_{cor} = K_{em}/K_2 < 1$) can be extracted.

Muñoz-Darias et al. (2005) presented numerical solutions for K_{cor} (see Figure 1.12) in their extensive study of K-correction modelling. Their main conclusion is that K-correction depends strongly on:

(i) the mass ratio, $q = M_2/M_1$;

(ii) disc flaring angle, α*, which represents the disc shadowing effect.*

The dependence on the inclination angle i is rather weak. Figure 1.12 plots the K-correction as functions of q for both high- (solid lines) and low-inclination angle cases (dash-dotted lines).

The lower dashed line in Figure 1.12 represents the case where all the emission

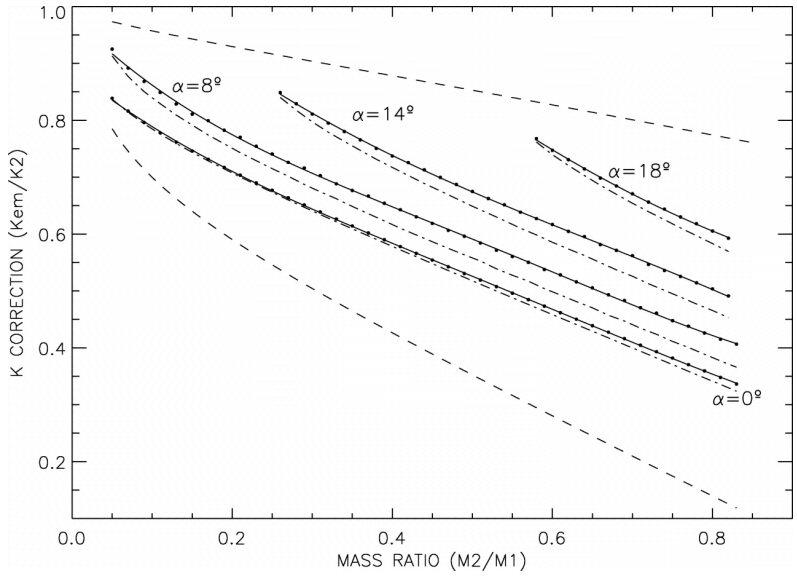

Figure 1.12: K-correction as function of the mass ratio for different disc opening angles. K_{cor} is at the minimum when $\alpha = 0$ (i.e., maximum correction is required), and approaches unity as α increases. Figure from Muñoz-Darias et al. (2005).

is formed at the inner Lagrange point L_1, thus only provides a purely theoretical limit. The K-correction is effectively constrained between $\alpha = 0°$ when disc shielding can be neglected (maximum displacement), and the geometric limit set by emission from the limb of the irradiated region (minimum displacement; upper dashed line). Efforts have been made to obtain knowledge of α (for a system where K_2 is known) from direct spectroscopic measurements and detailed modelling (Jiménez-Ibarra et al., 2018).

1.3.3 The Bowen survey

The discovery of narrow, high-excitation emission lines arising from the (previously unseen) donor star in Sco X-1 opened up a new window to achieving robust RV studies in active LMXBs. Since then, a systematic survey has been conducted in order to search for similar diagnostic features in $\sim$ 20 suitably bright persistent systems and/or transients during outburst (Cornelisse et al., 2008). It turns out that the presence of narrow line features is not peculiar to Sco X-1, but seems to be a common property in the spectra of most of the surveyed sources (see Figure 2 in Cornelisse et al. 2008 and Table 1.1 for a list of candidates with Bowen emission). As we shall see later in Chapters 2 and 3, only in the case of Sco X-1 was it possible to use the conventional RV fitting method to robustly pursue this new avenue for dynamical mass measurements. In all other cases (SNR $<$ 10), the use of the Doppler tomography technique was required to detect Bowen emission from the donor.

Table 1.1: A list of observed optically bright, active low-mass X-ray binaries. Estimates of K_{em} and masses of the accretor were collated from previously published works using the Bowen blend diagnostics.

System	Type	Mag	P_{orb} (hr)	K_{em} (km/s)	M_1 ($M_\odot$)	Reference
Sco X-1	Persistent	B=12.2	18.9	77.2 ± 0.4	> 0.2	Steeghs & Casares (2002)
X1822-371	Persistent	B=15.8	5.6	300 ± 8	1.6–2.3	Casares et al. (2003)
GX 9+9	Persistent	B=16.8	4.2	230 ± 35	> 0.2	Cornelisse et al. (2007b)
V926 Sco	Persistent	B=17.9	4.7	226 ± 22	> 0.5	Casares et al. (2006)
LMC X-2	Persistent	B=18	8.1	351 ± 28	> 0.9	Cornelisse et al. (2007c)
V801 Ara	Persistent	B=18.2	3.8	277 ± 22	> 0.8	Casares et al. (2006)
GR Mus	Persistent	B=19.1	3.9	245 ± 30	1.2–2.6	Barnes et al. (2007)
GX 339−4[a]	Transient	V>21	42.1	317 ± 10	> 6.0	Hynes et al. (2003)
Aql X−1[b]	Transient	V∼22	19.0	247 ± 8	> 1.6	Cornelisse et al. (2007a)
XTE J1814−338[c]	Transient/AMXP	V=23.3	4.2	345 ± 19	> 1	Casares et al. (2004)

Notes.
[a]We note that a recent spectroscopic study of the BH transient GX 339-4 during a quiescent phase (Heida et al., 2017) ruled out the donor star origin of the Bowen emission reported by Hynes et al. (2003).
[b]This result is no longer compatible with the dynamical solution derived from near-infrared spectroscopy taken during the quiescent state (Mata Sánchez et al., 2017). See Section 3.3 and Chapter 6 for more detailed discussions.
[c]Preliminary results.

1.4 Gravitational waves

Over the past two decades, interferometric gravitational-wave (GW) detector technology has dramatically improved and now reached sensitivity levels that are sufficient for direct detection of GWs from astrophysical sources. On February 11, 2016, the first detection of the GW signal (GW150914) emitted from a relativistic in-spiral and merger of two large black holes was reported by the Laser Interferometer Gravitational Wave Observatory (LIGO)[3] and the Virgo[4] collaboration (Abbott et al., 2016), opening a new observational window for studying astrophysical objects. The subsequent detection of a binary neutron star merger (GW170817; Abbott et al. 2017b) confirmed the excitement of detecting GW transients and demonstrated opportunities for discovering new GW source types in the advanced detector era.

It is therefore timely to target also a different GW signal: continuous waves (CWs) emitted by spinning neutron stars in LMXBs that may be detectable in the band of ground-based interferometric observatories. The expectations for CW gravitational radiation from LMXBs arise from the cut-off observed in the spin frequency distribution (of both LMXBs and millisecond radio pulsars) at around 700 Hz, well below the breakup limit (Chakrabarty et al., 2003; Patruno, 2010). Given the estimated ages ($\sim 10^{10}$ yrs) and observed accretion rates of LMXBs, accretion is expected to spin up the NS to at least >1 kHz (for standard NS equations of state; Cook et al. 1994). Thus, there should exist some braking torque to balance the spin-up from accretion. One possibility is the loss of angular momentum through gravitational radiation (Papaloizou & Pringle, 1978; Wagoner, 1984; Bildsten, 1998). If a NS is asymmetric with respect to its rotation axis, it will emit a CW with frequency f at a given ratio with respect to the star rotational frequency ν_s. Different mechanisms were proposed to describe how a small asymmetry in the neutron star might be developed: e.g., crustal mountains ($f = 2\nu_s$; Bildsten 1998; Ushomirsky et al. 2000; Melatos & Payne 2005; Haskell et al. 2006); magnetic deformation ($f = 2\nu_s$; Cutler 2002; Haskell et al. 2008); and internal r-mode oscillations ($f \approx 4/3\nu_s$; Andersson 1998, 2003). Assuming a balance between the accretion torque and the spin-down torque by the GW radiation, the expected GW signal strength at the Earth can be expressed as:

$$h_0 \approx 4 \times 10^{-27} \left(\frac{F_X}{10^{-8}\ \mathrm{erg\,cm^{-2}\,s^{-1}}} \right)^{1/2} \left(\frac{300\ \mathrm{Hz}}{\nu_s} \right)^{1/2}, \tag{1.19}$$

where $h_0 = \Delta L/L$ is the strain, i.e., the fractional change in length of an interferometer arm, and F_X is the incident X-ray flux. Note that the $\nu_s^{-1/2}$ scaling arises only because of the spin-equilibrium assumption; slower rotators ($\nu_s << 300$ Hz) need larger ellipticities for

[3] http://www.ligo.caltech.edu
[4] http://wwwcascina.virgo.infn.it

torque balance (Lasky, 2015). The most promising targets for periodic GW searches are then the brightest sources with the lowest spin frequencies.

Depending upon the *a priori* knowledge of the target source, searches for continuous gravitational waves generally fall into three broad categories: 1) *targeted* searches in which the star's position and rotation frequency are precisely known (e.g., known radio, X-ray or γ-ray pulsars); 2) *directed* searches where the direction of the source is known but little or no frequency information is available (e.g., non-pulsing LMXBs) and 3) *all-sky* searches for unknown neutron stars (Riles, 2017). The volume of parameter space over which to search increases by large steps as one progresses through these categories and, for 2) and 3), any unknown binary orbital parameters (if a star is in a binary system) further increase the search volume. Without accurate determinations of the orbital parameters, an observational 'penalty' must be paid. Effectively, the signal must be proportionately stronger, compared to a source where the parameters are more precisely constrained, in order to reach the same order of confidence for a detection.

Many directed GW searches on known LMXBs have been carried out, mainly focusing on the potentially most luminous source of continuous GW radiation for LIGO and VIRGO, Sco X-1 (Figure 1.13; see also Meadors et al. 2016; Abbott et al. 2017a; Meadors et al. 2017). Since in these cases the source strengths are expected to be small, one must integrate data over long observation times to have any chance of signal detection. So far, only upper limits on the signal amplitude have been obtained (2.3×10^{-25} for Sco X-1; Abbott et al. 2017c). In general, the greater knowledge one has about the source, the more computationally feasible it is to integrate data coherently (preserving phase information) over long observation times. Thus, improvements in the precision of the system parameters of candidate persistent GW sources are essential for reducing the volume of parameter space that needs to be searched, which will contribute to computationally cheaper searches and eventually allowing the use of the most sensitive types of approaches (Messenger et al., 2015).

1.5 Goals of this study

Accurate determinations of binary system parameters, especially the stellar masses, provide key information about the nature of individual components in the system as well as its evolutionary state. Even more significantly, by studying and characterising a large number of objects, we will be able to explore the spatial distribution of these systems and the distributions of key system parameters, thus place constraints on models of binary formation and evolution scenario. In the following chapters, we will study and further develop the proven Bowen fluorescence technique for dynamically deriving robust system parameter estimates

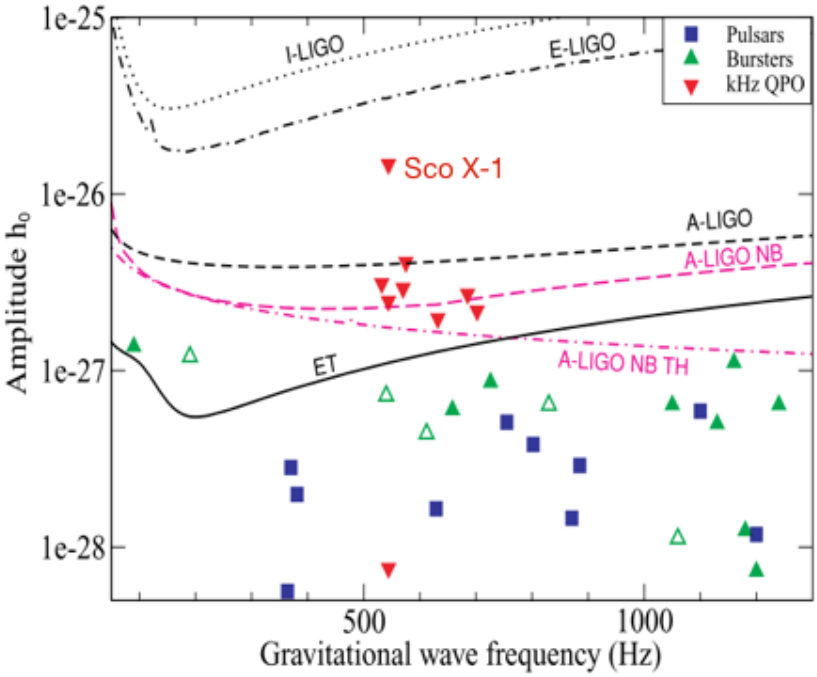

Figure 1.13: Estimates for the gravitational wave strain amplitude (h_0) for a number of known accreting neutron star sources as a function of frequency. The bursters are divided into two groups: those for which the frequency is confirmed (filled) and those for which the frequency requires confirmation (open), see Section 3 of Watts et al. (2008). The detectability thresholds for initial LIGO (I-LIGO), Enhanced LIGO (E-LIGO) and Advanced LIGO (A-LIGO) are also shown. Sco X-1 is by far the only source above the detection threshold for Advanced LIGO broad-band due to its relative proximity to Earth and high mass accretion rate. Figure taken from Watts et al. (2008).

in active LMXBs. Our new analysis toolsets will then be applied to several systems including the 5^{th} accreting millisecond X-ray pulsar XTE J1814-338, which can yield results offering insights into the evolutionary scenario involving binary pulsars. Furthermore, we will continue working to improve the precision of the key orbital parameters of Sco X-1 (our Bowen blend benchmark as well as the prime target for continuous GW searches) required by directed searches for continuous waves.

The rest of this thesis is structured as follows: **Chapter 2** describes the developments of the analysis tools for obtaining dynamical system parameter constraints for Bowen targets. **Chapter 3** presents the (re-)analysis of Bowen datasets using the newly developed Monte Carlo tools and provides updated binary parameter constraints of five LMXBs. In **Chapter 4**, we apply the method to the 5^{th} accreting millisecond X-ray pulsar (AMXP) XTE J1814−338 to establish – for the first time for an AMXP – a complete set of dynamical system parameter constraints. In **Chapter 5**, we return to the Bowen blend benchmark, Sco X-1, and derive revised constraints on key orbital parameters in direct support of GW observations of Sco X-1 in the Advanced-LIGO era.

Chapter 2

Methods

2.1 Data analysis

2.1.1 Radial velocity technique

Line profile fitting

We use the *mgfit* routine within the MOLLY spectral analysis package[1] to fit Gaussian profiles to emission lines in time-resolved, continuum-normalised spectra. The tool allows for a simultaneous fit of multiple lines, and computes the peak height, the FWHM and the offset (relative to the rest wavelengths) of each component following the non-linear least squares fitting technique of Marquardt (1963). Figure 2.1 shows the results of multiple-Gaussian fits to the three strongest narrow lines N III $\lambda\lambda$4634 & 4640Å and C III λ4647 in the Bowen blend of Sco X-1.

It is known that during certain phase ranges, especially near phase zero ϕ_0 (defined as the inferior conjunction of the mass donor), the narrow emission lines from the donor could be much weaker than at other phases. In order to pick up weak features near phase zero (see, e.g., lower panel of 2.1), we can optimize the fitting code to take into account the spectrum-to-spectrum variation. For each spectrum, the expected RV of the narrow lines can be calculated (if the orbital phase is known) and used as the initial fit value of the velocity offset to guide the optimizer to a reasonable optimum (as was implemented to fit both spectra in 2.1). The quality of individual Gaussian fits should also be assessed by visual inspection, especially for spectra taken near the inferior conjunction of the companion.

[1] http://deneb.astro.warwick.ac.uk/phsaap/software

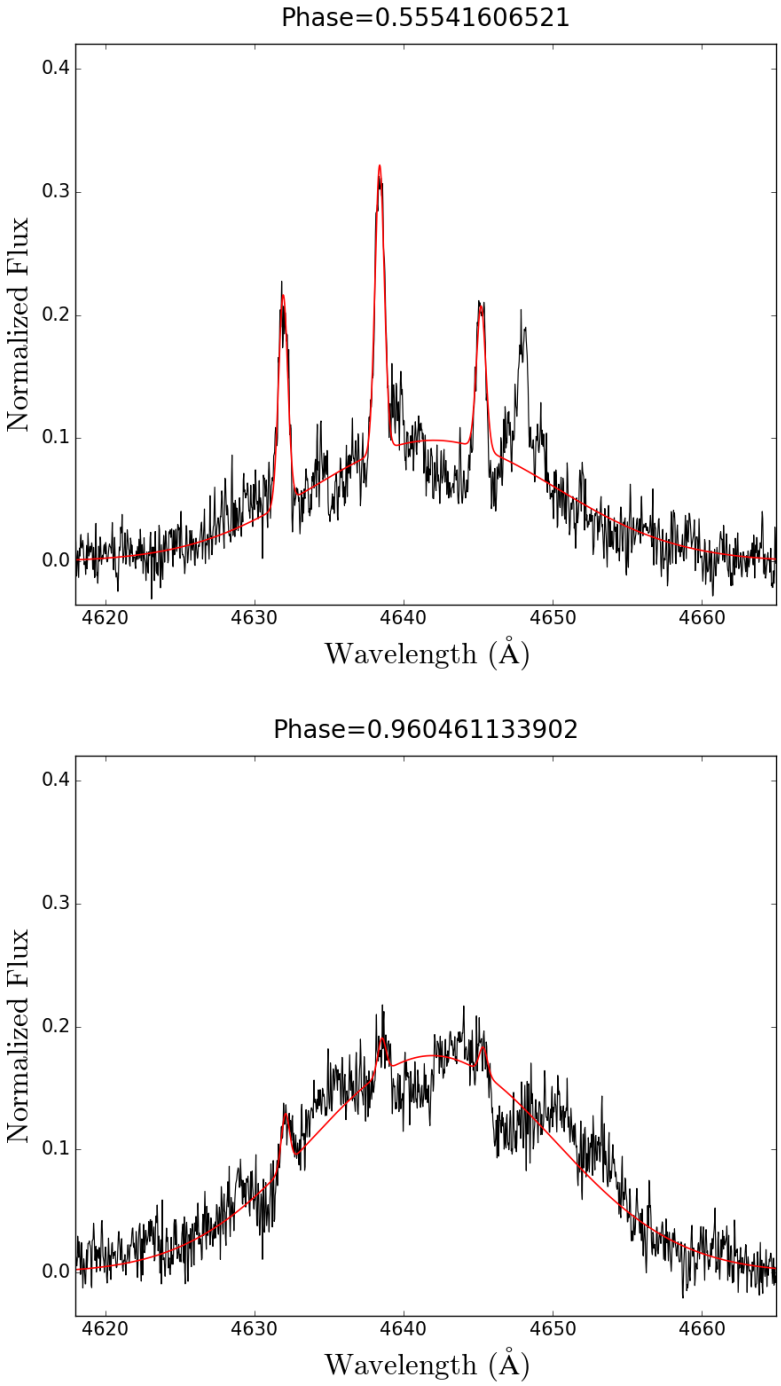

Figure 2.1: Example spectra from the 2011 VLT observations of Sco X-1 at orbital phases $\phi = 0.56$ (*top*) and $\phi = 0.96$ (*bottom*). Multiple Gaussian fits to the N III and C III emission lines are shown in red. Note that the narrow lines are much weaker near phase zero (when we face the un-irradiated side of the donor) than near phase 0.5.

Circular orbit fit

Assuming that the reprocessed light centre traces the orbit of the companion, and that the intrinsic eccentricity of the binary orbit is negligible ($e = 0$), the simplest model for the variation of the projected Bowen RVs is a sinusoid of the form

$$V(t) = \gamma + K \sin\left(\frac{2\pi(t - T_0)}{P_{orb}}\right) = \gamma + K \sin(2\pi(\phi - \phi_0)), \tag{2.1}$$

where γ is the RV of the system (systemic velocity), K is the measured velocity semi-amplitude, T_0 is the epoch of inferior conjunction of the mass donor, P_{orb} is the orbital period (see Figure 1.11 for an example RV curve). To fit the 4 free parameters (T_0, P_{orb}, K, and γ), a least-squares method can be used and each data point is weighted according to the associated error bar given by *mgfit*. This method of extracting orbital parameters is referred to as the RV technique.

The well-established RV method has completely failed in most other cases where the signal-to-noise ratio is low, and the narrow components are too weak to be detectable in individual spectra. In Figure 2.2, we compare the trailed spectrogram of the Bowen blend for Sco X-1 and a fainter source in Table 1.1 (V926 Sco). The narrow 'S-wave' components arising from the heated hemisphere of the donor star can be clearly identified in the exceptional Sco X-1 case, where we have shown the evolution of the Bowen blend as a function of orbital phase. The Bowen region of V926 Sco looks extremely complicated, probably dominated by many weak and blended S-wave features. In a case like this, there might still be genuine signal from the donor. Nonetheless, two outstanding questions remain: 1. *Is there a way to extract* K_{em} *from such noisy datasets?* 2. *(If yes) how do we estimate the statistical uncertainty in the measured* K_{em}*?*

2.1.2 Doppler tomography

The answer to the first question above is yes. To cope with weak emission features, we aim to use all (phase-resolved) spectra *at once*. We also need to be able to separate donor emission from various other sources of emission (these essentially give rise to overlapped/blended sinusoids seen in trailed spectrograms). Fortunately, the technique that matches our needs already exists, and is known as *Doppler tomography*. This powerful mapping technique was originally developed by Marsh & Horne (1988) for recovering accretion structures in cataclysmic variables (CVs). We will first look at the underlying principles of Doppler tomography before moving on to some of the applications to both CVs and LMXBs.

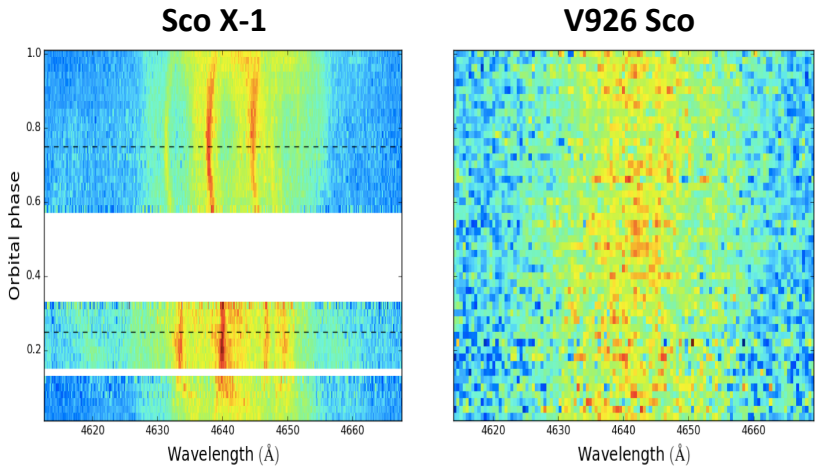

Figure 2.2: Trailed spectrogram of the Bowen blend for Sco X-1 (*left*; all spectra are from 2011 WHT observations of Sco X-1, as presented in Galloway et al. (2014) and V926 Sco (in 50 phase bins; *right*).

The principle

The line profile expected from a simple Keplerian disk is broadened by the large velocities of the emitting gas. The contribution of a particular location is Doppler shifted due to its RV relative to the observer. If Doppler-shifting is the dominant broadening mechanism, all emission from within a region of more-or-less equal RV will contribute to the corresponding part of the velocity-resolved line profile (see Fig. 1 of Marsh & Horne 1988). Hence a spectrum contains information on the integrated flux over the accretion region. Indeed, a line profile observed at a particular orbital phase can be seen as a collapse of the *velocity-space image* of the accretion flow at an angle defined by the phase. Fig. 2.3 gives an example of such an image in velocity space with an artificial spot of emission. From the two line profiles shown in Fig. 2.3, it is easy to locate the position of the spot by tracing back the peaks in the profile along the projection direction. In light of the idea of the CAT-scanning process, it is not hard to imagine that if a sequence of spectra is taken, ideally covering at least a whole orbital period, visualizations of the line-forming region can then be reconstructed in the form of a tomogram in *velocity (or Doppler) coordinates*.

To do this, we begin with a starting image and derive the equivalent trailed spectra. The modelled spectra are then compared against the observed spectra by a χ^2 statistic. In this way, the image can be modified iteratively until the predicted data is consistent with the observed data. The resultant image is given by a *unique* solution that reaches a reasonable goodness-of-fit level (i.e. small χ^2, defined by the user) and occurs with maximum image entropy (i.e. the smoothest reconstruction).

The standard definition of the entropy (S) of an image (I), $S = -\sum p_i \ \ln p_i$, where p_i

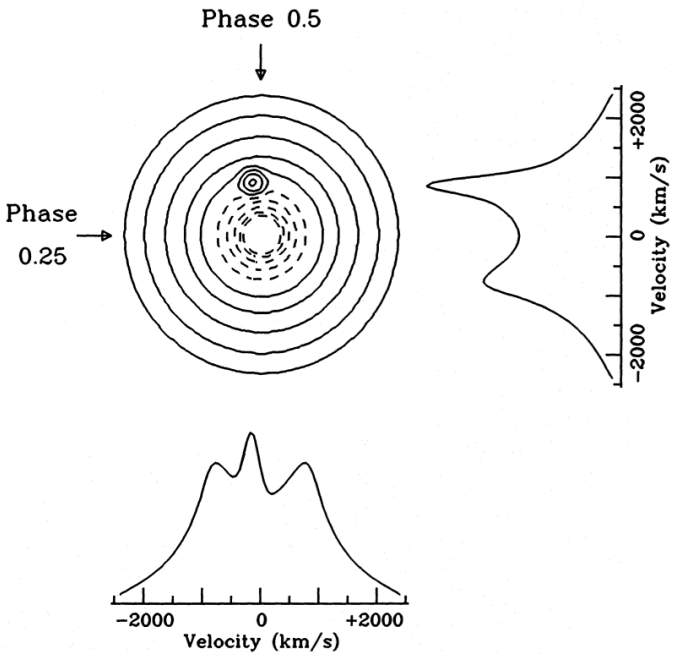

Figure 2.3: Model contour map of the disc in velocity space (i.e. lines of equal radial velocity are straight). The spot is seen to be projected into different parts of the two example profiles at orbital phase 0.25 (*right-most*) and 0.5 (*lower*). The line profile at each orbital phase can then be recognized as the projection of the image along the line of sight. Figure is taken from Marsh & Horne (1988).

$= I_i/\sum_j I_j$, selects the most uniform of all possible images. This could be a problem in the case of the distribution of line emission which is generally a strong function of radius and is far from uniform. Doppler tomography instead uses a modified version of entropy that finds the most axisymmetric distribution consistent with the image, and allows the radial dependence to be determined by the data. The modified version of S is given by

$$S = -\sum_{i=1}^{n} p_i \log \frac{p_i}{q_i}, \quad p_i = \frac{I_i}{\sum_j I_j}, \quad \text{and} \quad q_i = \frac{J_i}{\sum_j J_j}, \tag{2.2}$$

where J is the default image. The default image allows the incorporation of prior information. Both an axisymmetric and a smooth default are possible. A smoothed version constrains only short-scale structure in the image, and is suited to the study of the bright spot region.

The Doppler coordinate system

As a point-like emission source (in the binary system) traces a sinusoidal radial velocity curve (as a function of orbital phase) around the system's mean velocity (γ),

$$V(\phi) = \gamma - V_x cos2\pi\phi + V_y sin2\pi\phi \tag{2.3}$$

this eventually causes an S-shaped pattern (S-wave) that is frequently seen in 2-D trailed spectrograms. Depending upon the phase and amplitude of the S-wave, a *unique* coordinate can be assigned to this point source, expressed by a velocity vector (V_x, V_y), relative to the *inertial* frame. This coordinate system has the advantage that it allows blended S-waves to be mapped into clear and separate features in the velocity space image.

We note that there are good reasons for *not* trying to produce Doppler tomograms in the Cartesian xy-plane, as this would require unjustified assumptions being made (e.g. Keplerian flow in the disc) in order to translate between velocity and position. Worse still, there is often the danger that one point in the system can produce emission at more than one velocity, e.g., the stream-disc impact region. Given the close relationship between the velocity profile of emission lines and the accretion structure in velocity coordinates, we shall restrict ourselves to reconstructing maps in the velocity space. To get a good handle on Doppler maps, one must first get used to this special coordinate system.

In the Doppler coordinate frame, the V_x-axis is conventionally defined by the direction from the accreting compact object to the mass donor, the V_y-axis points in the direction of motion of the donor star, and the centre of mass of the system is at the origin. Based on this definition, we can predict where key components in binary systems would end up in the reconstructed maps.

Understanding the map

Assume the system's mean velocity is zero[2], the centre of mass of the system does not move with respect to the observer, therefore appears on the map at (V_x, V_y) = (0, 0). In the case of the Roche-lobe-filling donor star, which is assumed to be *co-rotating* with the binary ($\boldsymbol{v} = \omega \wedge \boldsymbol{r}$ for 'solid-body' rotation), the transformation preserves the shape of the Roche lobe, but rotates its position to the positive V_y-axis of the tomogram (as the secondary star moves in the positive y-direction by definition). The primary is also on the V_y-axis, but below the origin at (0, -K_1).

A key point to realize is that the familiar picture of the accretion disc in spatial coordinates (Fig. 2.4, *left*) gets turned inside-out in velocity coordinates (Fig. 2.4, *right*).

[2]The systemic velocity is an input parameter to DOPPLER.

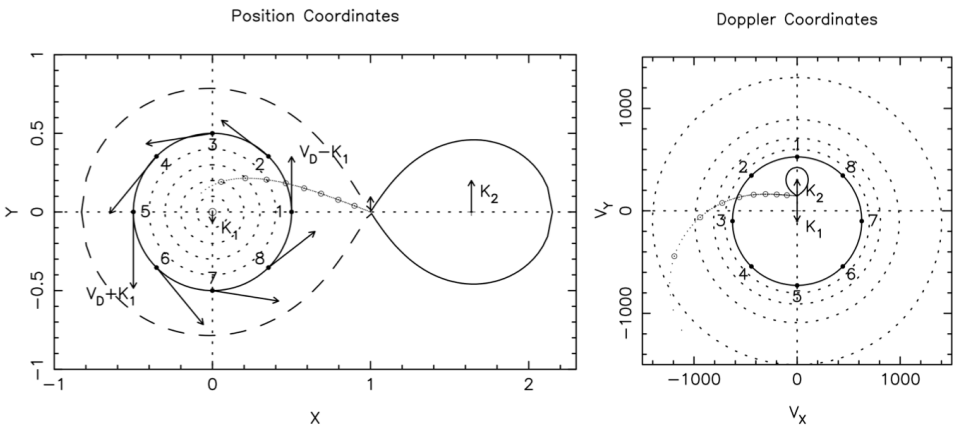

Figure 2.4: Schematic view of a CV in both Doppler coordinates (V_x, V_y) and spatial coordinates in the binary frame (x, y). Major emission sites (including emission from the Roche-lobe-filling secondary star, the mass transfer gas stream and the hot spot at the outer disc) are nicely separated in Doppler maps. Note that the accretion disc in velocity coordinate is turned inside-out, since the inner disc that is closer to the white dwarf should be mapped to higher velocities. From Keith Horne's lecture notes: http://star-www.st-and.ac.uk/ kdh1/pub0/doptom/doptom.html.

Since the inner part of the disc is closer to the central accretor, it will show up in the tomogram as a ring feature (centred on the primary's projected velocity) of radius equal to the large local Kepler velocity. Similarly, the outer edge of the disc is mapped to lower velocities, thus appear closer to the origin in velocity space. Other major emission sites might be traced at an expected position in the reconstruction, including the mass transfer stream leaving the secondary and the bright spot where the gas stream hits the (outer) edge of the disc.

As mentioned before, traditional RV methods of measuring K_2 would fail when dealing with weak features from the donor star in many LMXBs or CV systems. On the other hand, the application of tomography can not only separate various sources of emission nicely in an image in velocity space, but also make weaker contributions easier to be identified by using all observed data at once. This makes Doppler tomography an attractive tool for the derivation of binary system parameters.

2.1.3 Axioms of Doppler Tomography

There are certain assumptions that are required when performing Doppler Tomography.

1. All points are equally visible at all times.

2. The flux from any point fixed in the rotating frame is constant.

3. All motion is parallel to the orbital plane.

4. All velocity vectors rotate with the binary star.

5. The intrinsic width of the profile from any point is negligible.

Exceptions exist to each of these. For example, emission on the mass donor violates axiom (1), and the donor can also obscure the compact object, the accretion disc, and the hotspot. Axiom (2) is violated during a system's outburst. Axiom (3) may be violated in parts of the flow, and the derived maps should then be seen as approximations whereby the flow is projected onto the orbital frame of the binary. Violation of these approximations does not mean the resulting maps are meaningless, but one should be aware of the limitations of the technique when interpreting Doppler maps.

2.1.4 A tomography-based method

If we exploit Doppler maps of emission lines, and find a donor spot at the expected position in the velocity plane (if the absolute phase is known), the apparent RV of the secondary (K_{em}) can be easily extracted from the map through a 2-dimensional Gaussian fit to the spot region.

Work has been done to prove that this tomography-based method does provide valid routes towards orbital parameter estimation. One of the highlights is the detection of donor star emission - for the dwarf nova GW Librae - in the reconstructed map of the Ca II triplet lines. Post-outburst spectroscopy covering the *I* band illustrates the advantages of Ca II relative to the Balmer lines when attempting to constrain system parameters (van Spaandonk et al., 2010). Despite the relative weakness of the Ca II lines, they have a lower ionisation energy (6.1132 eV) than H (13.5984 eV) and He (24.5874 eV), and can be excited by cool sources of radiation ($\sim$ 10 000K). A sharp S-wave (only visible in Ca II) moving *in between* the disc peaks (see van Spaandonk et al., 2010, middle row of figure 6) was mapped to an emission spot in the Ca II λ8662 tomogram (see Fig. 2.5 top right). Since a bright/hot spot emission would have velocities equal to or higher than that of the outer disc edge, a sharp spot seen in this velocity range can be confidently interpreted as an emission component from the irradiated secondary star. With correct ephemerides, the donor emission should always be projected on the map at the position ($V_x = 0$, $V_y = K_{em}$). The coordinate of maximum emission in velocity plane corresponds to a semi-amplitude of $K_{em,\,Ca\,II} = 85$ km s^{-1}. This value was in excellent agreement with the result obtained with line profile fitting ($K_{em,\,RV} = 82.2 \pm 4.9$ km s^{-1}).

For most of the Bowen targets (SNR < 10), Doppler tomography provides the only way to constrain K_{em} (see Table 1.1). Using the K-velocity amplitude derived from

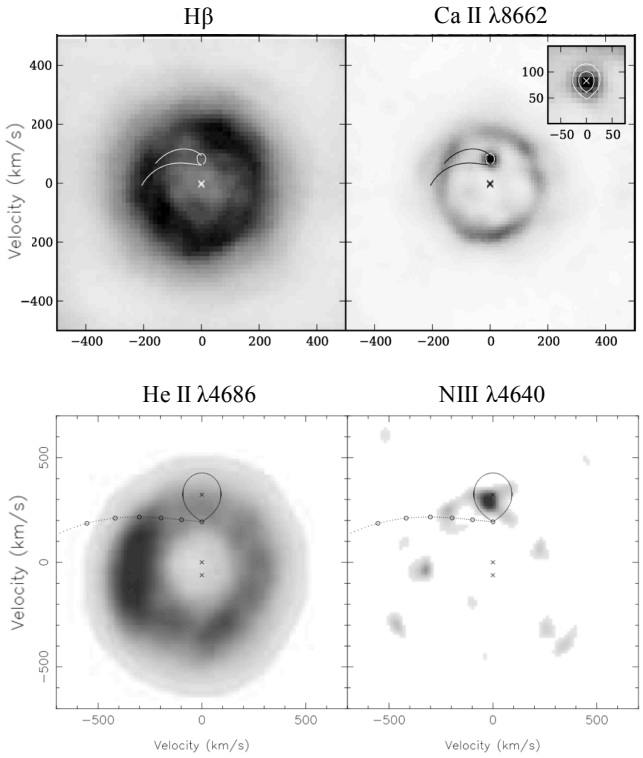

Figure 2.5: Doppler maps of GW Lib (*upper panels*; from van Spaandonk et al. 2010) and the LMXB X1822-371 (*lower panels*; from Casares et al. 2003).

the donor spot, the average Doppler corrected spectra in the rest frame of the donor can be created. In the majority of cases, we see the narrow peaks on top of the underlying broad component appearing to line up with N III and C III lines *only* in the Doppler corrected average. This (and the Sco X-1 work) confirms the reliability of the general methodology that has been applied to LMXBs so far.

Perhaps the most important step towards robust binary parameter estimation using the Bowen technique involves finding the right spot feature in the reconstructed image. This becomes increasingly difficult as we push into lower SNR regimes – for example, it is not uncommon that more than one emission spot can show up in the map; and noise artefacts may also be present as sharp spots. **It is therefore vital to test the reality/significance of a certain feature, which can lead to a decision as to whether any rigorous analysis should be carried out based on the reconstruction.**

In the rest of this chapter we tackle the problem of quantifying the statistical significance of sharp features in Doppler tomograms – this is linked with formal error estimation of quantities (e.g., peak height, K_{em} and full-width half-maximum) determined from map features. The goal is to provide refined diagnostic tools for detecting donor signatures in active LMXBs as well as obtaining the most robust system parameter constraints.

Maximum entropy methods

For maximum entropy based regularised mapping, the user defines a desired goodness-of-fit level (χ^2) of the resultant model. Given data $\vec{x}$ and a default image $\vec{q}$, the Maximum Entropy Method (MEM) finds the *simplest positive image* $\vec{p}$ (among all feasible solutions) that minimizes

$$Q^2 \equiv \chi^2(\vec{x}, \vec{p}) - \alpha S(\vec{p}, \vec{q}), \tag{2.4}$$

where α is a Lagrange multiplier representing the balance between realism (measured by χ^2) and simplicity (measured by the entropy S – Horne 1994). The iteration may begin with a maximum χ^2 at $\alpha = \infty$ (entropy-dominated), iterative corrections are then made to the image as the influence of the data becomes important (α decreases). As the desired χ^2 level is reached, the final iterations will aim to increase entropy to a maximum (for a chosen α), the result of which can be checked by examining the value of

$$\mathrm{TEST} \equiv \frac{1}{2}\left|\frac{\nabla\chi^2}{|\nabla\chi^2|} - \frac{\nabla \mathrm{S}}{|\nabla \mathrm{S}|}\right|^2 \approx 1 - \cos\theta, \tag{2.5}$$

which measures the degree of non-parallelism between $\nabla\chi^2$ and ∇S. For a truly unique maximum-entropy solution, the angle θ between $\nabla\chi^2$ and ∇S should approach zero (Skilling & Bryan, 1984). For linear models, the solution for fixed α is unique (Figure 2.6). One can

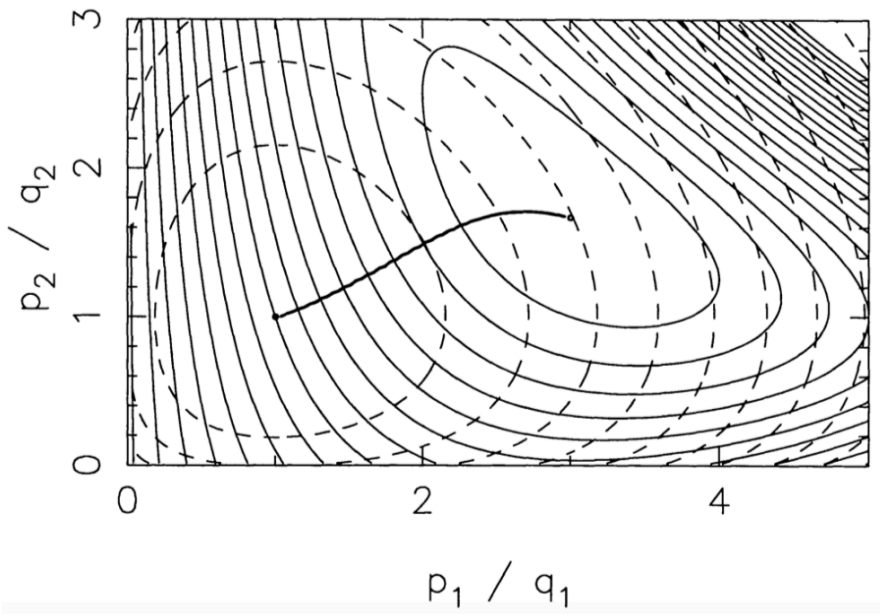

Figure 2.6: The MEM solution for a 2-pixel image. The continuous and dashed lines are contours of χ^2 and entropy, respectively. A trajectory of maximum entropy solutions (parameterized by α) runs from the unconstrained maximum entropy solution ($\alpha = \infty$) to the maximum likelihood solution ($\alpha = 0$). The data constraint confines the solution to be inside the $\chi^2 = C_{\rm aim}$ contour defined by the user. For a chosen α, the MEM solution is unique provided that the χ^2 contours are sufficiently convex. Figure is taken from Horne (1994).

also expect the MEM solution to be well defined in cases of non-linear models. Furthermore, it can be shown that χ^2 decreases monotonically with α until it reaches a minimum at $\alpha = 0$. Thus we can regard χ^2 as an equally valid parameterization of the MEM trajectory, and use the *control parameter* C_{aim} (reduced χ^2 to aim for) to explore a range of solutions. The question is, which value of α (or C_{aim}) should we choose?

Determining optimal goodness-of-fit/entropy level

If we set α too high, the resulting image usually has little structure and fails to fit the data adequately. If we set α too low, we approach the maximum likelihood image, which will attempt to fit noise as well as signal. The detection of weaker emission features can be enhanced in the tomogram by pushing target χ^2 towards low values (i.e., low α), however, this practice at the same time amplifies noise in the image.

It is important to choose an optimal solution, in particular prior to obtaining quantitative measurements using features in the map. One often has to visually examine a range of reconstructions (by changing target χ^2), in order to make a reasonable choice of α, so

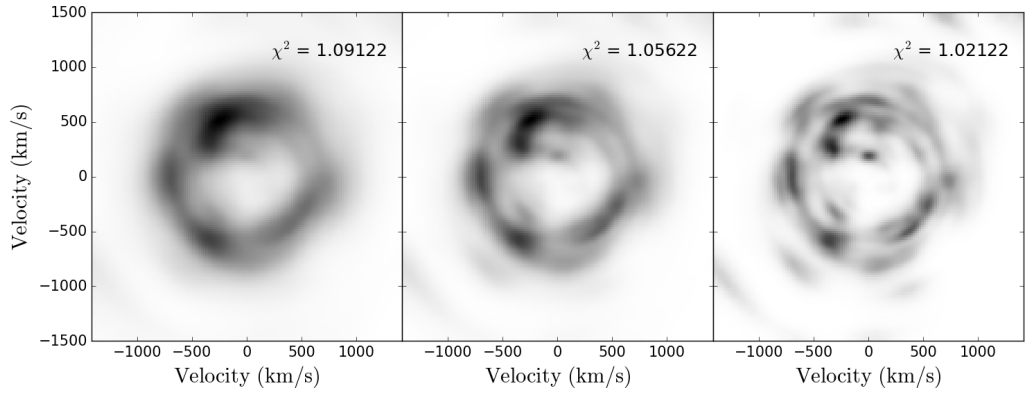

Figure 2.7: Doppler maps of ASAS 0025+1217. A sharp spot feature at the expected position of the companion star emerges (but also the overall map gets noisier) as χ^2 decreases.

that the underlying structure and all emission components can be clearly revealed, without going to the over-fitted regime.

A true feature or an artefact?

In the case of Hγ map for the cataclysmic variable ASAS 0025+1217, the maps corresponding to the lower end of the χ^2 range reveal a sharp emission spot mapped from a weak S-wave (Figure 2.7). It might be tempting to interpret this feature as a secondary star detection (based on its location relative to the disc ring), however, we must caution that the sharp spot only emerges in a subset of all possible solutions, where α is low. It is thus worth questioning whether or not the spot feature is real before using its peak position to infer the RV of the donor.

In order to distinguish real spot features from a noise artefact, we perform tests that make use of a **Monte-Carlo approach**. By generating a large number of synthesized datasets from the original data, simulated images can be computed *in the same manner*[3] as for the original map. The variability from trial to trial can provide a means to statistical uncertainty determination.

Traditional Monte-Carlo techniques require jiggling individual data points around their measured values for generating synthetic datasets. This process makes the often false assumption that we know the error distribution of the measured data and that each data point follows a Gaussian distribution with the standard error. Note that in the cases presented here, neighbouring points may also be correlated due to, e.g., instrumental resolution. After testing on both synthetic and real datasets, we can confirm that 'jiggled' datasets do not represent statistically equivalent datasets to the observed data, as the data values are perturbed

[3]This will be discussed in detail in Section 2.2.1.

yet the error bars remain the same (essentially adding noise to an already noisy manifestation of the underlying data). As our prime purpose is to quantify the *true* significance of a feature, we have instead opted for a method, known as *bootstrapping* (Efron & Tibshirani, 1993).

2.2 Method development

2.2.1 The Bootstrap test

The idea of the bootstrap method is to use the data themselves as an estimator of their underlying parent distribution. By randomly selecting data points from the input spectra (the only sample available to us) with replacements (test 1), a large number of simulated datasets of the same size as the original sample can be generated. To ensure that the true statistics of the data are reflected in the newly generated data and no extra statistical noise is added to each bootstrap dataset, instead of changing values of data points in the trailed spectra, only the error bars of observed data are manipulated. Concretely, based on the output of a random number generator, data points that are selected N times are included in the fit but with errors reduced by a factor of $\sqrt{N}$. Data points that are not selected can be effectively ignored in the fitting procedure by setting their uncertainties to infinity (see details in Watson & Dhillon, 2001).

We also performed tests where we randomly select spectra, rather than data points, so that not all spectra are included for each dataset (test 2). Test 2 has the potential to allow us to identify bad quality data (caused by problems in the reduction, aborted exposure, etc.), by examining the actual combination of spectra for individual bootstrapped maps, especially for the 'outlier' ones. However, test 1 has the advantage that more data points are included in the fitting for each trial, thus provides more reliable error estimates, given that a decent number of bootruns are performed. Therefore it is the test 1 scheme that will feature the rest of the thesis. We note that some issues may still arise with the bootstrapping technique, e.g., there is a finite chance that the bootstrapped spectra contain no useful data (i.e., all the points that are picked lie outside of the lines and in the continuum).

Upon creating a large number of new maps by resampling from the original trailed spectra, histograms of spot parameters can be constructed from ensembles of 2D Gaussian fits. The histograms provide information about the unknown sampling distribution of each property, including the centroid position, peak intensity, and FWHM. We can estimate the mean, the variance and confidence regions for any of these properties based on the bootstrap distribution.

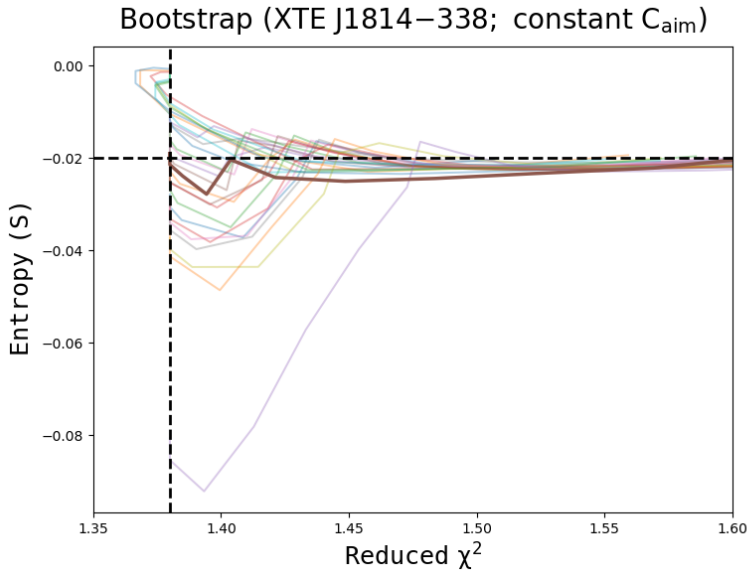

Figure 2.8: χ^2 versus entropy trajectories when fitting the bootstrap datasets to the same χ^2 level (C_{aim} = 1.38) as the original dataset. This strategy resulted in a broad entropy distribution across bootstraps. Brown solid curve represents the trajectory for the original dataset. Coloured curves represent the trajectories for bootstrap datasets.

Monte-Carlo Doppler mapping

We have carefully examined sources of undesirable (random) variations that have high potential to distort the shape of the resulting bootstrap distribution and lead to inaccurate conclusions. While it may seem natural to fit all bootstrap spectra to the same user-defined goodness-of-fit level (χ^2) as the observed spectra, it turns out that for maximum entropy (MEM) Doppler mapping, setting the same reduced χ^2 to aim for can lead to broad entropy distribution across bootstraps, especially in low SNR regimes (e.g. XTE J1814−338, see Figure 2.8). This means that in some cases, the bootstrap map looks simpler or smoother than the original map; in other cases we may end up with much noisier reconstructions, where the code has a hard time to reach the target χ^2 and fits noise as well as signal. This issue can be resolved by iterating all maps towards constant entropy level (S), as suggested in Marsh (2001).

For each inversion, we first construct a smooth map by specifying a high initial value of χ^2, and then decrease C_{aim} in small steps until the corresponding *entropy* reaches the desired value (see Figure 2.9). The grid search is implemented through custom wrapper functions around the second generation (Python/C++ based) DOPPLER routines[4] developed

[4] https://github.com/trmrsh/trm-doppler

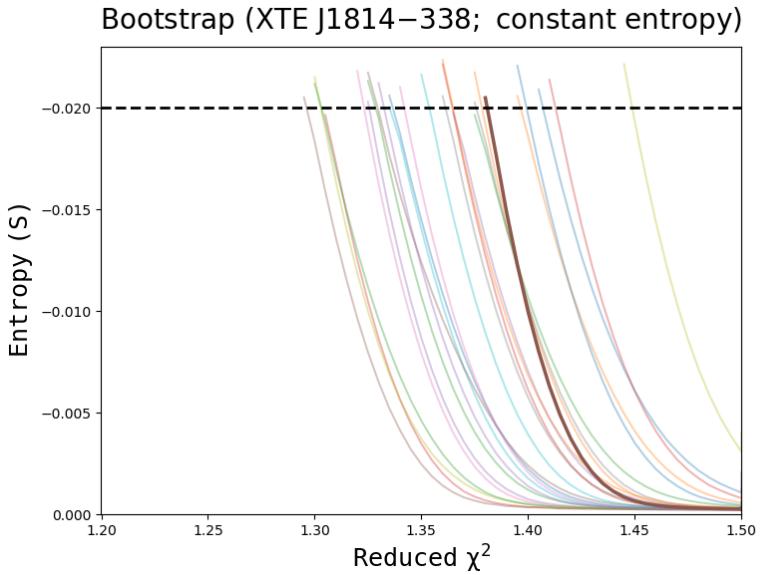

Figure 2.9: χ^2 versus entropy trajectories. All maps were set to reach approximately the same entropy S = −0.02 (horizontal dashed line). Brown solid curve represents the trajectory for the original dataset. Coloured curves represent the trajectories for bootstrap datasets.

by T. Marsh (Manser et al., 2016). One effectively searches for the optimal MEM solution, so that the realism (measured by χ^2) and simplicity (measured by S) can be ideally balanced for all simulated images (see Figure 2.10). Variation can be further reduced by increasing the size of the computational bootstrap (N_B). We have tested that $N_B \gtrsim 2000$ yields robust results within a reasonable time budget (several hours/days of computation). In Figure 2.11, we compare the peak height distribution of the donor spot, determined from 2000 images of J1814, by fitting all bootstrap datasets to the same χ^2 level (magenta) and iterating all maps to the same entropy (grey). This case clearly illustrates that the distribution of the peak emission is severely skewed when aiming for a fixed χ^2, but is perfectly Gaussian (as expected for a Gaussian-type spot) by iterating towards a fixed entropy. In the rest of this thesis, all errors and significance levels are calculated from more than 2000 bootstrap samples with maps iterated to reach the same image entropy.

Significance testing

Figure 2.12 shows the histogram of the emission height of the sharp spot feature in the Hγ map for ASAS 0025+1217 as derived from bootstrap samples. Since the distribution we obtained was Gaussian, we estimated the mean and 1σ error of the emission peak and deduced that the detection is made at only the 1.8σ confidence level (<95% confidence).

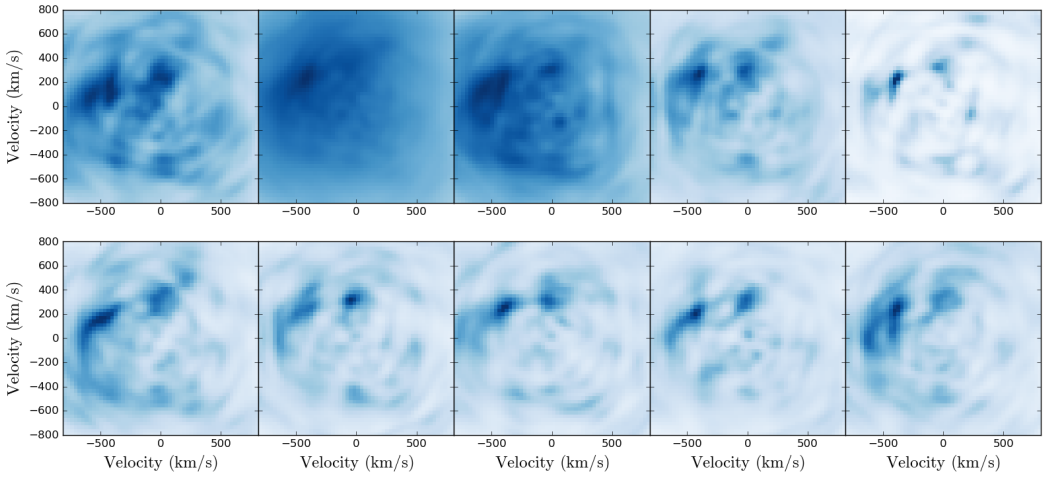

Figure 2.10: Example bootstrap maps of J1814−338 by iterating towards a constant C_{aim} (*top*) and a constant entropy (*bottom*). Setting the same reduced χ^2 to aim for can lead to broad entropy distribution across bootstraps. This issue can be resolved by iterating all maps towards constant entropy level.

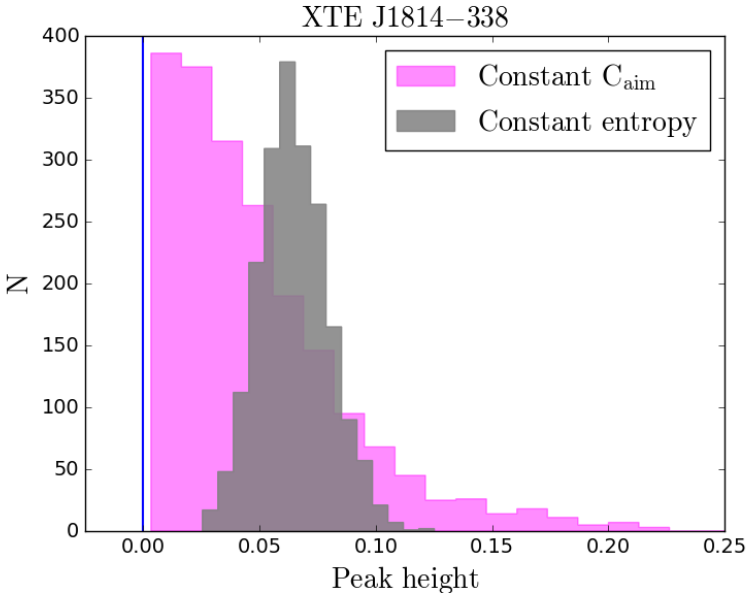

Figure 2.11: Number distribution of the peak height of the donor emission spot determined from 2000 bootstrapped images of J1814. The histogram is severely right-skewed by aiming for the same χ^2, but perfectly Gaussian (as expected for a Gaussian-type spot) by iterating towards a constant entropy (see Section 2.2.1).

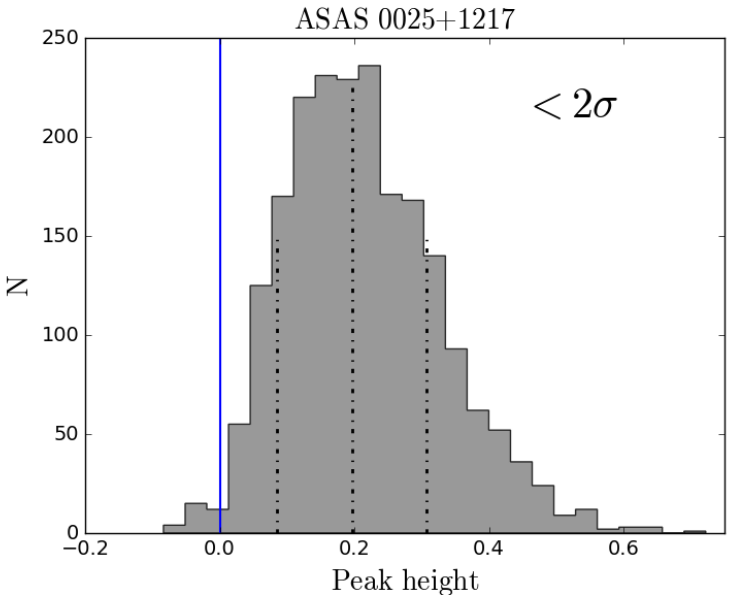

Figure 2.12: Number distribution of the peak height of the potential donor emission spot determined from 2000 bootstrapped images. All maps were set to reach approximately the same entropy S = − 0.0094 (corresponding to a χ^2 value of 1.02122 for the original map). Dashed lines indicate the mean and the ± 1σ confidence intervals. The centre of the peak height distribution is different from zero (blue solid line) at <2σ level, indicating that the detection is not significant.

Clearly more data is needed to confirm the donor signature in ASAS 0025+1217.

To validate that the bootstrap method developed above behaves correctly, we performed extensive tests (Chapter 3) using Bowen datasets of LMXBs spanning a range of S/N (see Cornelisse et al. 2008; Fig. 2). To suppress the noise and enhance signal strength, in all cases we created (combined) Bowen Doppler maps by assigning multiple Bowen emission lines to the same image. In Figure 2.13, we show the χ^2 distributions – for the bootstrap technique and the traditional Monte Carlo perturbation – across bootstraps for two data sets. The upper panel is for the XTE J1814 data (see Table 1.1), the lower panel for the much higher SNR data of our Bowen blend benchmark Sco X-1. These show that datasets generated via Monte Carlo perturbation deliver a significantly worse goodness-of-fit level compared to the original dataset (vertical dashed line), whereas bootstrap samples remain close to the original goodness-of-fit.

As discussed above, the disadvantage of Monte Carlo perturbation is that one needs to make explicit assumptions on both the type of error distribution (e.g. Gaussian) as well as the correct amplitude (correct 1σ error bars on all data points). It assumes that the statistical error bars of the data describe all sources of uncertainty, which is often not the case for real

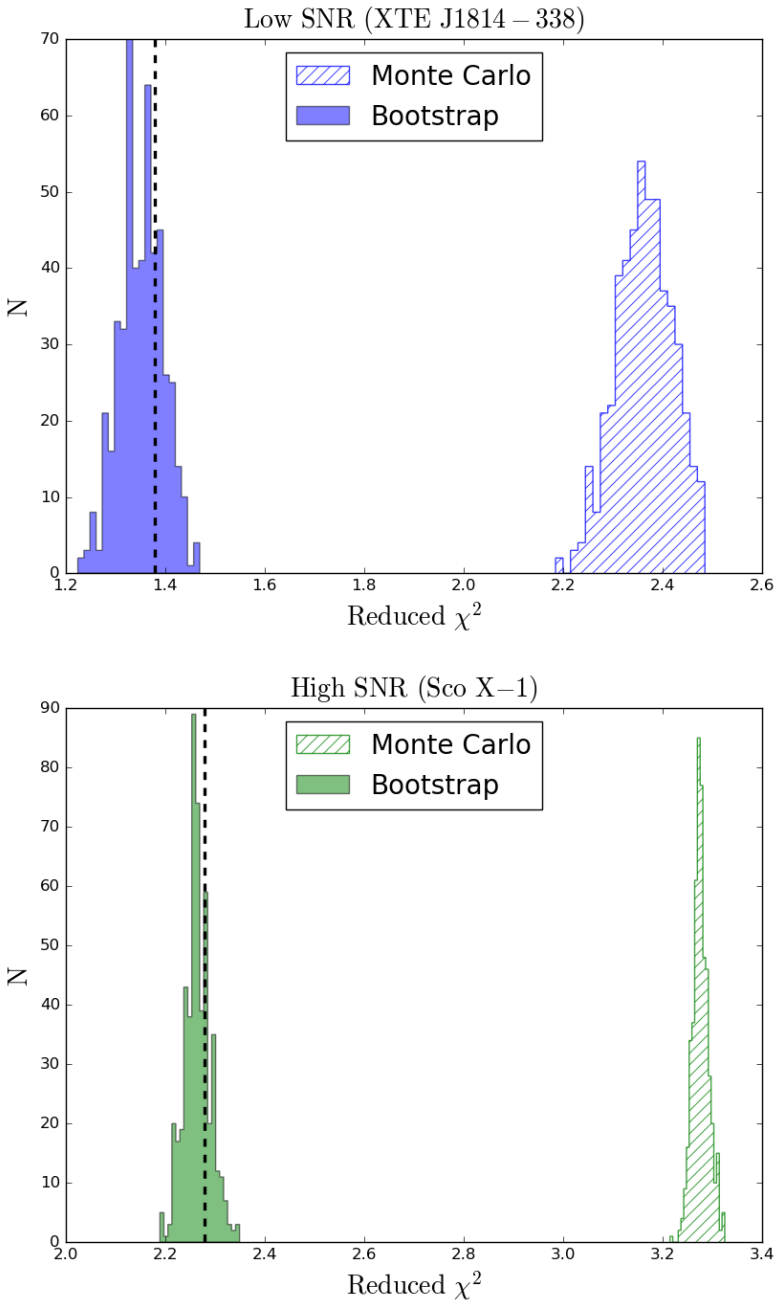

Figure 2.13: Distribution of the goodness-of-fit level of synthetic maps. Vertical dashed lines indicate the χ^2 level of the original map at the same entropy.

datasets. On the other hand, the bootstrap method avoids these assumptions, instead relying on the idea that the observed data itself encodes information about its error distribution. Since the bootstrap has minimum assumptions that hold more generally, we believe that the essential statistical features of the original data are better preserved in our bootstrap samples, and this is clearly reflected in Figure 2.13.

We also estimated the significance of promising donor features present in the Bowen Doppler maps of XTE J1814 and Sco X-1 (Chapters 4 and 5). For the relatively low SNR case of XTE J1814, the photon noise dominates and the two resampling methods deliver very similar significance levels (4.2σ). However, the implied statistical error on the velocity amplitude K_{em} was reduced (from 29 km s^{-1} to 21 km s^{-1}) by implementing the Monte-Carlo method. In the high SNR case of Sco X-1, we would deduce much higher apparent significance values compared to the bootstrap (109σ vs. 58σ) and also a greatly reduced velocity uncertainty on K_{em} (0.2 km s^{-1} vs. 0.8 km s^{-1}). **The parameter uncertainties extracted from the bootstrap series are thus more conservative and more robust against SNR.** This can be explained by the fact that the bootstrap samples allow us to test for contributions that are not captured by the formal error bar spectrum (e.g., contaminating spurious signals, flares, etc.).

2.2.2 Bowen diagnostic diagram

If the input γ parameter to DOPPLER (the systemic velocity parameter) is set to the true RV of the system, then one would obtain an optimally sharp image [note that the origin at (V_x , V_y) = (0, 0) corresponds to the centre of mass of the system]. On the other hand, an incorrect choice of γ often leads to poorer reconstructions, and spot features in particular would appear misplaced and out-of-focus in such an image (see Figure 2.14). Thus, the detection of donor emission provides the opportunity to study the reconstructions as a function of the assumed systemic velocity.

In the case of Sco X-1, where γ can be accurately determined using the RV fitting technique ($\gamma = -113.6 \pm 0.2$ km s^{-1}), Figure 2.14 shows that the correct value of γ yields indeed the most compact donor feature. By running the bootstrap test using a range of γ values in steps of 2 km s^{-1} (centered on -113.6 km s^{-1}), it can be shown that the maximum significance of the donor feature occurs at the value of γ estimated from the RV technique (Figure 2.15). **We can therefore expect that the best estimate for γ would yield the maximum significance of the donor feature.** Furthermore, the derived K_{em} velocity showed a small range of variation within a reasonable range of the target γ values (which yielded a $>50\sigma$ donor detection), indicating the presence of small systematic errors on K_{em} due to the uncertainty in γ. Based on the above results, we obtain

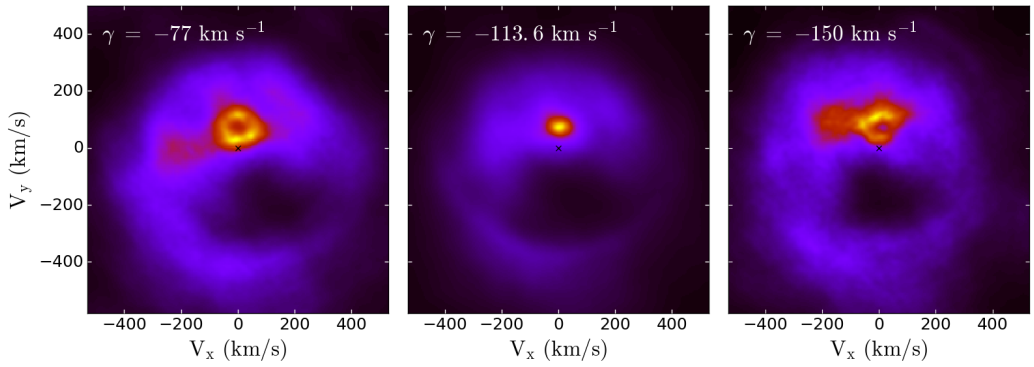

Figure 2.14: Bowen Doppler images of Sco X-1 for an assumed γ parameter of -77 km s^{-1} (*left*), -113.6 km s^{-1} (*middle*) and -150 km s^{-1} (*right*). Only the correct value of γ (estimated from the RV technique) yields an optimal reconstruction (*middle*) with a sharp donor emission spot at the right position in the map.

$$K_{em,\,doppler} = 75.0 \pm 0.8\ (stat) \pm 0.6\ (sys)\ km\ s^{-1},$$

in excellent agreement with the K_{em} amplitude derived from the traditional RV fitting method ($K_{em,\,RV} = 74.8 \pm 0.4$ km s^{-1}; see Chapter 5).

In the cases where γ is unknown, a 'diagnostic diagram' (similar to that displayed in Figure 2.15) can be exploited to evaluate the optimal γ solution and any systematic uncertainties on the derived RV semi-amplitude. More applications of the bootstrap method as well as example diagnostic diagrams can be found in Chapters 3 and 4.

2.2.3 Monte-Carlo binary parameter calculations

The detection of Bowen emission lines opens up a special opportunity to constrain the radial velocity of the companion star (K_2), and thereby the mass of the compact object (M_1) via the mass function equation (Eq 1.17). The main caveat is that the narrow lines are produced on the irradiated inner hemisphere of the secondary, instead of the entire Roche lobe; hence the previously determined K_{em} amplitude represents only a lower limit to the true, centre-of-mass velocity of the companion, K_2. Therefore a 'K-correction' must be applied to the observed K_{em} when performing binary parameter calculations.

In order to arrive at the most reliable estimation of true K_2, we developed new tools to extend the numerical solutions for the K-correction (originally provided in Muñoz-Darias et al. 2005) to a set of fast K-correction models covering all disc flaring angle (α) values typical of XRBs. By interpolating over the grid of K-correction functions for α from 0 to 18° (in steps of 2°; see Table 1 in Muñoz-Darias et al. 2005), we can generate reasonable model K-corrections as functions of q for any arbitrary disc opening angle within the given bounds (Figure 2.16). The best fitting polynomial, $K_{cor} = \frac{K_{em}}{K_2} \cong N_0 + N_1 q + N_2 q^2 + N_3 q^3 +$

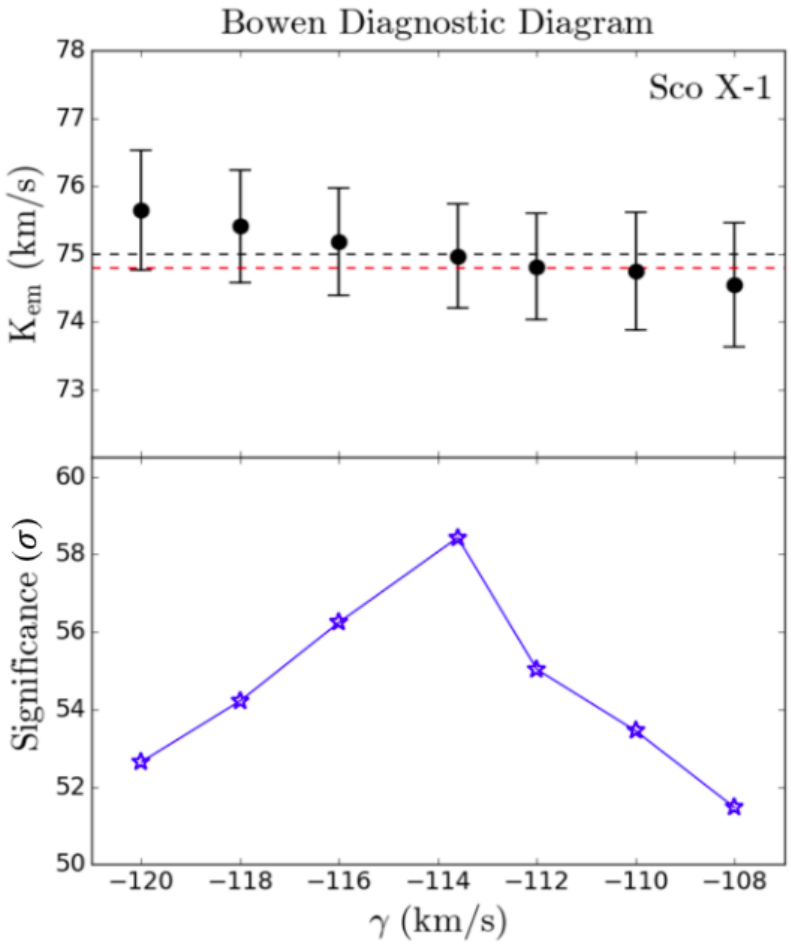

Figure 2.15: Bowen Diagnostic diagram for Sco X-1 showing the best-fit solutions of K_{em} (with bootstrap estimate of 1σ errors), and the significance level of the corresponding donor feature, as a function of the assumed systemic velocity. The K_{em} amplitude derived using Monte-Carlo Doppler mapping (black dashed line) is in excellent agreement with that derived from the RV technique (red dashed line).

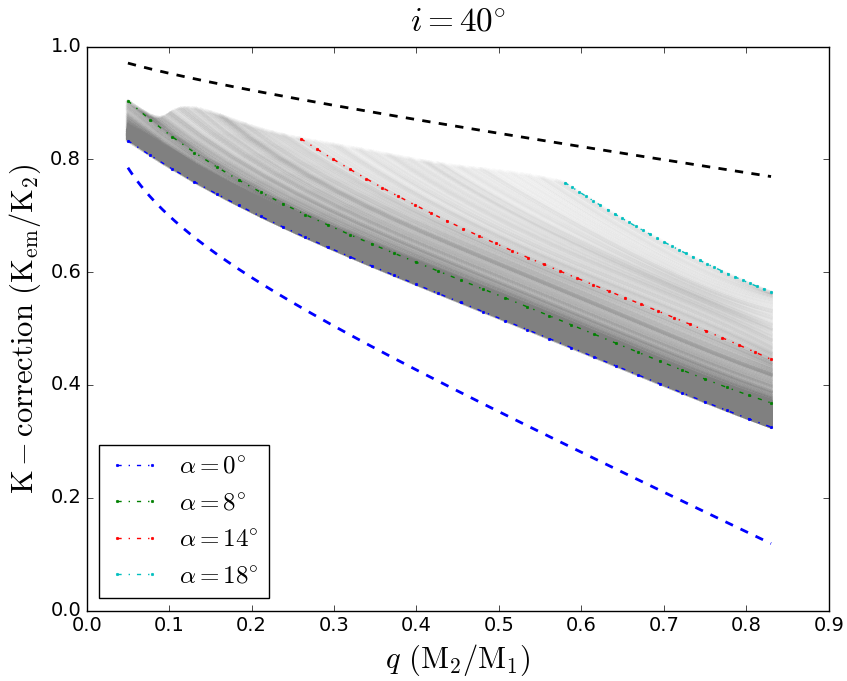

Figure 2.16: Plot of synthetic K_{cor} models (grey) for α between 0 and 18° as a function of q (for the low inclination case) determined by our code, based on the grids of K-correction models calculated by Muñoz-Darias et al. 2005 (coloured dash-dotted lines).

$N_4 q^4$, can be obtained with the generated model and applied to the measured K_{em} amplitude.

With the measurements of P_{orb} and K_2, equation 1.17 gives the minimum allowable mass of the primary M_1. Precise determinations of stellar masses require knowledge of the mass ratio q (= M_2/M_1 = K_1/K_2) as well as the inclination i. To fully account for the uncertainties in all observables/input parameters, we perform Monte Carlo simulations to obtain estimates of the probability density functions (PDF's) for unknown system parameters (essentially a brute-force tabulation of possible outcomes). The problem is quite simple for many systems as the random variables involved are uniformly distributed (e.g., α and i). By generating a large number of random trials while imposing other constraints (e.g. strict upper limit to i set by the absence of X-ray eclipses), the large number of outcomes can be evaluated (in individual trials) and assembled into the final PDF's for binary parameters.

In the next chapter, we apply the newly developed analysis tools to previously published datasets of Bowen sources spanning a range of S/N. The aim is to provide more descriptions and justifications of the methodology.

Chapter 3

Bowen survey

Part of Section 3.3 has been published in:

Jiménez-Ibarra, F., Muñoz-Darias, T., **Wang, L.**, Casares, J., Mata Sánchez, D. and Steeghs, D. et al.; *Bowen emission from Aquila X-1: evidence for multiple components and constraint on the accretion disc vertical structure*; 2018, Monthly Notices of the Royal Astronomical Society, **474**, 4717.

The analysis in Section 3.4 is performed for:

Muñoz-Darias, T. et al., in preparation.

Following the first discovery of the high excitation Bowen emission lines in Sco X-1 arising from the X-ray illuminated atmosphere of the donor star, continuous efforts have been made to search for donor signatures in other active LMXBs. In this chapter I apply my new set of Monte Carlo tools to published Bowen data sets of five non-eclipsing LMXB systems obtained from the Bowen survey (performed by our group between 1999–2005; Figure 3.1) as well as additional data collected during a system (Aql X-1)'s recent outbursts. These survey datasets (spanning a range of S/N) provide an excellent opportunity for further testing and validating our methodology.

For each system, we first present a summary of source data, followed by a detailed description of the results obtained at each step in the analysis (see Figure 3.2 for an overview of the analysis toolbox). Finally, we present our conclusions and provide updated and more robust binary parameter constraints.

3.1 4U 1636−536 (=V801 Ara) and 4U 1735−444 (=V926 Sco)

4U 1636−536 (=V801 Ara) and 4U 1735−444 (=V926 Sco) are among the optically brighter members of persistent LMXBs ($L_X \simeq 10^{37-38}$ erg s^{-1}), whose optical spectra usually consist

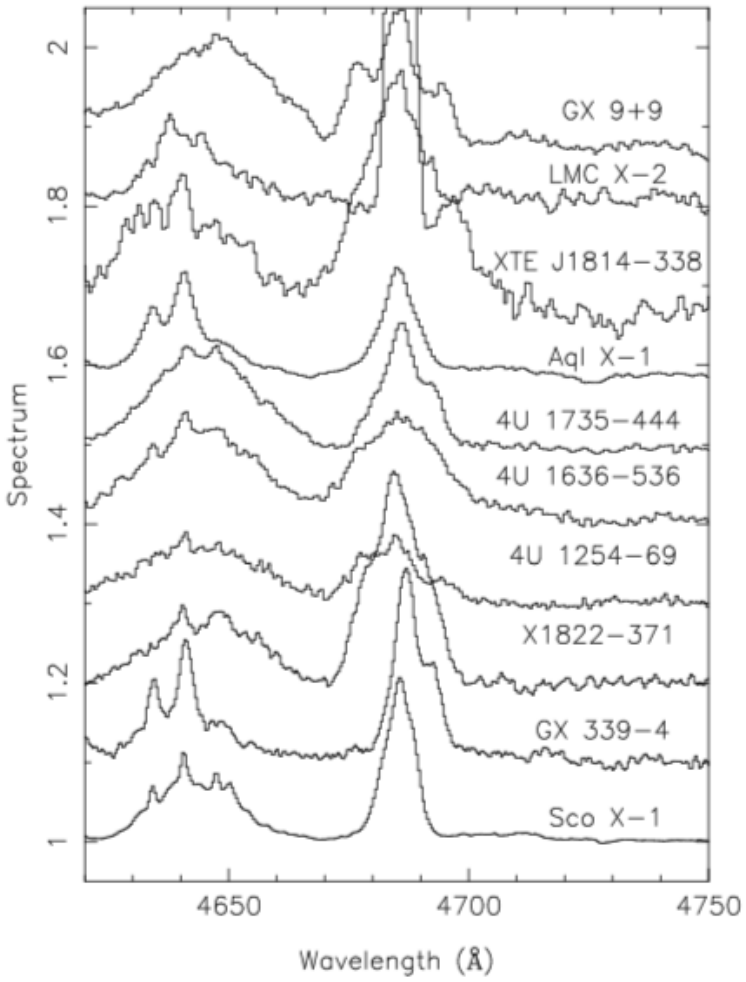

Figure 3.1: Average Doppler corrected spectra of the Bowen region and He II λ4686 in the rest frame of the donor for the systems observed by our team during the period between 1999 and 2005. Figure from Cornelisse et al. (2008).

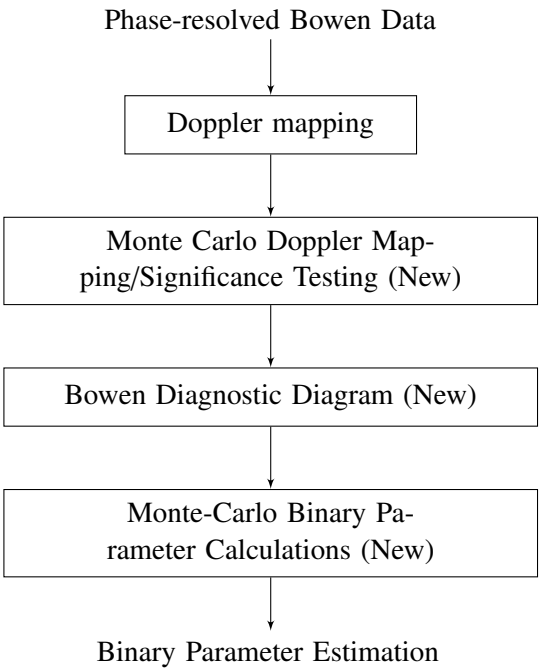

Figure 3.2: Toolbox for Bowen data analysis.

of a blue continuum with a few rather weak high excitation emission lines (in particular He II λ4686 and the N III/C III 4630-4660Å Bowen blend). The two sources share many similar properties: they are of similar apparent optical and X-ray brightness; they both show frequent X-ray bursts; and have similar orbital periods (3.80 and 4.65 hr for V801 Ara and V926 Sco, respectively) revealed through optical photometry (Pedersen et al. 1981; Corbet et al. 1986). Their light curves display small amplitude sinusoidal variations that can be interpreted as due to the varying visibility of the X-ray heated face of the donor star (van Paradijs et al., 1988). Hence, the photometric maxima should occur at phase 0.5 (i.e. superior conjunction of the donor), although we caution that in some cases this assumption requires further evaluation.

Among the few low-resolution spectroscopic studies of V801 Ara and V926 Sco, Smale & Corbet (1991) found that the Hα line core of V926 Sco is dominated by emission from the accretion stream or the impact point where the stream intersects the disc. Later on, Augusteijn et al. (1998) derived RV curves of He II λ4686 and the Bowen blend for both sources, and concluded that a significant amount of emission must also arise from the disc bulge. Inspired by the 2002 study of Sco X-1, which led to the first detection of the donor star in persistent LMXBs, Casares et al. (2006) applied the same technique to V801 Ara and V926 Sco, and found (in both cases) evidence of irradiated emission from the donor star using Doppler tomography of N III lines. Here we present a re-analysis of the data obtained

Table 3.1: Observations of V801 Ara and V926 Sco.

Object	Date	Instrument	Exposure time (s)	N_{obs}	Resolution (Å)	Reference
V801 Ara	2003 Jun 23,25	FORS2/VLT	600	42	1.2	[1]
V926 Sco	2003 Jun 23,25	FORS2/VLT	200	102	1.2	[1]

References.
(1) Casares et al. (2006)

by Casares et al. (2006) in order to confirm the significance of the donor signal as well as the accuracy of the absolute ephemerides defined in Casares et al. (2006).

3.1.1 Source data

V801 Ara and V926 Sco were observed in 2003 with the VLT, using the FORS2 Spectrograph attached to the 8.2-m Yepun Telescope (UT4). A total of 42 spectra of 600s of V801 Ara and 102 exposures of 200s of V926 Sco were obtained covering the wavelength range $\lambda\lambda$4514-5815 at 70 km s^{-1} (FWHM) resolution and a complete orbital cycle per night for each target. Table 3.1 shows a summary of source data. The raw images were de-biased and flat-fielded, and the spectra were subsequently extracted using optimal extraction routines in order to maximize the SNR of the output spectra (Horne, 1986). A He–Ne–Hg–Cd comparison lamp image was obtained during daytime for wavelength calibration purposes. All the spectra were calibrated in flux using observations of the flux standard Feige 110. We used data available in the reduced form as input for our analysis. For details of the observations and data reduction procedures, we refer to Casares et al. (2006).

3.1.2 Analysis

Figure 3.3 displays the trailed spectra of the Bowen blend and He II λ4686 in 15 phase bins. The binary phases were calculated using the ephemerides for times of maximum optical light (but shifted in phase by +0.5) given by Giles et al. (2002) and Augusteijn et al. (1998) for V801 Ara and V926 Sco, respectively. The Bowen blend of V801 Ara shows multiple narrow S-wave components moving in phase with each other (but significantly less clear than those observed in Sco X-1); which may be attributed to the irradiated donor star. On the other hand, the core of the Bowen region of V926 Sco is dominated by many weak and blended features that are difficult to trace by eye.

In contrast to the case of Sco X-1, here the Bowen emission features are too faint to be detectable in the individual spectra. Therefore, the Doppler tomography technique provides the only opportunity to search for faint donor components in these systems. In

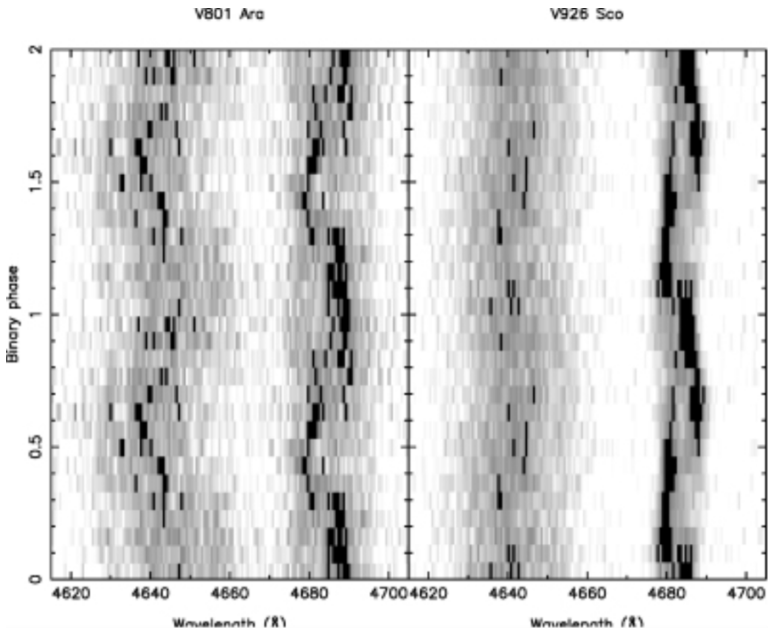

Figure 3.3: Trailed spectra of the Bowen blend and He II λ4686, in 15 phase bins using the *photometric ephemerides* of Giles et al. (2002) and Augusteijn et al. (1998) for V801 Ara (*left*) and V926 Sco (*right*). Figure is taken from Casares et al. (2006).

order to prepare phase-resolved data ready for analysis using the second generation, maximum entropy DOPPLER code[1] (T. Marsh), we rectified the individual spectra by subtracting a low-order spline fit to the continuum regions and re-binned them onto a uniform velocity scale (37 km s^{-1} pixel^{-1}). We then constructed the *combined Bowen Doppler maps*, for which we included all 4 relevant Bowen emission components (N III $\lambda\lambda$4634 & 4640 and C III $\lambda\lambda$4647 & 4650), as suggested by the Doppler-corrected average spectra in Figure 7 of Casares et al. (2006). Furthermore, since it is known that the choice of the input systemic velocity parameter can have a strong impact on the resulting Doppler image, a series of maps were computed (with γ varying from -200 to 200 km s^{-1}) to allow for the search over a range of γ that yield the best focused Bowen emission spot.

Figure 3.4 shows that the most compact spots are found for values of γ around -31 km s^{-1} for V801 Ara, consistent with the result obtained with the standard double-Gaussian method ($\gamma = -42 \pm 4$ km s^{-1}; Casares et al. 2006). The phasing of the emission spot in the reconstructed image (Figure 3.4; middle panel) using the photometric ephemeris suggests a possible signal from the companion. Thus, we decided to adopt the conservative estimate for $\gamma = -40 - -25$ km s^{-1} (V801 Ara) and consider reconstructions within this range (in steps of 3 km s^{-1}) in our bootstrap Monte Carlo analyses. Following the strategy

[1] https://github.com/trmrsh/trm-doppler

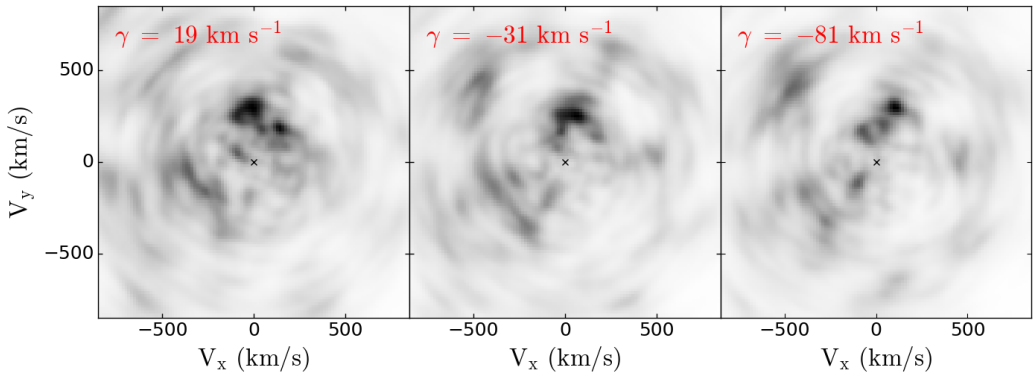

Figure 3.4: Bowen Doppler images of V801 Ara (using the photometric ephemeris) for an assumed γ parameter of 19 km s^{-1} (*left*), −31 km s^{-1} (*middle*) and −81 km s^{-1} (*right*).

described in Chapter 2, we created 2000 simulated images from independently generated bootstrapped datasets in the same manner as for the original map, and iterated them towards constant entropy. Measurements of the peak intensity and the centroid of the spot were then performed for the ensemble of Bowen images.

The first important step towards binary parameter estimation using the Bowen technique in cases of low SNRs is to confirm the statistical significance of the detected feature (found at the expected position of the donor). In Figure 3.5 (middle panel) we considered the distribution of the peak height of the promising 'donor signal'. By estimating the mean and 1σ error of the emission peak, it can be deduced that the detection is made at the >5σ confidence level (>99.999% confidence) for γ = −31 km s^{-1}. Hence, we confirm that the emission from the donor is detected for V801 Ara, and that the spectroscopic ephemeris defined in Casares et al. 2006 (by requiring that the spot observed in their N III Doppler map arises from the heated face of the secondary) is valid. Using the spectroscopic ephemeris, we derive a phase shift (between the donor spot and the vertical plane) $\Delta\phi_{\rm spot}$ of −0.010 ± 0.013 (see Figure 3.5; left panel), in better agreement with zero compared to $\Delta\phi_{\rm spot}$ = 0.020 ± 0.013 using the photometric ephemeris; hence the spectroscopic ephemeris is adopted as our preferred solution. Next, we aim to use the emission line diagnostics to obtain robust constraints on the RV semi-amplitude $K_{\rm em}$, which represents a strict lower limit to the true RV of the companion star. A diagnostic plot of the $K_{\rm em}$ amplitude (with bootstrap estimate for 1σ errors) as a function of the input γ (Figure 3.6) shows that $K_{\rm em}$ is stable against the assumed systemic velocity, and we would therefore derive

$$K_{\rm em,\,doppler} = 251 \pm 14 \text{ (stat) km s}^{-1} \text{ (V801 Ara).}$$

Turning to the case of V926 Sco, the maps show a prominent spot for γ around −140 km s^{-1} (or between −150 and −115 km s^{-1}), but shifted in phase by −0.18 with

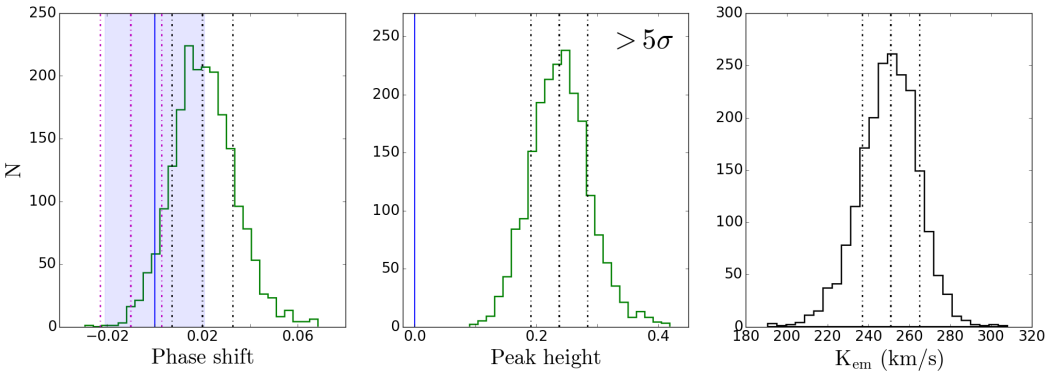

Figure 3.5: Number distributions of the phase shift (*left*), peak emission (*middle*) and K_{em} (*right*) measured from 2000 bootstrap maps of V801 Ara assuming a systemic velocity of -31 km s^{-1} and using the photometric ephemeris of Giles et al. 2002. Dashed lines indicate the mean and the $\pm$ 1σ confidence intervals. The emission feature is significant at a $>5\sigma$ level. Note also that although the phase shift with respect to the expected location of the donor star (blue interval) is consistent with zero (blue vertical line), the phase shift computed using the spectroscopic ephemeris of Casares et al. 2006 (magenta dashed lines) is closer to zero, thus the spectroscopic ephemeris would be our preferred solution.

respect to the expected location of the secondary (see Figure 3.7). If this feature (marked with a red circle in Figure 3.7; middle panel) is produced on the irradiated hemisphere of the secondary, then a correction can be applied to the previous photometric ephemeris by determining the rotation needed to align the feature along the positive V_y-plane.

We performed significance tests for essentially all spot features present in the Doppler image (including those marked with cyan circles in the middle panel of Figure 3.7), adopting again a more conservative estimate for $\gamma = -150 - -115$ km s^{-1} (V926 Sco) compared to the constraint (-121 ± 7 km s^{-1}) derived with the double-Gaussian technique. It can be shown that the centre of the peak height distribution for the compact spot marked with the red circle is different from zero at the $>5\sigma$ level (see middle panel of Figure 3.8), indicating a significant detection. Conversely, the significance levels of the rest of the features all fell below the 4σ threshold. Thus, only one statistically significant sharp feature is present in the noisy Bowen map of V926 Sco, which most likely represents a signature of the donor [as has been shown to be the case in Sco X-1 (Steeghs & Casares, 2002) and V801 Ara]. Additionally, based on the robust estimate for $\Delta\phi_{spot} = -0.177 \pm 0.010$ (Figure 3.8; left panel), we could confirm that the spectroscopic ephemeris defined in Casares et al. (2006), using a phase shift of -0.18, is accurate and reliable.

It readily follows from Figure 3.8 (right panel) that the RV semi-amplitude $K_{em} = 200 \pm 10$ (statistical) km s^{-1} for $\gamma = -140$ km s^{-1}. However, it is also important to notice any correlation between the derived K_{em} value and the input γ parameter using, e.g., a

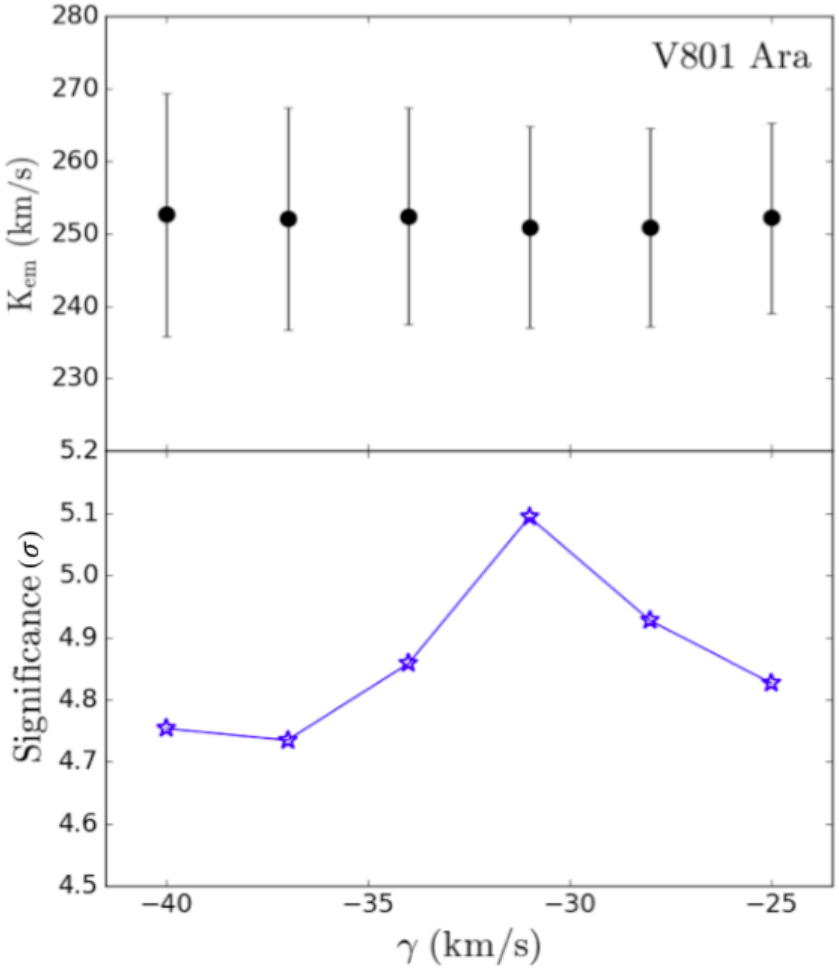

Figure 3.6: Bowen Diagnostic diagram for V801 Ara showing the best-fit solutions of K_{em} (with bootstrap estimate of 1σ errors), and the significance level of the corresponding donor feature over the preferred range of γ.

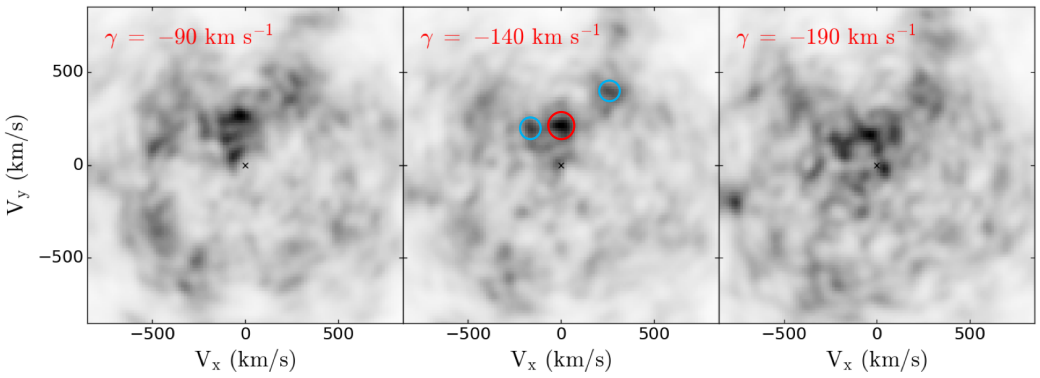

Figure 3.7: Bowen Doppler images of V926 Sco for an assumed γ parameter of -90 km s^{-1} (*left*), -140 km s^{-1} (*middle*) and -190 km s^{-1} (*right*). Red circle marks the most prominent compact spot that might arise from the irradiated companion star. For visualization purposes, all maps were rotated by a common phase angle of 64.8° to place the prominent emission feature at $(V_x, V_y) = (0, +\mathrm{K_{em}})$.

diagnostic diagram. In Figure 3.8, we show that $\mathrm{K_{em}}$ is positively correlated with γ (within the range of our preferred systemic velocities), with a maximum of 10 km s^{-1} drift around the central value. Therefore, in this case it is necessary to take systematic errors into account and measure the velocity semi-amplitude as:

$$\mathrm{K_{em,\,doppler}} = 200 \pm 10\ (\text{statistical}) \pm 10\ (\text{systematic})\ \text{km s}^{-1}\ (\text{V926 Sco}).$$

3.1.3 Determination of system parameters

To this date, the detection of Bowen emission lines from the irradiated companion in V801 Ara and V926 Sco provides the only opportunity for constraining dynamical masses of these persistent LMXBs. In this section, we use the newly developed, simpler binary parameter calculation tools introduced in Section 2.2.3 (compared with the method of Casares et al. 2006) to perform the K-correction to $\mathrm{K_{em}}$, and thereby deriving updated estimates for their binary mass ratio q and component masses M_1 & M_2.

V801 Ara

An additional constraint on the neutron star's projected velocity $K_1 (= qK_2)$ of V801 Ara is available from the study of 'burst oscillations' (i.e. nearly coherent high frequency pulsations). In particular a train of burst oscillations was discovered in an 800s interval during the 2011 'superburst' from this source, showing a frequency drift consistent with the orbital motion of the primary (Strohmayer & Markwardt, 2002). Using a circular orbit model with

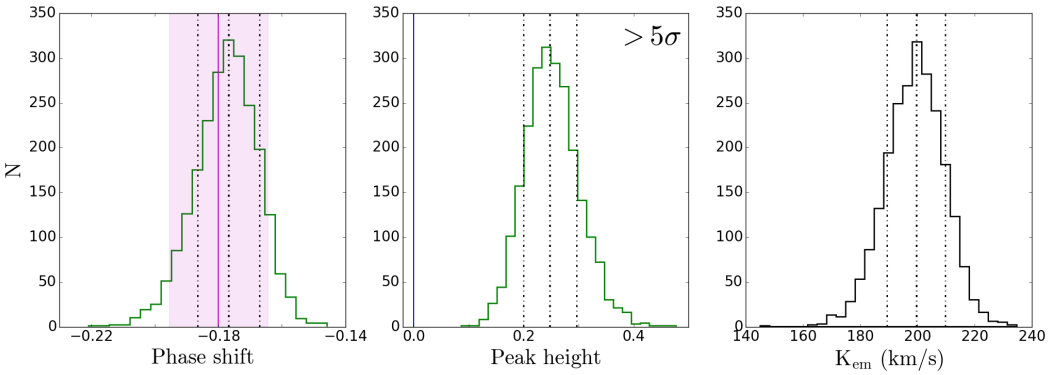

Figure 3.8: Number distributions of the phase shift (*left*), peak emission (*middle*) and K_{em} (*right*) measured from 2000 bootstrap maps of V926 Sco assuming a systemic velocity of -140 km s^{-1} and using the photometric ephemeris of Augusteijn et al. 1998. Dashed lines indicate the mean and the $\pm$ 1σ confidence intervals. The emission feature is significant at a >5σ level. Note that the phase shift with respect to the positive V_y-axis is similar to the phase offset calculated by Casares et al. 2006 ($\sim$ 0.18; magenta interval). Thus we confirm that the spectroscopic ephemeris defined in Casares et al. 2006 is accurate.

the reference epoch fixed to the *spectroscopic* ephemeris, Casares et al. (2006) re-analyzed the superburst pulsation data and derived a refined range for K_1 = 90–113 km s^{-1}.

To establish the probability density functions of the rest of the unknown system parameters, we performed a Monte Carlo analysis (10^6 trials) and considered a random distribution of K_1 (between 90 and 113 km s^{-1}) and binary inclinations (by resampling linearly from a cos$i$ distribution). Since the K-correction is constrained between $\alpha = 0$ (i.e. neglecting disc shielding) and the limit set by emission from the limb of the irradiated region, we let α also follow a uniform distribution, on (0°, 18°), covering the full range typical of XRBs. Furthermore, by selecting synthetic values of P_{orb} and K_{em} from a Gauss-normal distribution (with a mean and 1σ error equal to the observed values), a set of simulated binary parameters can be used as input to equation 1.17. For every combination of K_{em}, K_1 and α, we performed an accurate K-correction using the previously developed tool (see Section 2.2.3), followed by evaluation of q and true K_2. With a set of q, K_2 and P_{orb} in place, we then calculated a lower limit to i by assuming a maximum stable NS mass of 3.2 $M_\odot$; and an upper limit set by the absence of X-ray eclipses. A random inclination angle could be generated using a uniform distribution for cos(i) (between the lower and upper bounds set by the particular combination of input parameters). Finally, the masses were calculated and only outcomes of trials that yielded an M_1 value greater than the minimum stable NS mass ($\sim$ 0.9 $M_\odot$; e.g., Lattimer 2012) were assembled into the estimates for the PDF's for V801 Ara (Figures 3.10 and 3.11).

Thanks to our knowledge of K_1 from burst oscillations, we were able to derive

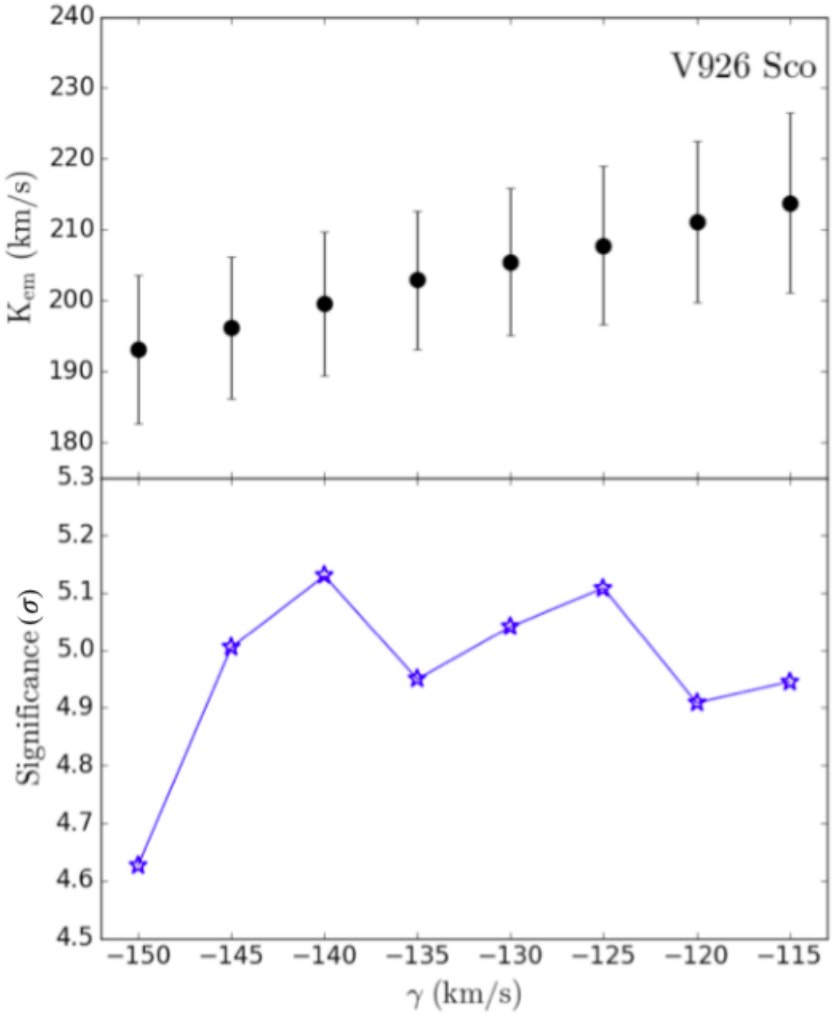

Figure 3.9: Bowen Diagnostic diagram for V926 Sco showing the best-fit solutions of K_{em} (with bootstrap estimate of 1σ errors), and the significance level of the corresponding donor feature over the preferred range of γ. In this case, systematics due to uncertainties in γ can be tracked down and should be added in quadrature to the statistical uncertainties.

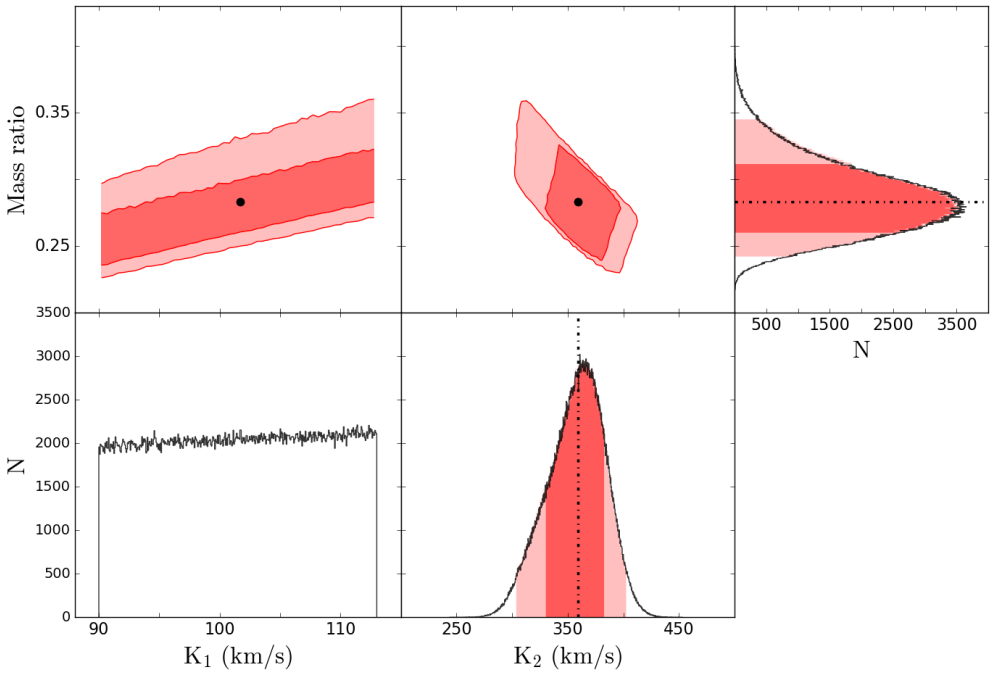

Figure 3.10: The 68 per cent and 95 per cent confidence regions and projected PDF's for K_2 and q for V801 Ara derived from the Monte Carlo binary parameter calculations (10^6 trials), using constraints on K_1 from burst oscillations (90–113 km s^{-1}). Dash-dotted lines indicate the locations of the 50^{th} percentile (median). The best estimates for the system parameters and their associated 95 per cent confidence intervals (CI) error bars are given in Table 3.2.

robust constraints on the true RV of the donor and the binary mass ratio (with 2σ errors of less than 20 per cent):

$$q = 0.28^{+0.06}_{-0.04}\ (95\%);$$
$$K_2 = 359^{+43}_{-56}\ \text{km s}^{-1}\ (95\%).$$

As Figure 3.11 shows, it remains difficult to place tight constraints on the masses of the binary components as we have only hard limits on the inclination (34° – 75°) deduced from the lack of X-ray dips. A summary of the system parameter estimates derived using our new set of Monte Carlo tools is provided in Table 3.2.

V926 Sco

The same method was applied to V926 Sco, and a strict upper limit to i was similarly set by the absence of X-ray dips ($i \leq 75°$). Assuming a NS accretor, only the outcomes of trials that yielded an M_1 value between 0.9–3.2 $M_\odot$ were assembled into the most conservative

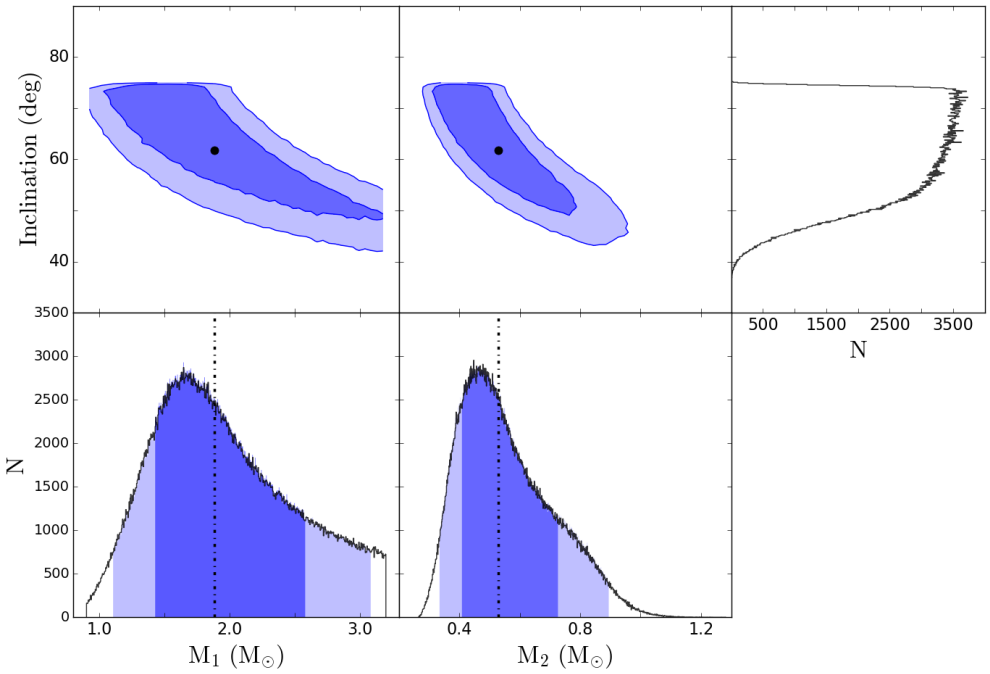

Figure 3.11: The 68% and 95% confidence regions and projected PDF's for the masses of the stellar components for V801 Ara. The median values are denoted by dash-dotted lines.

estimates for the PDF's (Figure 3.12 and 3.13; grey). In this case we do not have constraints on K_1 from burst oscillations and hence the RV and mass ratio constraints are much looser than in the previous case. Without making any further assumptions, we obtain

$$q = 0.45^{+0.26}_{-0.25}\ (95\%);$$
$$K_1 = 144^{+96}_{-94}\ \mathrm{km\ s^{-1}}\ (95\%);$$
$$K_2 = 316^{+65}_{-77}\ \mathrm{km\ s^{-1}}\ (95\%).$$

To explore alternative scenarios and show how additional constraints can strongly improve the determination of parameter PDF's, we obtained an independent estimate for K_1 using the double-Gaussian technique (Schneider & Young, 1980) to the wings of He II λ4686 line. As shown in Figure 3.3, the line cores are dominated by complex (low-velocity) emission components arising from the outer disc and/or the donor star. By convolving the emission line with a double-Gaussian filter of sufficiently large Gaussian separation, we extracted RV curves from the wings of the profile, which are presumably formed in the undisturbed inner accretion disc, and should therefore more closely replicate the motion of the compact object.

We employed a double-Gaussian bandpass with FWHM = 100 km s^{-1} and Gaussian separations in the range a = 400–1400 km s^{-1} in steps of 100 km s^{-1}. In order to

Table 3.2: Revised system parameters for V801 Ara and V926 Sco.

Parameter	4U 1636−536 V801 Ara	4U 1735−444 V926 Sco
P_{orb} (d)[a]	0.15804693(16)[a]	0.19383351(32)[c]
T_0 HJD(UTC)[a]	2452813.531(2)[b]	2452813.495(3)[b]
Significance	$> 5\sigma$	$> 5\sigma$
γ (km s^{-1})	-40 – -25	-150 – -115
K_{em} (km s^{-1})	251 ± 14	200 ± 10 (statistical) ± 10 (systematic)
K_1(km s^{-1})[b]	90 – 113[b]	144^{+96}_{-94} (95%)
K_2 (km s^{-1})	359^{+43}_{-56} (95%)	316^{+65}_{-77} (95%)
q (M_2/M_1)	$0.28^{+0.06}_{-0.04}$ (95%)	$0.45^{+0.26}_{-0.25}$ (95%)
i (°)	34 – 75	20 – 75
M_1 ($M_\odot$)	$1.9^{+1.2}_{-0.8}$ (95%)	$2.2^{+0.9}_{-1.3}$ (95%)
M_2 ($M_\odot$)	$0.5^{+0.4}_{-0.2}$ (95%)	$1.0^{+1.1}_{-0.7}$ (95%)

Notes.
T_0 indicates inferior conjunction of the donor.
[a]Adapted from Giles et al. 2002
[b]Adapted from Casares et al. 2006
[c]Adapted from Augusteijn et al. 1998

improve statistics, we also co-added the spectra into 15 phase bins using the *spectroscopic* ephemeris. Radial velocity curves obtained for different Gaussian separations were subsequently fitted with sine waves (fixing the period to the orbital value). Figure 3.14 displays the RV curve of He II λ4686 for the last separation, a = 1000 km s^{-1}, before the velocity points start to be corrupted by continuum noise as indicated by the diagnostic parameters σ(K)/K as well as the diagnostic diagram generated by Casares et al. (2006). A sine wave fit yields the systemic velocity $\gamma = -126 \pm 5$ km s^{-1} (consistent with our finding based on the Bowen diagnostic) and the semi-amplitude $K_1 = 81 \pm 7$ km s^{-1}; hence, we choose to adopt the upper bound of $K_1 \leq 103$ km s^{-1} in a different scenario shown in Figure 3.12 (red) and Figure 3.13 (blue). A further upper limit on M_2 is established by considering the zero-age main-sequence (ZAMS) mass-radius relation (Tout et al., 1996) for a 4.65-h Roche lobe, which lead to $M_2 \leq 0.58\ M_\odot$. Combining both new restrictions, the CIs for q and K_2 are significantly narrowed down to $q = 0.28^{+0.09}_{-0.15}$; $K_2 = 273^{+37}_{-53}$ km s^{-1}.

We should, however, bear in mind that the RV of the NS found by the double-Gaussian technique may still be skewed by asymmetry in the disc emission (and is not always reliable). Therefore, for V926 Sco we prefer the most conservative ranges shown in grey in Figures 3.12 & 3.13 and listed in Table 3.2.

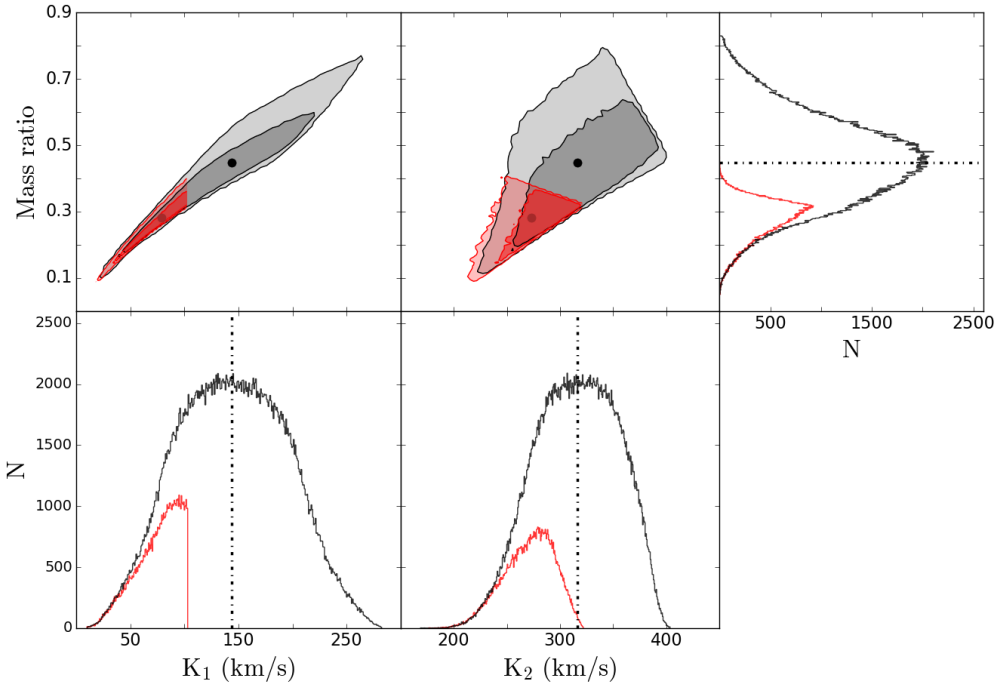

Figure 3.12: The 68 per cent and 95 per cent confidence regions and projected PDF's for K_1, K_2 and q for V926 Sco derived from the Monte Carlo binary parameter calculations (10^6 trials). Dash-dotted lines indicate the locations of the 50^{th} percentile. The most conservative estimates for the system parameters are shown in grey (and their associated 95 per cent CI error bars given in Table 3.2), compared to the results of a different scenario by applying additional K_1 and M_2 constraints (red).

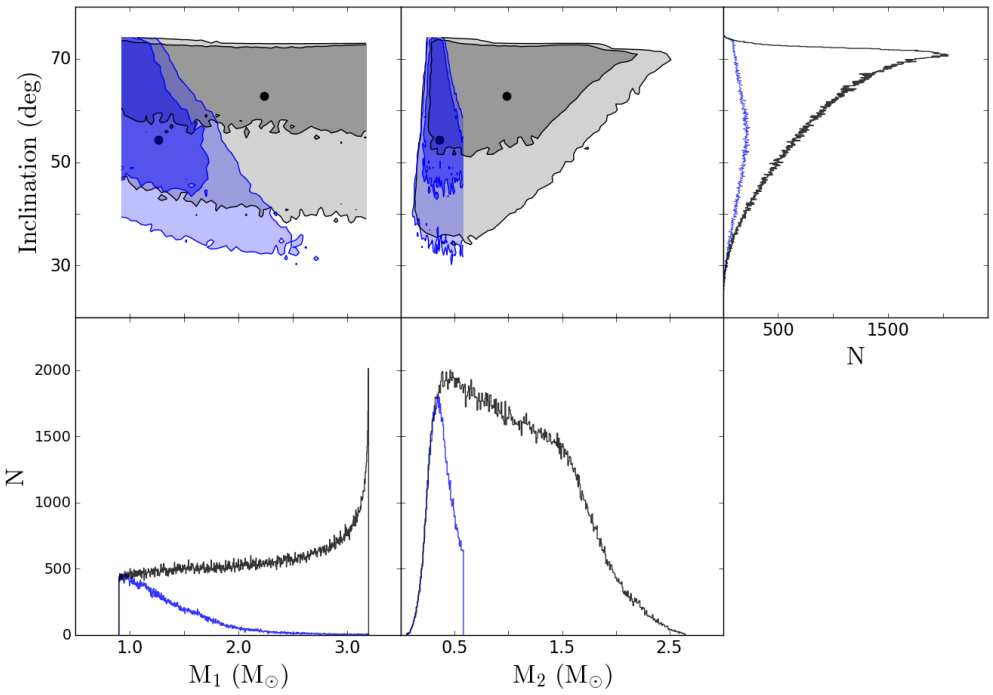

Figure 3.13: The 68% and 95% confidence regions and projected PDF's for the masses of the stellar components for V926 Sco. As in Figure 3.12, the most conservative estimates are shown in grey compared to the results of a possible scenario (applying additional K_1 and M_2 constraints; blue).

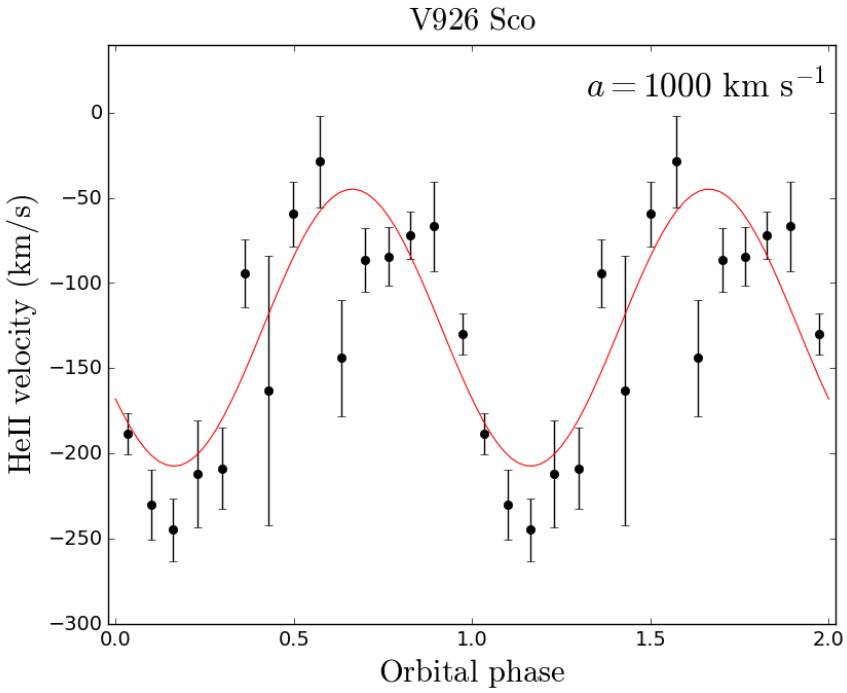

Figure 3.14: Radial velocity curve of the He II emission line based on a double Gaussian fit with separation a = 1000 km s^{-1} overplotted with the best-fit sine wave (red curve).

3.2 4U 1254−69 (=GR Mus)

XB 1254−690 is a persistently bright LMXB. It was identified with a faint blue star (GR Mus, V = 19.1), which exhibits the N III and C III Bowen blend in emission (Griffiths et al., 1978). The source produced type 1 X-ray bursts, indicating the presence of a neutron star. *EXOSAT* observations of XB 1254−690 confirmed the presence of recurrent X-ray dips with a period of 3.88 ± 0.15 hr and lasting ~0.2 cycles (Courvoisier et al., 1986). The dips are thought to be caused by occultation of the central source by a bulge on the outer edge of the accretion disc, implying a moderately high inclination. The optical photometry revealed the same period in the light curve as in the recurrence of X-ray dips. From V-band observations of GR Mus, Motch et al. (1987) determined an ephemeris (for times of minimum optical light) of T_{min} = JD 2445735.693(4) + 0.163890(9) d. Geometric modelling of the optical light curve constrains the binary inclination to 65° < i < 73°, and a distance of 8–15 kpc (Motch et al., 1987).

Barnes et al. (2007) presented simultaneous high-resolution blue optical spectroscopy and X-ray data of GR Mus. Their X-ray observations were used to re-establish the orbital ephemeris of Motch et al. (1987). Optical spectroscopy revealed features of the donor through the use of Doppler Tomography on the Bowen blend. In this section we revisit

Table 3.3: Optical observations of GR Mus.

Date	Instrument	Exposure time (s)	N_{obs}	Resolution (Å)	Reference
2004 May 26–28	FORS2/VLT	900	38	1.2	Barnes et al. 2007

the analysis of the Bowen data obtained for GR Mus and show that, while the donor signal detected by Barnes et al. (2007) is significant, an additional emission spot revealed by Doppler mapping and observed at an apparent phase of ~0.5 is unlikely to be a real feature.

3.2.1 Source data

GR Mus was observed in 2004 with the VLT using the FORS 2 spectrograph. A total of 38 spectra of 900s were obtained covering the wavelength range $\lambda\lambda$4513-5814 Å at 70 km s^{-1} (FWHM) resolution and a complete orbital cycle per night. The seeing during these observations varied between 0.5 and 2.1 arcsec. The slit was orientated at a position angle of 88.15° to include a comparison star in order to calibrate slit losses. Table 3.3 shows a summary of source data. We used data available in the reduced form as input for our analysis. For data reduction steps and details of the simultaneous X-ray observations, we refer to Section 2 of Barnes et al. (2007).

3.2.2 Analysis

The Bowen blend is displayed in the form of a trailed spectrogram in 20 phase bins (calculated using the updated X-ray orbital ephemeris of Barnes et al. 2007) in Figure 3.15. All of the individual spectra were first normalized to the continuum using a third-order polynomial fit. A sharp S-wave can be seen to move as a function of the orbit consistent with the phasing of the donor star. There also appears to be traces of other components moving in anti-phase with the feature from the donor. In order to better interpret the trail of the Bowen blend, we computed combined Bowen Doppler maps, for which we included all N III $\lambda\lambda$4634 & 4640 and C III $\lambda\lambda$4647 & 4650 components (but giving a higher weight to the strong N III λ4640 line; see Figure 12 of Barnes et al. 2007).

Based on the fact that assigning the correct systemic velocity would yield the most compact donor feature in the Doppler tomogram, we determined a range of γ for GR Mus between 170 and 195 km s^{-1} from the Bowen map (see Figure 3.16), consistent with the value determined by applying the double Gaussian technique to the He II lines (173 ± 12 km s^{-1}). The combined map for γ = 180 km s^{-1} (middle panel of Figure 3.16) revealed a spot feature at an apparent phase of ~0.5 in addition to the prominent companion feature. Given the phasing and the velocity of this feature (marked with a cyan circle), it is difficult

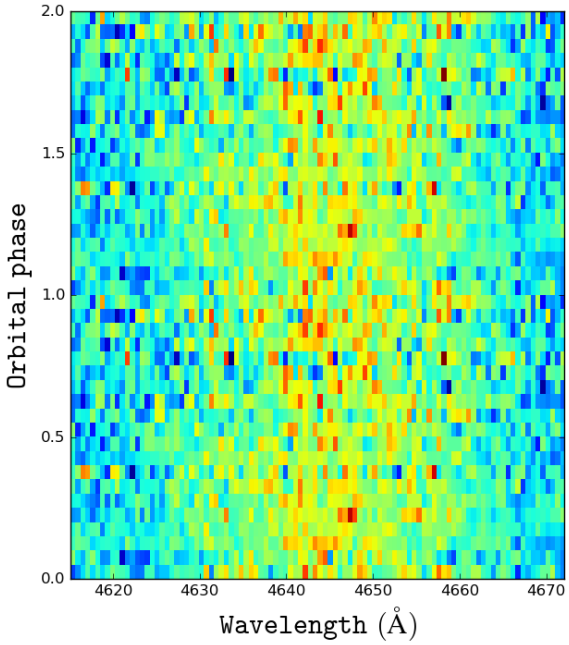

Figure 3.15: Trailed spectra of the Bowen blend for GR Mus, in 20 phase bins using the updated ephemeris of Barnes et al. 2007. The data are plotted twice for clarity. There is a sharp S-wave evident in the Bowen complex.

to provide a satisfactory explanation for its origin.

Following the standard analysis recipe, we proceeded to test the significance of both emission spots and considered reconstructions within the previously determined range of γ (in steps of 5 km s^{-1}). Figure 3.17 (middle panel) compares the distributions of the peak height for the two features, indicating that the spot at phase ~0.25 is >1.5σ weaker than the brighter feature. Since the mean of the peak intensity distribution is above zero at the 4.4σ level (for γ = 180 km s^{-1}) for the compact spot at the phasing where the companion star is expected (Figure 3.17; middle and left panels), we can confidently claim a donor detection in this system and obtain robust constraints on the apparent radial velocity K_{em}. We do note that the position of the peak height can be skewed by the image positivity criterion required by MEM, which will bias fluxes away from 0. The fainter of the two spots is most likely a noise artefact, as can be shown by our bootstrap test (~2.7σ) or, by visual inspection of the trailed spectra. From the bottom panel of the Bowen diagnostic diagram (Figure 3.18), we select a range (indicated by vertical dash-dotted lines), over which the significance of the Bowen spot is above the ~4σ level, as the final estimate for γ (170 – 190 km s^{-1}). It can also be concluded that the systematic uncertainty of K_{em} due to our assumption of γ is negligible compared to the statistical uncertainty, hence we constrain the RV semi-amplitude to

$$K_{em,\,doppler} = 255 \pm 19 \text{ (stat) km s}^{-1}.$$

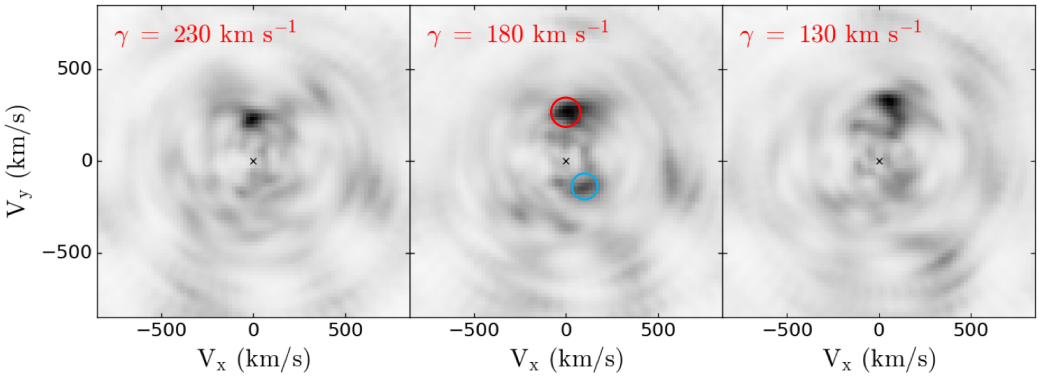

Figure 3.16: Bowen Doppler images of GR Mus (using the updated ephemeris of Barnes et al. 2007) for an assumed γ parameter of 230 km s^{-1} (*left*), 180 km s^{-1} (*middle*) and 130 km s^{-1} (*right*). The brighter of the two spots (marked with a red circle) occurs at the phasing where the companion star is expected. It is difficult to explain the origin of the second spot observed at an apparent phase of ~0.5 (marked with a cyan circle).

3.2.3 Determination of system parameters

Using a geometric model for the reprocessing of X-rays in LMXBs, de Jong et al. (1996) estimated an opening semi-angle of 12° for the accretion disc in GR Mus, in agreement with the range $\alpha \sim 9 - 13°$ derived by Motch et al. (1987) in order to explain the observed amplitude of the orbital photometric modulation. These limits can provide improvements in the K-correction (=K_{em}/K_2), which is an increasing function of α (although K_{cor} depends also strongly on q; see Chapter 1). Therefore, in our Monte Carlo simulations, we mainly considered scenarios where the more conservative α range of Motch et al. (1987) was adopted. By selecting synthetic α values from a uniform distribution between 9 – 13° and letting the inclination also follow a uniform distribution between the range 65 – 73°, we obtain estimates for

$$q = 0.35^{+0.17}_{-0.15}\ (95\%);$$
$$K_1 = 127^{+76}_{-63}\ (95\%);$$
$$K_2 = 363^{+54}_{-55}\ (95\%)$$

(see Figure 3.19; grey).

If we impose the constraint of the compact object velocity measured from the wings of the He II λ4686 emission line ($K_1 = 130 \pm 16$; Barnes et al. 2007), the 95% confidence interval for q can be narrowed down to 0.28 – 0.43, whilst the limits on K_2 are not significantly changed (Figure 3.19; red). However, Barnes et al. (2007) did note that the classic ring-like distribution of the accretion disc was not observed in their Doppler tomogram of He II λ4686 (presumably due to the strength of the low-velocity line core features vastly

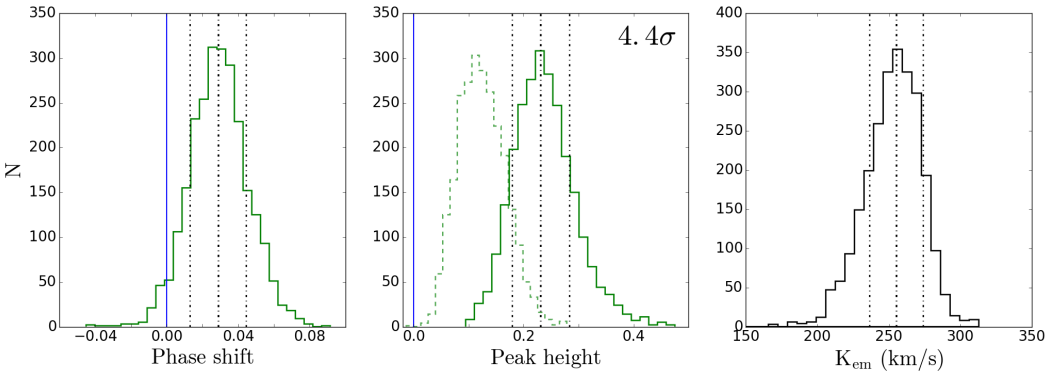

Figure 3.17: Number distributions of the phase shift (*left*), peak emission (*middle*; solid histogram) and K_{em} (*right*) of the donor emission spot measured from 2000 bootstrap maps of GR Mus assuming a systemic velocity of 180 km s^{-1} and using the updated ephemeris of Barnes et al. 2007. Dashed lines indicate the mean and the $\pm$ 1σ confidence intervals. The emission feature is significant at a 4.4σ level. Note that the phase shift with respect to the positive V_y-axis is consistent with zero (blue vertical line) within 2σ. The centre of the peak height distribution for the second spot at phase ~0.25 (dashed histogram) is different from zero (blue solid line) at <3σ level, indicating that the detection is not significant.

overwhelming the inner disc emission); and that the results of the double Gaussian technique may not be accurate. Thus, we prefer the conservative parameter PDF's without making additional assumptions about the K_1 velocity. Finally, due to the limited knowledge of K_2 and q, the mass of the donor is loosely determined to $0.2M_\odot \leq M_2 \leq 1.5M_\odot$ (Figure 3.20; grey); and the neutron star mass cannot be constrained by current data.

3.3 Aql X-1

Aquila X-1 is a recurrent neutron star transient LMXB which has exhibited both coherent millisecond X-ray pulsations at ~1.8 ms (Casella et al., 2008) and thermonuclear bursts (Galloway et al., 2008). The optical counterpart (V1333 Aql) was identified in 1978 as a star with B $\gtrsim$ 20 mag (in quiescence) and B ~ 17 mag in outburst (Thorstensen et al., 1978). The recurrence time of the outbursts is about 2 yr and they have been extensively monitored at different wavelengths. During the 2004 outburst, Cornelisse et al. (2007a) presented a preliminary estimate for the radial velocity of the donor star using narrow Bowen fluorescence lines (K_{em} = 247 $\pm$ 8 km s^{-1}). Their result is no longer compatible with the dynamical solution (K_2 = 136 $\pm$ 4 km s^{-1}) derived from near-infrared spectroscopy obtained in quiescence (Mata Sánchez et al., 2017). The discrepancy could result from spurious emission arising from localized regions of the disc that contribute to the Bowen blend (in a particular stage of the outburst).

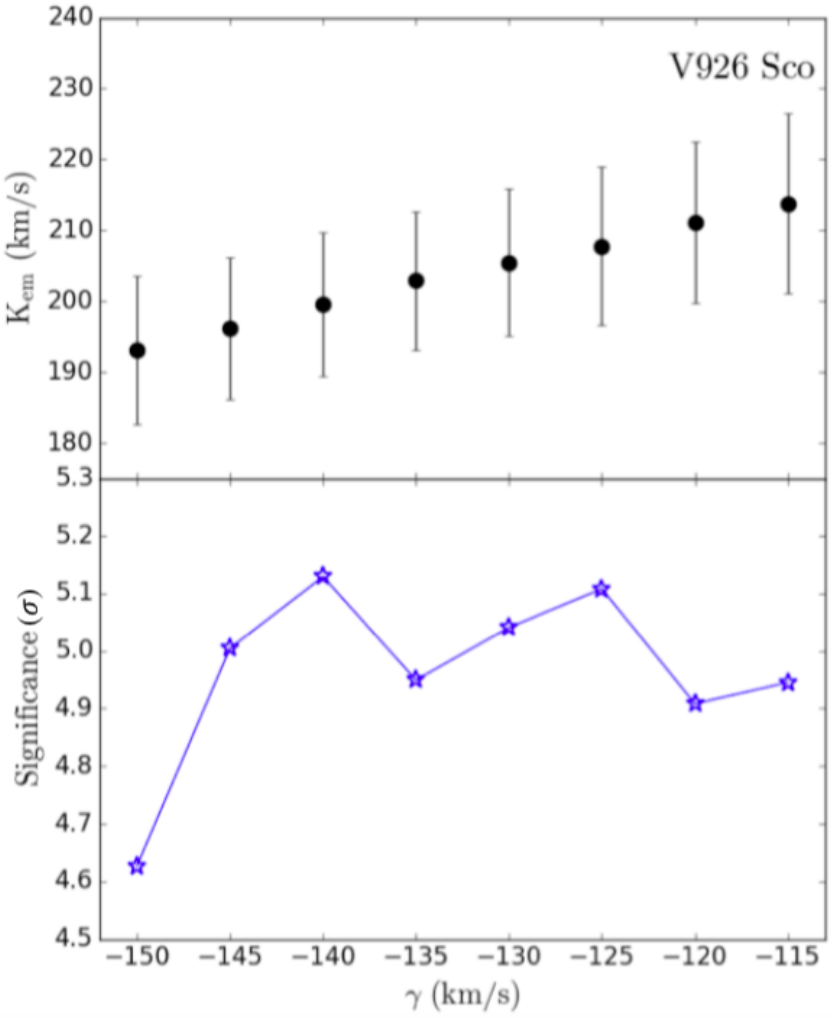

Figure 3.18: Bowen Diagnostic diagram for GR Mus showing the best-fit solutions of K_{em} (with bootstrap estimate of 1σ errors), and the significance level of the corresponding donor feature as a function of the assumed systemic velocity. Vertical dash-dotted lines mark our preferred range of γ, over which the statistical significance of the secondary feature is above $\sim 4\sigma$ (horizontal dashed line).

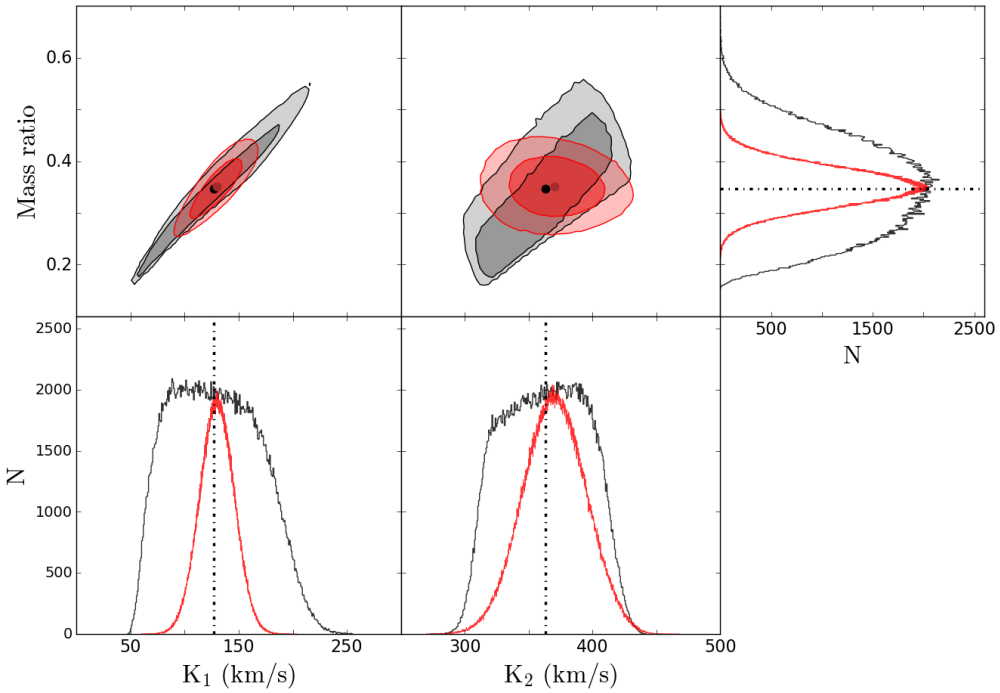

Figure 3.19: The 68 per cent and 95 per cent confidence regions and projected PDF's for K_1, K_2 and q for GR Mus derived from the Monte Carlo binary parameter calculations (10^6 trials). Dash-dotted lines indicate the locations of the 50^{th} percentile. The most conservative estimates for the system parameters are shown in grey (and their associated 95 per cent CI error bars given in Table 3.4), compared to the results of a different scenario by applying the K_1 constraints of Barnes et al. (2007) obtained with the double Gaussian method (red).

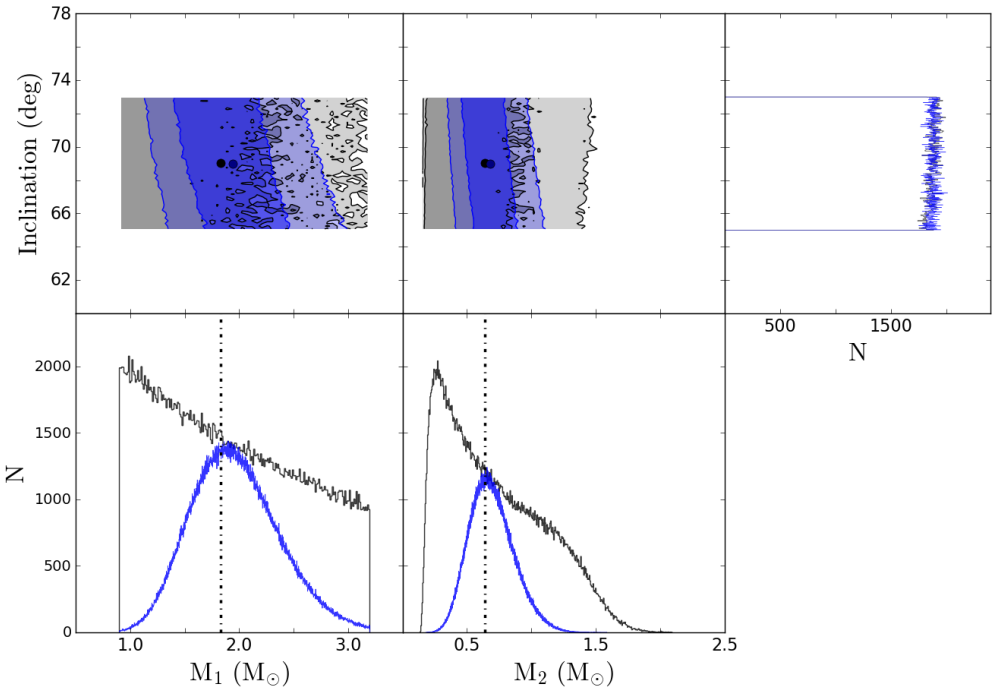

Figure 3.20: The 68% and 95% confidence regions and projected PDF's for the masses of the stellar components for GR Mus. The median values are denoted by dash-dotted lines. As in Figure 3.19, the most conservative estimates are shown in grey compared to the results of a possible scenario (applying additional K_1 constraints; blue).

Table 3.4: Revised system parameters for GR Mus.

Parameter	Value
P_{orb} (d)[a]	0.163890(9)[a]
T_0 HJD(UTC)[a]	2453151.509(3)[b]
Significance	$> 4\sigma$
γ (km s^{-1})	170 – 190
K_{em} (km s^{-1})	255 ± 19
α (°)	9 – 13[a]
K_1(km s^{-1})	127^{+76}_{-63} (95%)
K_2 (km s^{-1})	363^{+54}_{-55} (95%)
q (M_2/M_1)	$0.35^{+0.17}_{-0.15}$ (95%)
i (°)	65 – 73[a]
M_1 ($M_\odot$)	$1.8^{+1.3}_{-0.9}$ (95%)
M_2 ($M_\odot$)	$0.64^{+0.88}_{-0.44}$ (95%)

Notes.
T_0 indicates inferior conjunction of the donor.
[a]Adapted from Motch et al. 1987
[b]Adapted from Barnes et al. 2007

Jiménez-Ibarra et al. (2018) presented phase-resolved optical spectroscopy of Aql X-1 taken during the 2011, 2013 and 2016 outbursts. The *complete* phase coverage has allowed us to exploit the Doppler mapping technique to accurately determine a new constraint on K_{em}, which is now fully compatible with the near-infrared measurement. By combining the two measurements of K_{em} and K_2, Jiménez-Ibarra et al. (2018) determined (for the first time) the disc opening angle $\alpha = 15.5^{+2.5}_{-5}$ deg, consistent with theoretical work if significant X-ray irradiation is taken into account.

3.3.1 Source data

Phase-resolved spectroscopy of Aql X-1 was obtained with the Optical System for Imaging and low-Intermediate Resolution Integrated Spectroscopy (OSIRIS) located at the Nasmyth-B focus of the 10.4 m Gran Telescopio Canarias (GTC). A total of 65 spectra were acquired covering the wavelength range $\lambda\lambda$4500–6000 Å, at 132 or 173 km s^{-1} (FWHM) resolution, and a complete orbital cycle over 19 different epochs (see Figure 1 of Jiménez-Ibarra et al. 2018). The data were de-biased and flat-fielded using IRAF standard routines, and the pixel-to-wavelength calibration was made using a regular HgAr+Ne+Xe arc lamp exposure taken on each observing block. We used data reduced by F. Jiménez-Ibarra as input for our analysis. For details of the observations, we refer to Section 2 of Jiménez-Ibarra et al. 2018

(see also their Table 1 for a summary of source data).

3.3.2 Gaussian fitting

We initially carried out multiple Gaussian fits to the continuum-normalised GTC spectra in order to directly measure the RV curve of the narrow Bowen components over a full orbital period. We used two narrow components to fit the N III 4634 Å and N III 4640 Å emission lines, and a broad Gaussian to represent the broader underlying profile. The FWHM of the Gaussians were fixed to 200 and 1150 km s^{-1} for the narrow and broad components, respectively. The position and height of each Gaussian were set as free parameters, but with the relative separation between the two narrow components held constant (for obtaining a stable velocity solution). The same analysis was applied to the VLT data presented in Cornelisse et al. (2007a). Figure 3.21 shows the fitted velocity offset as a function of the orbital phase using the ephemeris from Mata Sánchez et al. (2017).

At first sight, we did not observe a sinusoidal RV curve similar to that obtained for Sco X-1 (Steeghs & Casares, 2002). By computing limiting cases for the expected K_{em} in Aql X-1 (light green area in Figure 3.21), we identified 28 points that are consistent with the expected radial velocity of the donor (blue dots). Those that are not consistent with a donor origin ($>3\sigma$ from the green region) are shown in grey triangles. 27 spectra did not enable a clear identification of the N III components and are denoted by black crosses. Thus, our Gaussian fitting suggests that the Bowen blend is tracing more than one emission region. It is also important to note that none of the velocity offsets derived from the 2004 VLT data were compatible with those expected for the companion star.

3.3.3 Doppler mapping

Following the previous studies, we computed Doppler maps using the 65 GTC spectra, for the strongest Bowen narrow component N III 4640 Å, using the ephemeris from Mata Sánchez et al. (2017) and also their systemic velocity ($\gamma = 104 \pm 3$ km s^{-1}). The result is shown in Figure 3.22, where a compact spot along the positive V_y-axis is clearly detected. The image also reveals a bright extended region, which is consistent with the gas-stream trajectory and/or the region where the in-falling material impacts the outer edge of the disc (i.e. the hotspot). As a next step, we used bootstrap techniques to compute confidence intervals for the velocity of the compact spot. To this end, we model a data set of 2000 bootstrapped maps from the original data and subsequently computed the peak height and K_{em} via a 2-D Gaussian fit to each bootstrapped map. Since the bootstrap distributions for both parameters are Gaussian (see Figure 3.23), we estimated the significance of the spot to be $\gtrsim 13\sigma$ and $K_{em} = 102 \pm 6$ km s^{-1} via Gaussian fitting to the histograms.

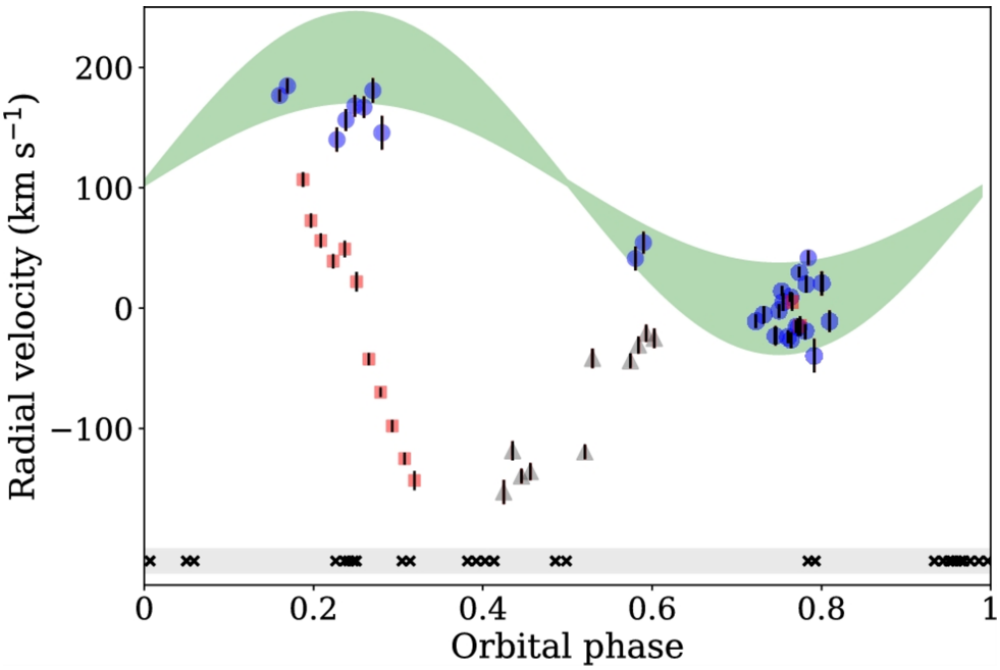

Figure 3.21: Radial velocity as a function of orbital phase derived from Gaussian fits of the Bowen blend narrow components. The light green area represents the region where the RV is consistent with that arising from the inner side of the companion star. Blue dots indicate velocities compatible (within 3σ) with the expected RV of the donor, while grey triangles correspond to those that are not consistent. Crosses show the phases of those spectra in which N III lines could not be identified. The velocities obtained from the VLT data of Cornelisse et al. (2007a) are shown as red squares.

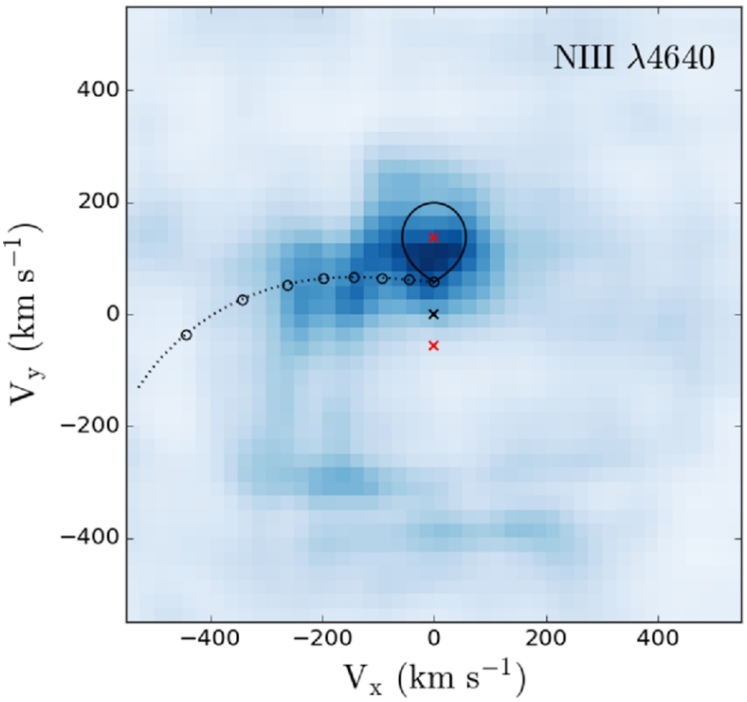

Figure 3.22: The Doppler tomogram of N III 4640.64/4641.84 Å computed using the updated binary period, ephemeris and γ = 104 km s^{-1} from Mata Sánchez et al. (2017). The origin (denoted by a black cross) corresponds to the centre of mass of the system. We overplot the gas-stream trajectory and the Roche lobe of the companion assuming K_2 = 136 km s^{-1} and a mass ratio of 0.41. The true orbital velocities of the companion (0, K_2 = 136 km s^{-1}) and the neutron star (0, $-K_1$ = 56 km s^{-1}) are denoted by red crosses.

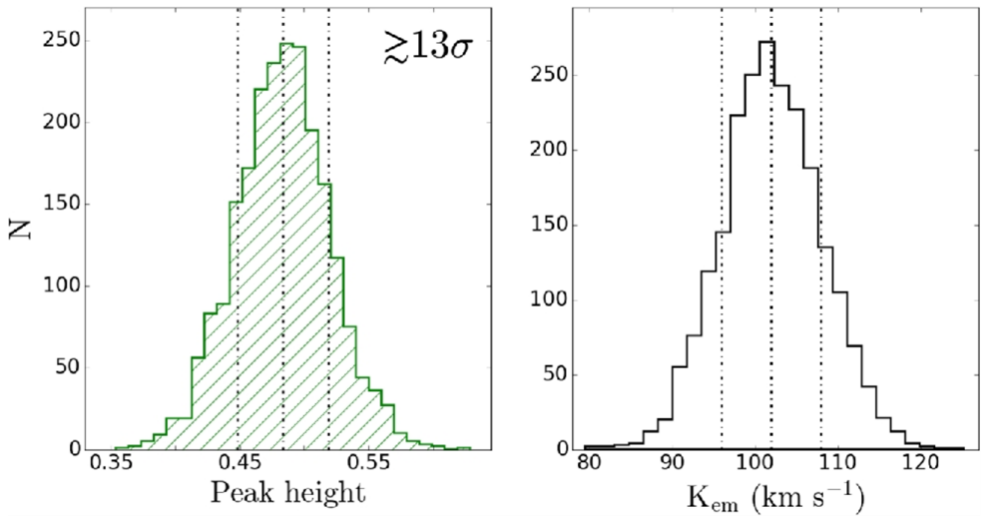

Figure 3.23: Distributions of the relative peak height (left) and K_{em} (right) determined from 2000 bootstrapped maps iterated to reach the same image entropy (S = −0.04) as that of the original image (Figure 3.22). Dashed lines indicate the mean and the $\pm 1\sigma$ confidence intervals. The emission feature is significant at the $\gtrsim 13\sigma$ level, providing a radial velocity semi-amplitude of $K_{em} = 102 \pm 6$ km s^{-1}.

The two different analysis techniques (RV and Doppler tomography) used here are closely related and essentially give consistent results, i.e., **the Bowen blend is tracing more than one emission component**. However, Doppler tomography has the advantage of cleanly separating different sources of emission on a velocity plane, which makes it better suited for detecting the donor and measuring K_{em}. We also benefited from the revised ephemeris and the complete phase coverage, making us confident that the donor has been unambiguously detected in this work. With transients, one should still be careful when mixing data together spanning different outburst states as the Bowen blend may not always be dominated by the donor.

3.3.4 Opening angle of the accretion disc

Given that K_{em}, K_2 and q are constrained, we carried out a Monte Carlo analysis to determine the range of accretion disc opening angles compatible with the observables. Using Gaussian distributions from the values reported in Table 3.5, a synthetic distribution of $K_{cor} = K_{em}/K_2$ was created. We then produced synthetic K-correction values from the models of Muñoz-Darias et al. (2005) sampling q from 0.05 to 0.85 in steps of 0.01, and α from 0 to 22° in steps of 0.5°. The disc opening angle α can be solved by comparing each trial K_{cor} with the synthetic values for a given q (adopting a Gaussian distribution for q). Finally, we obtained the projected 1D probability density function of α using 8×10^7 Monte Carlo trials

Table 3.5: System parameters for Aql X-1.

Parameter	Value
K_2^a	136 ± 4 km s^{-1}
K_{em}	102 ± 6 km s^{-1}
Significance	$\gtrsim 13\sigma$
q^a	0.41 ± 0.08
i^a	36 – 47 deg
α	$15.5^{+2.5}_{-5}$ deg (90%)

Notes.
[a]Adapted from Mata Sánchez et al. 2017

and then marginalized over q. Considering 90 per cent confidence levels, we estimated $\alpha = 15.5^{+2.5}_{-5}$ deg.

This estimate is consistent with the average value ($\alpha = 12°$) proposed by de Jong et al. (1996) using a simple geometric model for the reprocessing of X-rays in LMXBs. On purely theoretical grounds, Meyer & Meyer-Hofmeister (1982) studied the role of X-ray heating on the vertical structure of the accretion disc and showed that X-ray radiation is expected to thicken the accretion disc significantly (to $\alpha \sim 18 - 22$ deg). Our result is clearly consistent with an irradiation driven thick accretion disc, providing strong support for the theoretical works. As a final note, the upper limit to our α constraint is roughly consistent with the maximum disc opening angle for the donor to be irradiated at all. Indeed, opening angles close to this limit might explain the complex and very variable evolution of the Aql X-1 Bowen blend narrow components.

3.4 X1822-371

3.4.1 Introduction

X1822−371 is one of the brightest low-mass X-ray binaries in the optical, and the prototypical 'accretion disk corona' (ADC) source ($L_X/L_{opt} = 20$), where the combination of a high inclination and a thick disk obscures the central X-ray source. The X-rays are scattered into the line-of-sight by a large Compton-thick highly ionized corona above and below the center of the accretion disc (White & Holt, 1982). Its light curve shows orbital modulation in both the X-ray and optical bands, with a period of 5.57 hr (e.g. Mason et al. 1980; Hellier & Mason 1989). The eclipses of the disc by the companion has allowed an accurate determination of the inclination angle, $i = 82.5 \pm 1.5°$ (Heinz & Nowak, 2001); and estimates for the disc opening angle, $\alpha \sim 12 - 14°$ (Hellier & Mason 1989; Heinz & Nowak 2001).

The source also displays 0.59 s X-ray pulsations, making it one of the rare precursors of millisecond pulsars. Pulse arrival time analysis led to an extremely precise determination of the neutron star orbit, $a \sin i$ for the NS of 1.006(5) lt-s, corresponding to a radial velocity semi-amplitude of 94.5 ± 0.5 km s^{-1} (Jonker & van der Klis, 2001). Therefore, only an accurate determination of the RV curve of the companion is required for a precise NS mass constraint.

Casares et al. (2003) presented the first clear evidence for the motion of the companion using the N III λ4640 line with a velocity amplitude of K_{em} = 300 ± 8 km s^{-1}. A well-focused N III spot, centered along the V_y-axis, can be detected in the Doppler tomogram (computed using the pulsar ephemeris) for systemic velocities of ∼−44 km s^{-1}, based on the motion of the He II λ4686 wings. The application of numerical solutions for the K-correction to a more conservative value of K_{em} = 300 ± 15 km s^{-1} (combined with previous determinations of other parameters) yielded $1.61 \leq M_1 \leq 2.32\ M_\odot$ (Muñoz-Darias et al., 2005) – in strong support to the presence of a massive neutron star.

In this section, we perform a preliminary analysis on data taken in 2006 (with UVES/VLT) in order to obtain the most robust determination of K_{em}. The final goal of this study (Muñoz-Darias et al.; in preparation) is to measure the width of the Bowen lines to independently infer the disc opening angle (through further modelling) and therefore obtain a precise NS mass solution.

3.4.2 Analysis

X1822-371 was observed on the nights of 2006 June 23 and 24 with the Ultraviolet and Visual Echelle Spectrograph (UVES) on the VLT. A total of 266 spectra of 200s were obtained (with a FWHM resolution of 7–10 km s^{-1}) covering over one complete orbital cycle per night. The Bowen blend is dominated by multiple weak S-waves, moving as a function of the orbit consistent with the phasing of the donor, but are barely detectable in our low SNR individual spectra. Following Casares et al. (2003), we start by applying the Doppler tomography-based method to extract the RV amplitude of the narrow emission components. The spectra were rectified by subtracting a low-order spline fit to the continuum regions and re-binned onto a uniform velocity scale of 3 km s^{-1} pixel^{-1}. We then binned the continuum-subtracted spectra into 80 phase bins (covering one orbital cycle) using the most updated orbital ephemeris of Burderi et al. (2010)

$$T_0\ \mathrm{HJD(UTC)} = 2445615.30866 + 0.232108861(25)\mathrm{E}, \tag{3.1}$$

derived from the analysis of the eclipse arrival times spanning the period 1977–2008. A combined Bowen Doppler map was subsequently constructed including 4 Bowen emis-

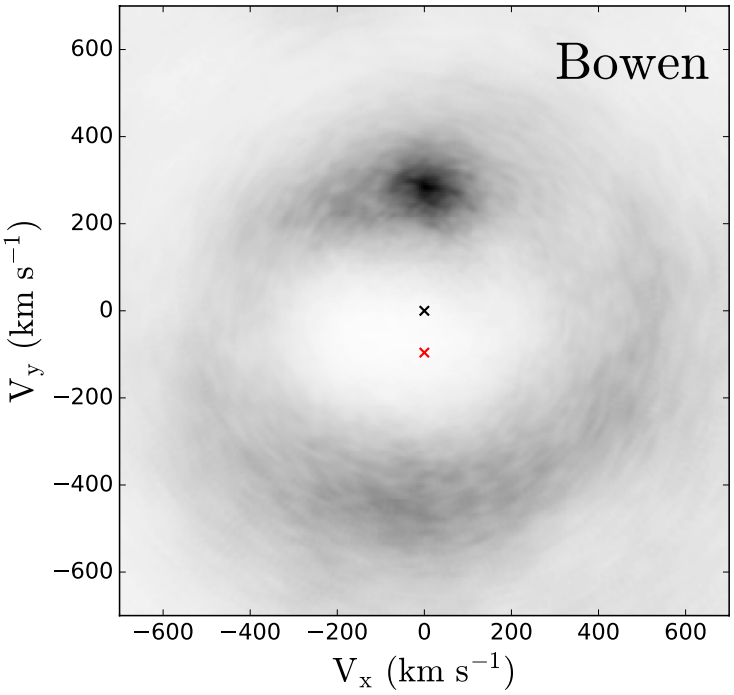

Figure 3.24: Doppler tomogram of N III $\lambda\lambda$4634/4640 and C III $\lambda\lambda$4647/4650 computed using the most updated ephemeris and period from Burderi et al. (2010). The origin (denoted by a black cross) corresponds to the centre of mass of the system using $\gamma = -44$ km s^{-1}. The red cross denotes the orbital velocity of the neutron star at (0, −94.5 km s^{-1}).

sion components (N III $\lambda\lambda$4634/4640 and C III $\lambda\lambda$4647/4650) in order to enhance the signal strength. Figure 3.24 displays the combined map for the best estimate for the systemic velocity, $\gamma = -44$ km s^{-1}, inferred from the He II wings (Casares et al., 2003).

The compact spot produced on the irradiated face of the donor can be clearly detected along the V_y-axis, at a position ($V_x \sim 3$ km s^{-1}, $V_y \sim 278$ km s^{-1}) similar to that of the 2003 N III spot. The map also reveals a ring-like feature approximately centered on the expected position of the NS (red cross in Figure 3.24), which we interpret as emission from the accretion disc.

In order to obtain a robust estimate for the RV semi-amplitude, we explored a range of trial γ values centered on −44 km s^{-1}; and ran bootstrap tests for γ between −56 and −32 km s^{-1} (that produced a well-focused donor spot), followed by calculating the significance and K_{em} amplitude. The bootstrap distributions for all spot parameters are Gaussian (see Figure 3.25), therefore we estimated the significance of the donor signal to be $\sim 18\sigma$ (for $\gamma = -44$ km s^{-1}) via Gaussian fitting to the peak height distribution. From the diagnostic diagram (Figure 3.26), we can robustly determine a preferred range of γ over which the phase shift relative to the orbital ephemeris is consistent with zero within 3σ (vertical lines

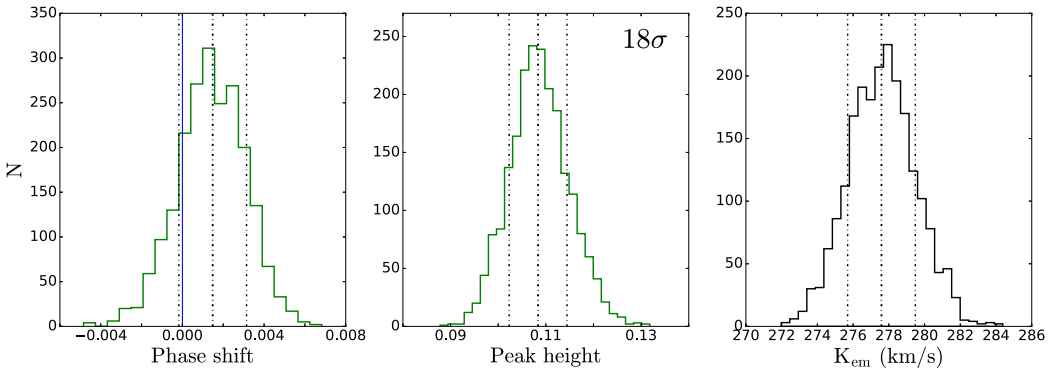

Figure 3.25: Number distributions of the phase shift (*left*), peak emission (*middle*) and K_{em} (*right*) measured from 2000 bootstrap maps of X1822−371 assuming a systemic velocity of -44 km s^{-1} and using the updated ephemeris of Burderi et al. (2010). The emission feature is significant at an 18σ level. The phase shift relative to the updated orbital ephemeris is consistent with zero (blue interval).

in the diagnostic diagram). This gives an independent estimate for γ of -40 to -48 km/s. Moreover, it's clear that the significance peaks in this range, which is also consistent with the previous γ estimate from Casares et al. (2003). Finally, the bottom panel of Figure 3.26 shows that the RV amplitude is stable with respect to γ. Hence, we obtain a final constraint on K_{em} of

$$K_{em,\,doppler} = 278 \pm 2 \text{ (statistical) km s}^{-1}.$$

3.4.3 Future plan

So far, the ADC source X1822−371 is the best candidate to apply an accurate K-correction. The known system parameter estimates for X1822 are summarized as follows:
(i) Orbital period = 20054.2056(22)s (Burderi et al., 2010);
(ii) Inclination = 82.5 ± 1.5° (Heinz & Nowak, 2001);
(iii) Radial velocity of the NS, $K_1 = 94.5 \pm 0.5$ km s^{-1} (Jonker & van der Klis, 2001);
(iv) $K_{em,\,Bowen} = 278 \pm 2$ km s^{-1} $< K_2$; significance $\simeq 18\sigma$ (this work).

All that remains to be determined (for getting the most precise mass constraints) is the disc opening angle. The measurement of α (possibly from the width of the lines) is work in progress, and the remaining analyses will be reported in Muñoz-Darias et al. (in preparation). Final determinations of component masses – including the full propagation of uncertainties – may provide compelling evidence for a massive NS ($M_{NS} > 1.6\ M_\odot$) in X1822, reinforcing the theory that LMXBs could harbor heavy NSs due to sustained

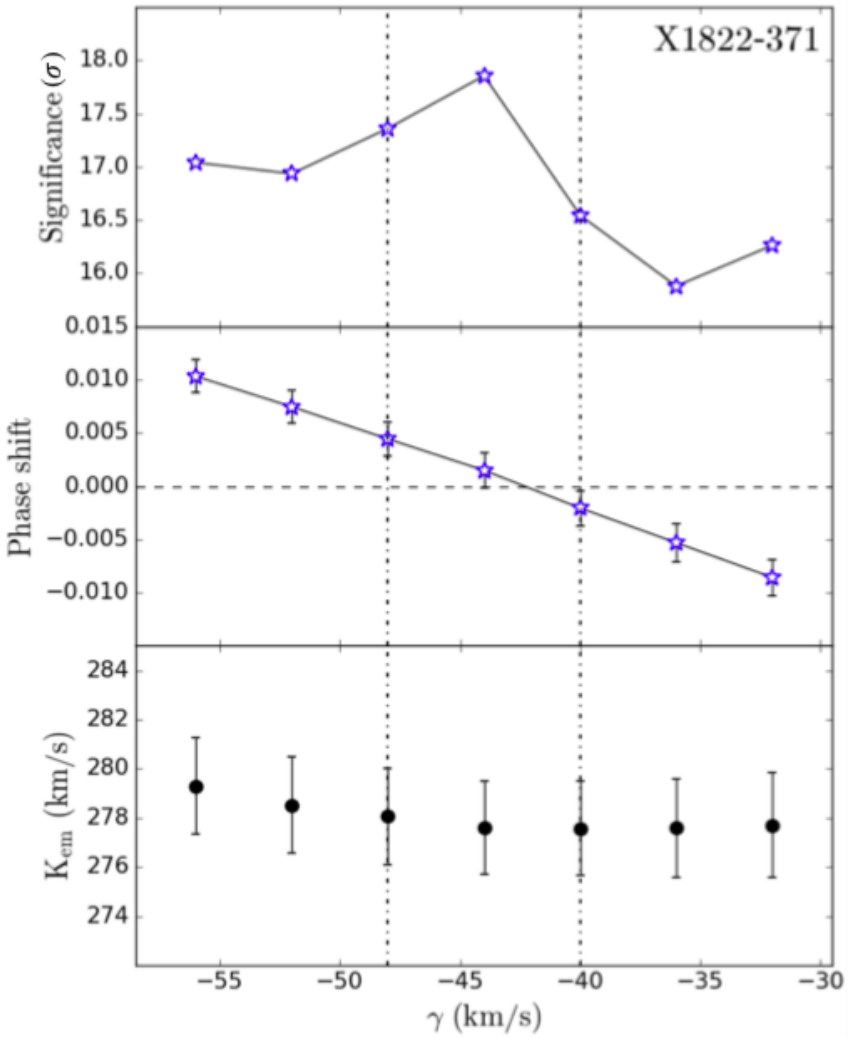

Figure 3.26: Bowen diagnostic diagram showing the best-fit solutions of the significance level, phase shift and K_{em} amplitude (with bootstrap estimate of 1σ errors) of the donor spot derived from the combined Bowen map, as a function of the assumed systemic velocity. Vertical dash-dotted lines mark the preferred range of γ (see Section 3.4.2).

episodes of mass accretion from the companion.

Chapter 4

XTE J1814-338

Based on:

Wang L., Steeghs D., Casares J., Charles P. A., Muñoz-Darias T., Marsh T. R., Hynes R. I., O'Brien K.; *System mass constraints for the accreting millisecond pulsar XTE J1814-338 using Bowen fluorescence*; 2017, Monthly Notices of the Royal Astronomical Society, **466**, 2261.

4.1 Introduction

The fifth accreting millisecond X-ray pulsar XTE J1814-338 was discovered on June 5 2003 by the *Rossi X-ray Timing Explorer (RXTE)* satellite during routine observations of the Galactic-center region, and has a pulse frequency of 314 Hz (Markwardt & Swank, 2003). Among the ~15 known AMXP systems (see Patruno & Watts 2012 for a recent review), its 4.3 hrs orbital period is the most similar to the period of 'classic' non-pulsing neutron star LMXBs, e.g., 4U 1735-444 (4.7 hrs), GX 9+9 (4.2 hrs) or 4U 1636-536 (3.8 hrs). A total of 28 type I X-ray bursts have been observed from XTE J1814-338 to date, all with burst oscillations in the vicinity of the 314 Hz pulsar frequency, confirming that the burst oscillation frequency for XTE J1814-338 is at the NS spin frequency (see, e.g., Watts et al. 2005). A source distance of 8 ± 1.6 kpc was inferred from the last burst, which likely reached the Eddington luminosity (Strohmayer et al., 2003).

The presence of ms pulsations provides the opportunity for a precise determination of the orbit of the neutron star (Papitto et al., 2007). However, in order to establish a complete set of system parameters, including the mass of the neutron star, the radial velocity curve of the companion is required. Optical and near-infrared observations of AMXPs in quiescence can offer promising opportunities to constrain the radial velocity of the donor, as the faint donor star may be detected directly. But so far, these have only led to upper limits

or a counterpart that is too faint on which to perform radial velocity studies (e.g. Homer et al., 2001; Jonker et al., 2003; Krauss et al., 2005).

We present medium resolution blue spectroscopy of the AMXP XTE J1814-338 obtained with the VLT during its 2003 outburst. The Bowen fluorescence technique is revisited and applied to XTE J1814-338 to establish dynamical system parameter constraints, which can offer insights into the evolutionary scenario involving binary pulsars. Section 4.2 summarizes the observing strategy and data reduction steps. In section 4.3 we present the average spectrum and main emission line parameters while radial velocities of emission lines are presented in section 4.4. In section 4.5, we exploit the Doppler tomography technique to obtain robust binary parameter constraints. Estimation of component masses and discussion of the results are given in section 4.6.

4.2 Observations and data reduction

We observed XTE J1814-338 (hereafter, J1814) using the FORS2 Spectrograph attached to the 8.2m Yepun Telescope (UT4) at Observatorio Monte Paranal (ESO) on the night of 23 June 2003 (programme 071.D-0372). A total of twenty spectra were obtained with the R1400V holographic grating, covering a complete orbital cycle using 700s long exposures. Matching with a 0.7 arcsec slit width resulted in a wavelength coverage of 4514-5815 Å at 70 km s^{-1} (FWHM) resolution. The seeing was variable between 0.6 arcsec – 1.2 arcsec during our run. The slit position angle was fixed to PA=100° which coincides with the parallactic angle at the end of our run, when the airmass of the target was highest (sec$z$ = 2.1). At the same time, two comparison stars were included in the slit, which enabled us to monitor slit losses and obtain a relative flux calibration. The flux standard Feige 110 was also observed with the same instrumental configuration to correct for the instrumental response of the detector.

The images were de-biased and flat-fielded, and the spectra were subsequently extracted using conventional optimal extraction techniques in order to optimize the signal-to-noise ratio of the output (Horne, 1986). A He+Ne+Hg+Cd comparison lamp image was obtained in the daytime to provide the wavelength calibration scale. A 4th-order polynomial fit to 19 arc lines produced an rms scatter < 0.05 Å with a mean dispersion of 0.64 Å pix^{-1}. Instrumental flexure was monitored through cross-correlation between the sky spectra and was found to be very small (always within 5 km s^{-1}). These velocity drifts were nevertheless removed from each individual spectra, and the zero point of the final wavelength scale was established by the strong O I sky line at 5577.338 Å. Individual spectra were corrected for slit losses using the brighter comparison star that shared the slit with our target. Correction factors were computed using a low-order spline fit to the ratio between each

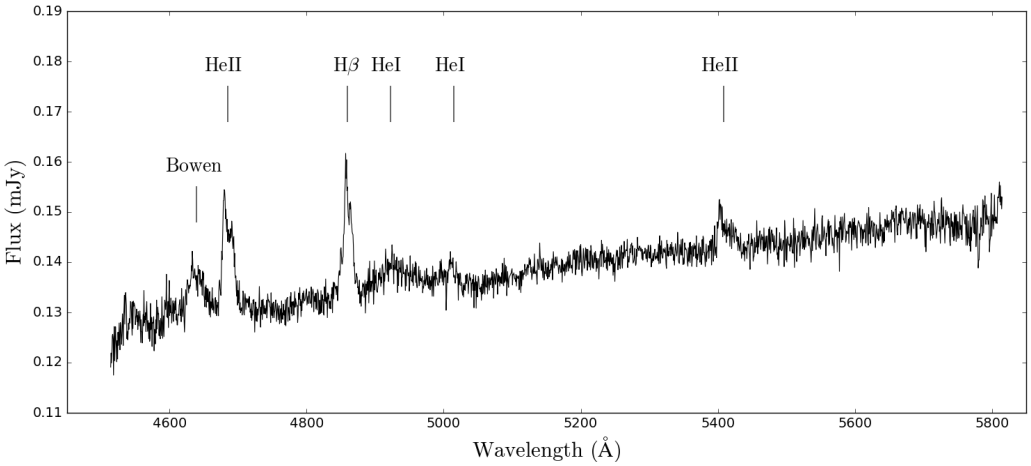

Figure 4.1: The average optical spectrum of XTE J1814-338. Main emission lines are indicated.

Table 4.1: Emission line parameters.

Line	Centroid Å	FWHM km s^{-1}	EW Å
Bowen	4639.0 ± 0.8	1613 ± 180	2.2 ± 0.2
He II	4684.6 ± 0.4	1160 ± 70	2.9 ± 0.2
Hβ	4859.7 ± 0.3	920 ± 60	2.8 ± 0.2
He II	5408.5 ± 1.7	1190 ± 200	0.8 ± 0.2

comparison star spectrum and its grand sum average. The target spectra were then divided by these fits to correct for time-dependent slit losses.

4.3 Average spectrum and orbital variability

The average spectrum of J1814 is presented in Fig. 4.1. The spectrum is dominated by high excitation emission lines of He II $\lambda\lambda$4686 & 5411Å, the Bowen blend at $\lambda\lambda$4630-50 Å and Hβ, which are typical of LMXBs and Soft X-ray Transients (SXTs) in outburst and first noted in Steeghs (2003b). He I lines at λ4922 and λ5015 are significantly weaker and no absorption components are discernible in the Balmer or He I lines, as seen in high inclination systems such as X1822-371 (see Casares et al., 2003). The He II profiles are double-peaked, as expected from an accretion disc, but the blue peak is considerably stronger than the red peak. The Hβ profile is more complex and its blue side peaks at lower velocities. A list of time-averaged emission line parameters is presented in Table 4.1.

Fig. 4.2 displays the orbital evolution of the most intense emission features presented in 15 phase bins. Binary phases were computed using the extremely accurate X-ray

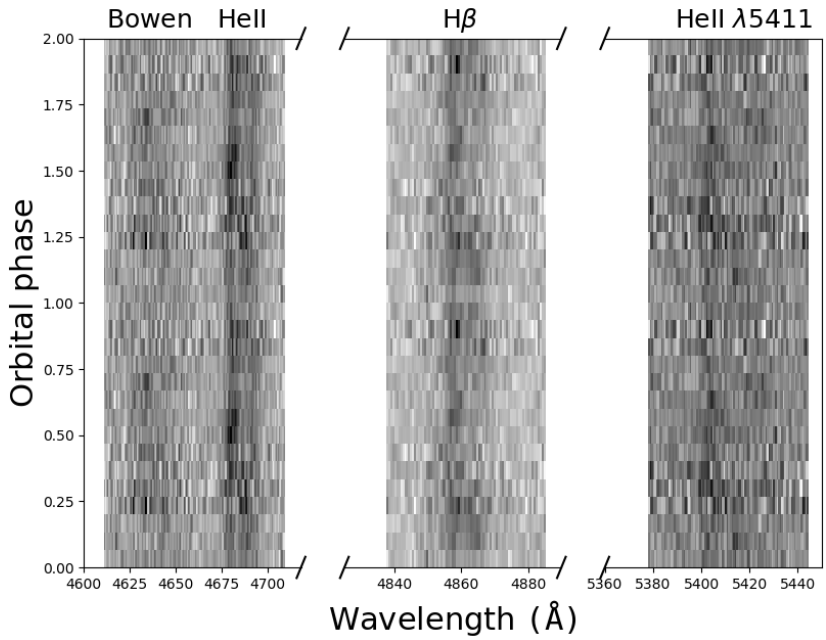

Figure 4.2: Trailed spectra showing the orbital evolution of the strongest emission lines in 15 phase bins.

pulsar orbital solution (Papitto et al., 2007) :

$$T_0 \text{ HJD(UTC)} = 2452798.3539536(9) + 0.178110219(2)\text{E}. \tag{4.1}$$

Here we adjusted T_0 such that phase 0 corresponds to the inferior conjunction of the companion star in a heliocentric UTC time system. He II λ4686 Å shows a clear double-peaked profile with the blue peak stronger around phase $\sim$ 0.6. An S-wave is visible, crossing from blue to red velocities at phase $\sim$ 0.9. The Hβ profiles are dominated by the blue peak throughout the orbit whereas the Bowen blend is too noisy to directly reveal any multi-component structure in the raw data. In general, the line intensities appear to peak in flux around phase $\sim$ 0.3 – 0.8.

4.4 Radial velocities and the systemic velocity

The broad disc emission features may be used to derive radial velocity curves as the disc gas should trace Keplerian orbits around the neutron star. In order to avoid contamination from line core components (see Fig. 4.2) we have applied the well established double-Gaussian technique (Schneider & Young, 1980) to He II λ4686. The Gaussian widths were fixed to

FWHM = 200 km s^{-1} with a variable separation a = 500 – 1800 km s^{-1} in steps of 100 km s^{-1}. The RV curves were fitted with a sine function and the resultant parameters are displayed using the traditional diagnostic diagram (Fig. 4.3; Shafter, 1985). As we move away from the line core and thus mainly probe the dynamics of the inner disc gas, the γ-velocity stabilizes towards −30 km s^{-1} (horizontal dash-dotted line). The radial velocity amplitude K drops from ∼ 150 to 50 km s^{-1}, and the phasing decreases from ∼ 0.85 to 0.5–0.6. From the pulsar solution we know the absolute phase (0.5) and velocity semi-amplitude of the neutron star (K_1 = 47.848±0.001 km s^{-1}, marked as horizontal blue lines in Fig. 4.3). It thus appears that in the range a ∼ 900 – 1200 km s^{-1}, the disc dynamics tracks the true orbit of the neutron star quite well. At larger separations, parameters deviate again due to increasing noise as we probe the faint line wings. Although we know K_1 already, this estimate suggests a systemic velocity near −30 km s^{-1}. In the next section, we present an alternative derivation of the systemic velocity using the new methodology, to be compared with the more traditional double Gaussian probe.

4.5 Analysis

4.5.1 Doppler mapping

The discovery of narrow, high-excitation Bowen emission lines arising from the irradiated donor star in Sco X-1 opened up a new window to achieve robust radial velocity studies in luminous LMXBs (Steeghs & Casares, 2002). Only in very few cases was it possible to use the conventional RV fitting method. For nearly all the fainter sources, the use of Doppler-tomography based methods was required in order to detect Bowen emission from the donor at low SNRs (S/N < 10).

For J1814, we first prepared the spectra by subtracting a low order spline fit to the continuum regions, and subsequently used the second generation (Python/C++ based), maximum entropy Doppler tomography code developed by T. Marsh (Manser et al., 2016) to exploit all 20 spectra simultaneously. In Fig. 4.4, we show the Doppler tomograms of the principal lines seen in our spectra using the ephemeris in equation (4.1) and γ = −30 km s^{-1}.

Both He II and Hβ maps show the classic ring-like features corresponding to emission from the accretion disc. An extended bright spot can be seen in the upper left velocity quadrant of these maps, suggesting excited emission from the stream-disc impact region. In addition to evidence of bright spot emission, the map of N III λ4640 (usually the strongest Bowen component) for J1814 reveals a sharp spot along the positive V_y-axis. The centroid is at the position V_x ∼ −20 km s^{-1} and V_y ∼ 319 km s^{-1}. The shape and phasing of this spot feature suggest that we may have detected a signal from the irradiated companion. Finally,

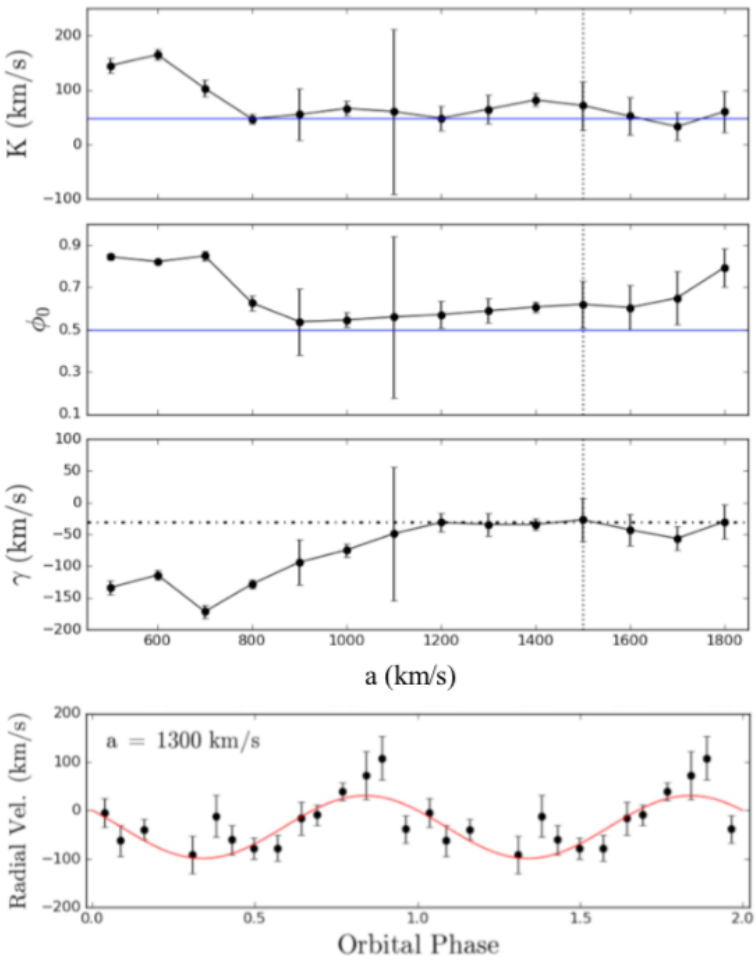

Figure 4.3: The diagnostic diagram of He II λ4686 (top 3 panels). Fitted sine-wave parameters (with 1σ errors) are plotted as functions of the Gaussian separation a. The vertical dotted line denotes a limit of the Gaussian separation above which the continuum noise dominates the radial velocities. The bottom panel shows the radial velocity curve for a = 1300 km s^{-1} overplotted with the best-fit sine wave (red curve).

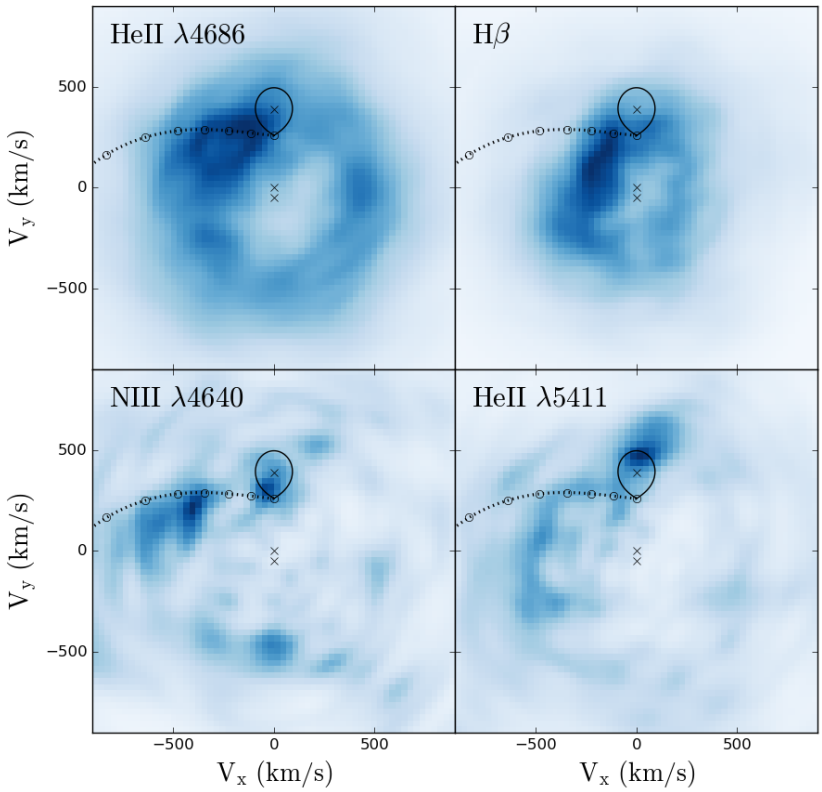

Figure 4.4: Doppler maps of several spectral features. All images were computed for a systemic velocity $\gamma = -30$ km s^{-1}. We plot the gas stream trajectory and the Roche lobe of the donor star using $K_1 = 47.848$ km s^{-1} and our best estimate of the mass ratio of 0.123 (see section 4.6.2). The centre-of-mass velocity of the mass donor (0, $K_2 = 390$ km s^{-1}), the center of mass of the system (0, 0) and the velocity of the neutron star (0, -K_1) are denoted by crosses.

we notice another bright spot at approximately the expected phase of the companion in the He II λ5411 map, the spot is clearly at a much larger velocity ($V_x \sim 30$ km s^{-1}, $V_y \sim 483$ km s^{-1}) and more extended than the N III λ4640 spot.

4.5.2 Bootstrap Monte-Carlo

Significance testing

Perhaps the most important step towards robust binary parameter estimation using the Bowen technique involves confirming the statistical significance of any donor star components and to determine their position in velocity space robustly. This becomes increasingly difficult as we push into lower SNR regimes, with correspondingly noisier Doppler maps that may contain spurious features. Therefore, it is vital to test the significance of the features seen in the N III λ4640 and He II λ5411 maps of J1814, before carrying out further rigorous analysis based on our reconstructions.

We have opted to use the robust and versatile bootstrap technique to derive estimates of the standard deviation and confidence intervals on a real dataset with unknown probability distribution function (Watson & Dhillon, 2001; Longa-Peña et al., 2015). Only the error bars of the observed data were manipulated to allow for approximately the same noise level to be present in the bootstrap dataset as in the original data (see details in Watson & Dhillon, 2001). For each bootstrap dataset, we compute a reconstructed image (automated processes; see 2.2.1) in the same manner as for the original image.

Upon creating a large number of new maps by resampling from the original trailed spectra, histograms of spot parameters can be constructed from ensembles of 2D Gaussian fits. The histograms provide information about the unknown sampling distribution of each property, including the centroid position, peak intensity, and FWHM. In this analysis, all errors and significance levels are calculated from more than 2000 bootstrap samples with maps iterated to reach the *same image entropy*.

Confirmation of the donor signature

We start by estimating the significance of the most promising feature present in the N III λ4640 Doppler map as well as the statistical error of the phase shift relative to the pulsar ephemeris. It is known that the choice of the input parameter γ can have an impact on the final Doppler image. In cases of high spectral resolution and high SNRs, an independent estimate of γ can be obtained by reconstructing a series of maps with a range of γ's, and searching for the one that yields the best fit to the data (minimal χ^2), as well as an ideal, artifact-free image (Steeghs, 2003a).

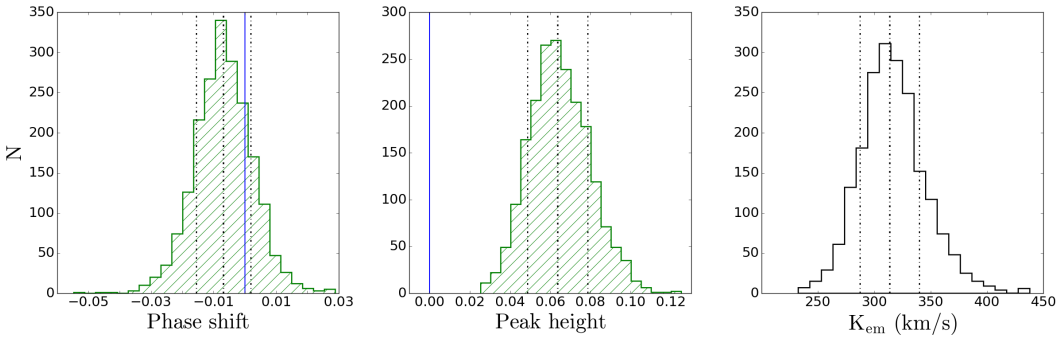

Figure 4.5: Number distributions of the phase shift (left), peak emission (middle) and radial velocity semi-amplitude (right) measured from 2000 bootstrap maps assuming a systemic velocity of −30 km s^{-1}. All maps were set to reach approximately the same entropy (S = −0.02). Dashed lines indicate the mean and the ± 1σ confidence intervals. The phase shift relative to the pulsar ephemeris is consistent with zero (blue solid line), and the emission feature is significant at a ∼4.2σ level.

In the case of J1814, we also generated a series of N III λ4640 maps with γ varying from −200 to 200 km s^{-1} in steps of 5 km s^{-1}, but found no pronounced minimum in χ^2. Reduced χ^2 remained low ($\chi^2_\nu < 1.4$) for γ between −200 and 30 km s^{-1}. Based on this test, we conclude that the systemic velocity is indeed more likely to be negative, but that our SNR is too low to permit us to tightly constrain γ. Among our N III λ4640 maps, only a subset (γ between −60 and 10 km s^{-1}) reveals a sharp, Gaussian-type spot feature along the positive V_y-axis, which we interpreted as a possible donor signature. Thus we choose to consider all reconstructions within this γ range in the subsequent analysis. To suppress the noise and enhance signal strength, we also created the *combined Bowen Doppler maps*, for which we included both the N III λ4640 and the N III λ4634 components[1]. The combined Bowen map is almost identical in structure with the N III λ4640 map (see Fig. 4.4).

In Fig. 4.5, we give examples of histograms, for a $\gamma = -30$ km s^{-1} case, representing the bootstrap distribution of three important spot properties obtained from the *combined* Bowen map.

Firstly, the bootstrap test allowed us to derive a phase shift (with its 1σ statistical error) of $\Delta\phi_{\rm spot} = -0.007 \pm 0.009$ ($-2.5 \pm 3.1°$) using the centroid position (V_x, V_y). Given that the binary ephemeris is accurately known thanks to the pulsar, we can thus formally demonstrate that the sharp Bowen spot is effectively centred on the V_y-axis, exactly where the donor star should appear.

Secondly, since all the distributions we obtained (see, e.g., Fig. 4.5) were Gaussian, we estimated the mean and 1σ error of the emission peak (and all the other spot parameters)

[1]Relevant Bowen components (other than the N III λ4640 line) may be identified by creating a trial Doppler corrected average spectrum in the rest frame of the donor.

by fitting a Gaussian curve to the histogram plots. The centre of the peak height distribution (0.064 ± 0.015) for $\gamma = -30$ km s^{-1} is different from zero at the $4 - 4.5\sigma$ level, indicating a significant detection (99.99% confidence).

It can be shown using the same method that the bright spot in the upper left velocity quadrant is also significant at the 4.4σ level, and likely originates from the stream-disc impact region. A third faint spot occurs on the negative V_y-axis, with a marginal significance level of 3.2σ, the location suggests that it could be part of a broken-ring-like feature corresponding to the accretion disc. The significance levels of the rest of the spots are all below 2σ. In summary, although several spot-like features are present in the noisy N III λ4640/combined Bowen maps, only one sharp feature (statistically significant at the $> 4\sigma$ level) lies in the positive V_y direction ($V_x = 0$ km s^{-1}) and thus can be confidently identified as the donor signature in the case of J1814. The availability of a robust absolute ephemeris in this case simplifies the search, but our methodology is appropriate even in cases where such an ephemeris may not be available and thus all statistically significant components need to be considered (see also Chapter 3).

4.5.3 The Bowen blend diagnostic

Along with the phase shift and peak emission, we show the distribution of the corresponding apparent radial velocity semi-amplitude K_{em} ($< K_2$) in Fig. 4.5. By fitting a Gaussian model to the histogram, we obtain $K_{em} = 313 \pm 26$ km s^{-1}. Similar analyses were applied to all the other N III λ4640 and the combined Bowen maps computed using the previously determined range of γ, and the results can be summarized in the form of a Bowen diagnostic diagram (Fig. 4.6).

Systemic velocity

In the new diagnostic diagram (compared with Figure 4.3), we plot the phase shift, K_{em} velocity (with 1σ statistical errors) and the significance level of the combined Bowen spot feature as functions of the assumed γ. Due to the low SNR of our data, we did not find a satisfactory γ range that would minimise the reduced χ^2 of a series of reconstructions (sensitivity to γ is weak). Nevertheless, the map reveals a real donor signature, mapped from one or more sharp S-wave component(s) present in the trailed spectra, we can therefore expect that the best estimate of γ would yield the maximum significance of the secondary feature.

From the bottom panel of Fig. 4.6, it is clear that the significance of the combined Bowen spot is consistently higher than that of the N III λ4640 spot, signifying the merit of assigning multiple Bowen transitions to one image. In both cases, the level of significance

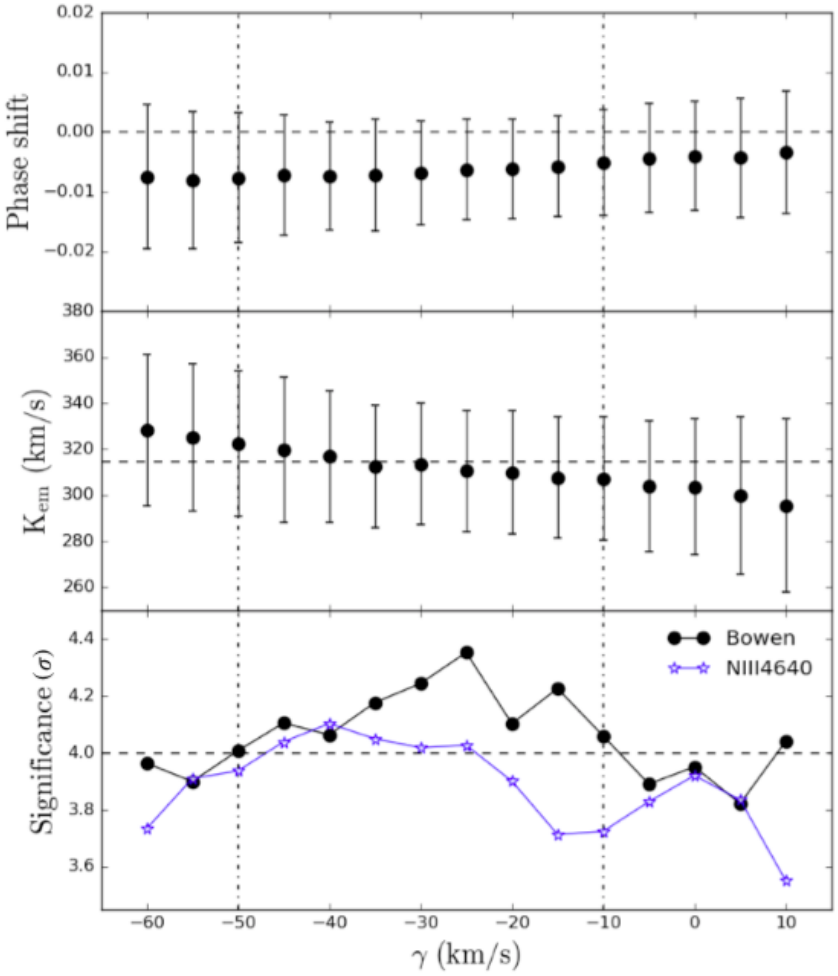

Figure 4.6: Diagram showing the best-fit solutions of the phase shift, K_{em} amplitude with bootstrap estimate of 1σ errors, and significance level of the donor spot feature derived from Bowen (black-filled circles) and N III λ4640 (blue stars) maps, as a function of the assumed systemic velocity. Vertical dash-dotted lines mark the preferred range of γ, over which the statistical significance of the secondary feature is greater than 4σ.

peaks near the mid-point of the γ range. As a final step in constraining the systemic velocity, we select a range (indicated by vertical dash-dotted lines) over which the significance of the Bowen spot is greater than the 4σ level (horizontal dashed line). Hence, we use the combined Bowen spot and focus only on this final range of γ (γ =-30 ± 20 km s^{-1}) for deriving the RV semi-amplitude.

K_{em} velocity

The middle panel of Fig. 4.6 shows that within the preferred γ range, K_{em} amplitude is very weakly dependent on the underlying γ assumption, with a maximum of 8 km s^{-1} drift around the central value of 315 km s^{-1} (marked by a horizontal dashed line). We therefore conclude that at low SNRs it is clearly the case that the systematic uncertainty due to our assumption of γ is subdominant. Using the information from the diagram, we derive the best estimate of

$$K_{em,\,doppler} = 315 \pm 28\ (stat) \pm 8\ (syst)\ km\ s^{-1}.$$

By running the same analysis, we could also confirm the significance (4.2 – 4.7σ level) of the He II λ5411 spot, and the phasing constraint [$\Delta\phi_{spot}$ = 0.009 ± 0.009 (stat) ± 0.002 (syst)] points to the inner Roche lobe of the donor star as a possible reprocessing site. However, we derived a velocity semi-amplitude significantly higher (3.3σ) than the Bowen K_{em} velocity: $K_{em,\,He\,II}$ = 477 ± 29 (stat) ± 27 (syst) km s^{-1}. We initially considered whether the He II λ5411 emission component could also come from the irradiated companion, albeit a different region of the Roche lobe – possibly due to differential shielding by the accretion disc. We then used the numerical solution for K_{cor} ($\alpha = 0°$) derived in Muñoz-Darias et al. (2005), for the lower inclination angle case (deduced from the lack of X-ray eclipses), to perform a K-correction for both K_{em} velocities.

4.6 Discussion

4.6.1 The K-correction

As the velocity amplitude of the neutron star (K_1 = 47.848 ± 0.001 km s^{-1}) is accurately known from the pulsar solution, the upper and lower limits for q inferred from the Bowen and the 5411 Å spot can be easily visualized in a K_1 – q plane (Fig. 4.7). Not surprisingly, the two significantly different radial velocities with their associated errors (by adding the statistical and systematic uncertainties in quadrature) had led to very different constraints of q (denoted by grey and blue shaded regions for the Bowen and He II λ5411 spot, respectively). Since there is no overlap between these shaded areas, there exists no value of q that

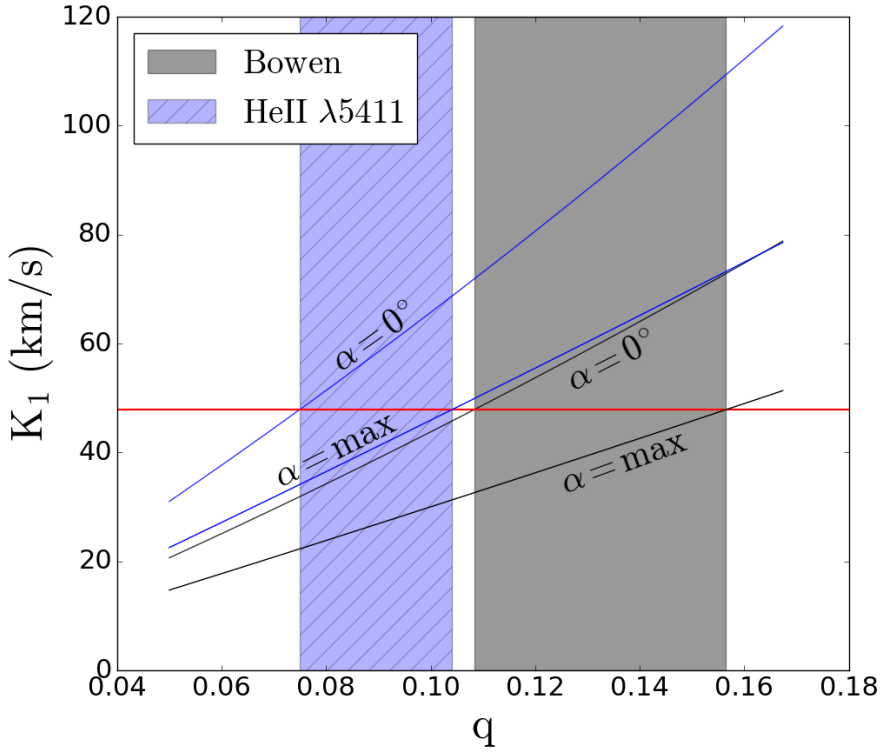

Figure 4.7: Constraints on q using the K amplitude derived from the Bowen (grey shaded region) and He II λ5411 spot (blue shaded region). The disc flaring angle must be between $\alpha = 0°$ and maximum, and the solutions for the Bowen and He II λ5411 spot are shown as black and blue curves, respectively. The horizontal red line denotes the estimate of K_1 from the pulsar solution.

would satisfy both velocity constraints at the same time, i.e., only one of the two emission spots can originate from the surface of the donor. We must therefore focus on the K_{em} velocity which most certainly traces the orbit of the companion to derive a feasible set of parameter constraints.

Previous studies have shown that the irradiated atmospheres of the companion star in many LMXBs are powerful emitters of the fluorescence N III components. Since we have verified that narrow lines are also present in the Bowen region of J1814, we may, by extension, attribute them to the donor. A further support to this hypothesis is provided by the correct phasing and the $>4\sigma$ significance level of the relevant spot feature in the reconstructed Doppler map. Similar to most of the other Bowen targets, the strongest component around 4630-4650 Å is N III λ4640, which only becomes visible in the Doppler corrected average spectrum (Fig. 4.8). Therefore we are confident that the grey region ($0.108 < q < 0.157$) in Fig. 4.7 represents a reliable range of the mass ratio for J1814. Following this argument, we rule out the possibility that the component detected in the 5411 Å emission profile comes from the X-ray illuminated front face of the companion. A tentative scenario for the origin of He II λ5411 emission is proposed in section 4.6.4.

4.6.2 Binary parameter estimation

The detection of Bowen emission lines in J1814 opens up a special opportunity to constrain the radial velocity of the companion star (K_2), and thereby the mass of the accreting millisecond pulsar (M_1) via the mass function equation (equation 1.17). The observed lower limit to K_2 ($K_{em} = 315 \pm 29$ km s^{-1}), combined with the precise determination of K_1, delivers an absolute upper limit to the mass ratio of $q < 0.167$, which implies, using Paczyński's approximation: $\sin(\alpha_{max}) \simeq R_2/a \simeq 0.462q^{1/3}/(1+q)^{1/3}$ (Paczyński, 1971), that the disc opening angle α cannot be higher than $\sim 14°$.

With the measurements of the binary orbital period (P_{orb}) and the projected radial velocity semi-amplitude K_2, equation (1.17) gives the minimum allowable mass of the compact primary M_1 (as $\sin(i) \lesssim 1$ and $1+q > 1$). Precise determinations of stellar masses require knowledge of the mass ratio q as well as the inclination angle i.

Monte-Carlo analysis

We performed a Monte Carlo analysis, and considered a random distribution of inclination angles to establish PDF's of the unknown system parameters. By selecting synthetic K_{em}, K_1 and P_{orb} values from a Gauss-normal distribution (with a mean and 1σ error equal to the observed values; see Table 4.2), a set of simulated data can be obtained at each Monte Carlo trial and used as inputs to equation (1.17). Since a firm lower limit on α for J1814

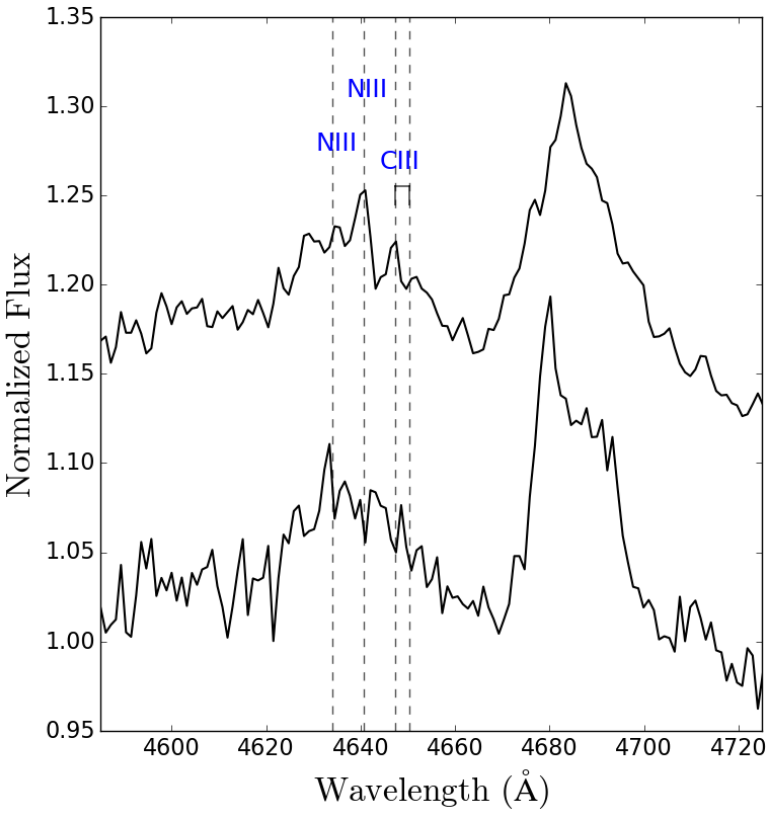

Figure 4.8: The Bowen/He II region of the average spectrum in the rest frame of the companion (*top*) compared with a straight average spectrum (*bottom*). At least three narrow peaks corresponding to known N III/C III transitions (vertical dashed lines) emerge in the Doppler corrected average. Top spectrum was calculated using the K_{em} amplitude and the systemic velocity values reported in Table 4.2.

is not known, we chose to let α follow a uniform distribution between 0 and 14°. A value as low as zero is perhaps unlikely given the presence of an active accretion disk, but we prefer not to bias our results by adopting some ad-hoc estimate of α. For every combination of randomly generated K_{em}, K_1 and α values, we determined an accurate K-correction for the α angle using the previously developed approximation tool. The updated K_{cor} was then applied to K_{em}, followed by evaluation of the solution for the binary mass ratio and the corresponding true K_2.

With a set of synthetic q, K_2 and P_{orb} in place, we proceeded to calculate a lower limit to the inclination angle by assuming a maximum stable neutron star mass of 3.2 $M_\odot$. The upper limit to i was simply estimated based on Paczyński's relation given the absence of X-ray eclipses (Krauss et al., 2005). This would result in an overall very loose constraint on the inclination, $35° \lesssim i \lesssim 78°$, by combining Bowen K_{em} velocity with $M_1 < 3.2\ M_\odot$ and using the knowledge of lack of X-ray dips. Therefore, during the last step, we used a uniform distribution for $\cos(i)$ (between the lower and upper bounds set by the particular combination of input values) to select a random inclination angle for deriving component masses. The same process was simulated 10^6 times. Finally, the large number of separate outcomes evaluated in individual trials were assembled into PDF's presented in Figures 4.9 and 4.10.

The binary mass ratio and component masses

Perhaps the main disadvantage of the Bowen fluorescence technique lies in the fact that the measured K_{em} velocity represents only a solid lower limit to K_2. However, in this case, we have the significant advantage of knowing the radial velocity semi-amplitude of the neutron star K_1 very accurately. As a result, both K_2 and q PDF's (see Fig. 4.9) display near Gaussian distributions under the assumption of randomly distributed inclinations. By propagating the uncertainties in all estimated quantities – including especially the full uncertainty in the opening angle of the accretion disc and the systemic velocity – into the errors in the output quantities, we were able to derive robust estimates of the true velocity semi-amplitude of the donor star and the binary mass ratio (with 1σ errors of less than 10% for both parameters):

$$K_2 = 390^{+35}_{-36}\ \mathrm{km\ s^{-1}},$$
$$q = 0.123^{+0.012}_{-0.010}.$$

Additionally, a lower limit to the inclination for an assumed pulsar mass of 1.4 $M_\odot$ can be established ($i \gtrsim 48°$) from $K_2 > K_{em} = 315 \pm 29$ km s^{-1}. The most secure constraint on i (as shown in Fig. 4.10) would be $35° < i < 78°$ using the knowledge of lack of X-ray dips and combining Bowen K_{em} velocity with $M_1 < 3.2\ M_\odot$. This new inclination

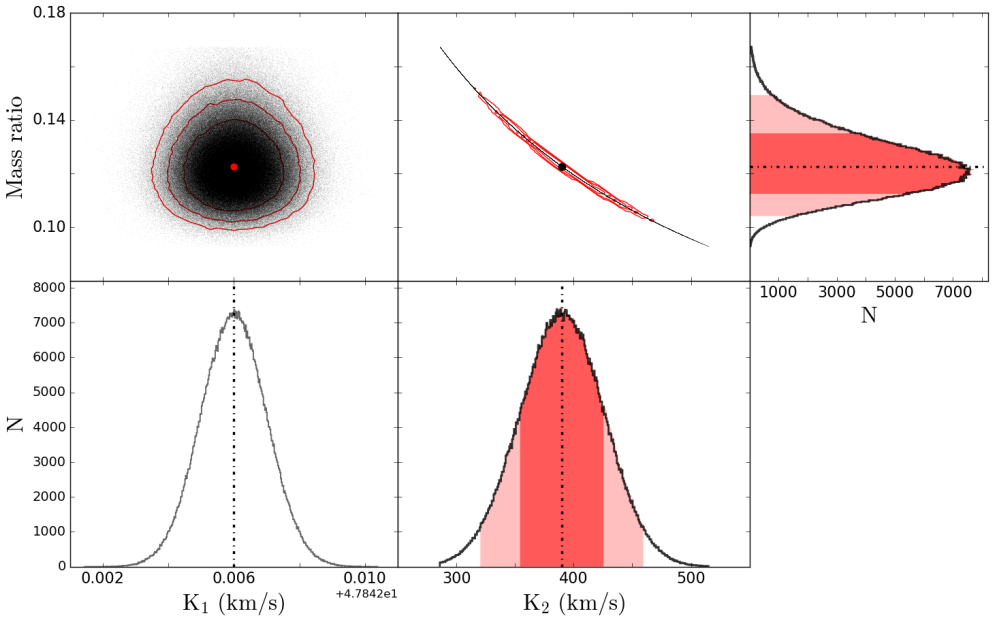

Figure 4.9: Probability density functions of K_2 and q derived from our Monte Carlo analysis (10^6 trials) for $35° \leq i \leq 78°$. Dash-dotted lines denote the locations of the median (50^{th} percentile). Red-shaded areas correspond to the regions between the 2.5^{th} and 97.5^{th} percentiles. 68% of the data fall within the darker regions. Best estimates of these system parameters and their associated 1σ errors are given in Table 4.2.

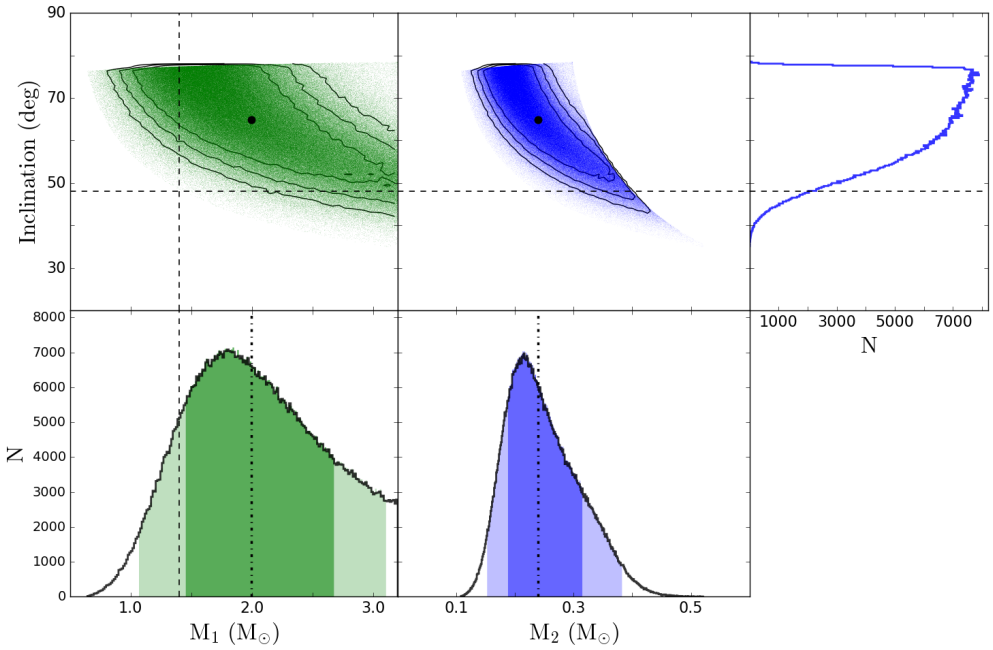

Figure 4.10: PDF's of the masses of the stellar components. The median values are denoted by dash-dotted lines. As in the previous PDF's, dark/light areas correspond to the regions between the $16^{\text{th}}/2.5^{\text{th}}$ and $84^{\text{th}}/97.5^{\text{th}}$ percentiles. The canonical value for the neutron star mass (1.4 $M_{\odot}$), denoted by a vertical dashed line, lies just outside the 68% confidence limits. The horizontal dashed line denotes the lower limit to the inclination angle ($i \gtrsim 48^{\circ}$) for an assumed pulsar mass of 1.4 $M_{\odot}$.

Table 4.2: XTE J1814-338 system parameters with estimates of 1σ/68% uncertainties.

Parameter	Value
P_{orb} (d)[a]	0.178110219(2)
T_0 HJD(UTC)[a]	2452798.3539536(9)
γ (km s^{-1})	-30 ± 20
K_{em} (km s^{-1})	315 ± 28 (statistical) ± 8 (systematic)
K_1(km s^{-1})[b]	47.848 ± 0.001
K_2 (km s^{-1})	390^{+35}_{-36}
q (M_2/M_1)	$0.123^{+0.012}_{-0.010}$
i (°)	35 - 78
M_1 ($M_\odot$)	$2.0^{+0.7}_{-0.5}$
M_2 ($M_\odot$)	$0.24^{+0.08}_{-0.05}$

Notes.
[a]Adapted from Papitto et al. (2007)
[b]Based on Papitto et al. (2007)

constraint thus provides a tighter lower bound compared with previously obtained limits based on burst oscillation properties ($26° < i < 50°$; Bhattacharyya et al., 2005), or by assuming a magnitude limit (R > 23.3) of the companion during quiescence ($22° < i < 77°$; Krauss et al., 2005).

Fig. 4.10 shows the negative correlation between the inclination and the component masses, M_1 and M_2. The projected 1-dimensional PDF of the companion mass (M_2) has a tail extending to 0.38 $M_\odot$ (95% confidence) and a lower 95% confidence limit of 0.15 $M_\odot$, which coincides with the minimum companion mass estimated from the pulsar mass function (Markwardt et al., 2003). The 68% CI for M_2 ($0.24^{+0.08}_{-0.05}$ $M_\odot$) is also in excellent agreement with the M_2 constraints deduced from studies of the quiescent optical counterpart of J1814 (D'Avanzo et al., 2009; Baglio et al., 2013).

The much wider M_1 PDF peaks beyond 1.4 $M_\odot$ ($2.0^{+0.7}_{-0.5}$ $M_\odot$; 68%). We note that the canonical mass of 1.4 $M_\odot$ is not ruled out ($1.1 \lesssim M_1 \lesssim 3.1$; 95%) with the lack of knowledge of i, and that a canonical NS mass would be more compatible with a relatively high inclination angle ($63° \lesssim i \lesssim 76°$; 68%). We already know that extremely high-mass neutron stars exist from the precise determinations of the mass of two radio millisecond pulsars, PSR J1614-2230 (M_1 = 1.928 ± 0.017 $M_\odot$; Demorest et al. 2010; see also Fonseca et al. 2016) and PSR J0348+0432 (M_1 = 2.01 ± 0.04 $M_\odot$; Antoniadis et al. 2013). An improvement in the measurement of the binary inclination is the key factor in achieving a tighter M_1 constraint for J1814, which may have the potential to exclude some soft equations of state. A summary of system parameters with estimates of 1σ uncertainties is given in Table 4.2.

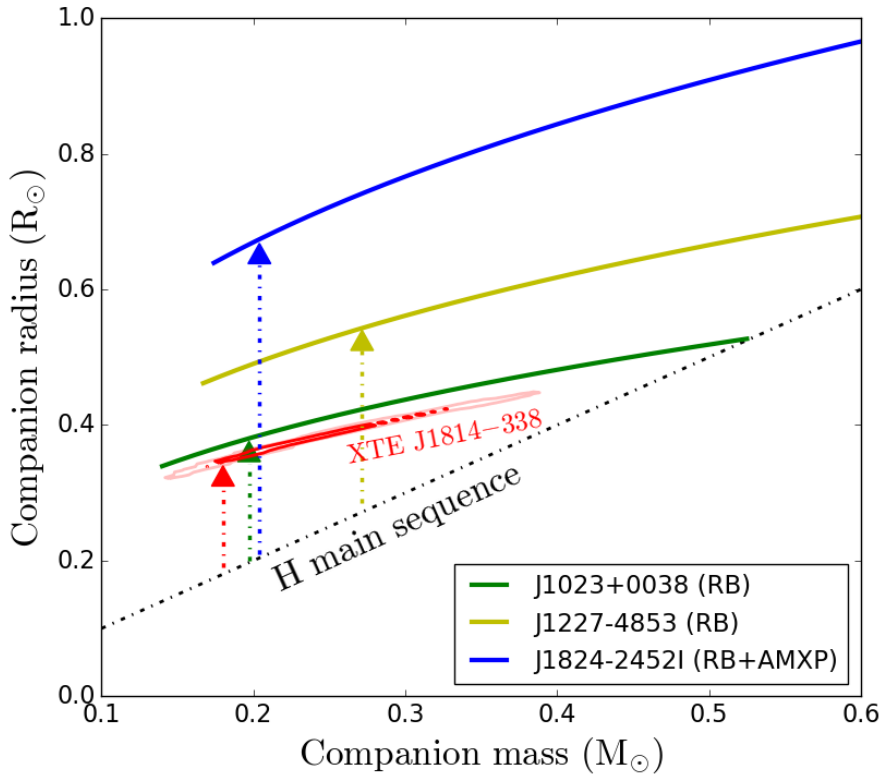

Figure 4.11: A comparison of the mass-radius relationships for the companion of J1814 and 3 t-MSPs (so far all 3 are redbacks (RBs); see e.g. Archibald et al., 2009; Papitto et al., 2013; Stappers et al., 2014; Bassa et al., 2014) with the approximate relation for ordinary low-mass hydrogen main-sequence stars. The 68% and 95% confidence regions for J1814 (red contours) exclude the mass-radius relation for hydrogen main-sequence stars, indicating that the companion must be bloated. Dash-dotted lines with arrows denote nominal M_2 values determined for a pulsar mass of 1.4 $M_\odot$.

4.6.3 The nature of the companion

Fig. 4.11 compares the mass-radius contours (showing the 68% and 95% confidence regions) for a Roche lobe-filling donor in a 4.275 hr binary (J1814) with the approximate relation for ordinary low-mass hydrogen main-sequence stars (using R/R$_\odot$ = M/M$_\odot$; black dash-dotted line). Our dynamical mass constraints confirmed previous suggestions of a main-sequence M-type companion in J1814, and that the companion is likely significantly bloated (given the 68%/95% confidence regions) presumably due to X-ray heating by an accretion-powered millisecond pulsar (see also Krauss et al., 2005; Bhattacharyya et al., 2005).

The fact that the radius of the secondary is ≈ 90% larger than expected (assuming M_2 = 0.18 M$_\odot$ for a 1.4 M$_\odot$ neutron star) is reminiscent of the first known transitional mil-

lisecond pulsar binary (t-MSP) PSR J1023+0038 (Archibald et al., 2009). This archetypal redback system (an eclipsing binary MSP with a companion of $\gtrsim 0.1\ M_{\odot}$; Roberts, 2011) in the Galactic field has a similar orbital period to J1814 (green mass-radius curve in Fig. 4.11) and a main-sequence-like, similar mass companion ($\sim 0.2\ M_{\odot}$) that is bloated to ≈ 1.9 times the expected radius. Given these remarkable similarities, it is intriguing to speculate that before the 2003 outburst, the companion of XTE J1814-338 may have been irradiated by a rotation-powered ('recycled') **redback-like** pulsar which switches on during an X-ray quiescent state. Ablation processes driven by the pulsar spin-down power could bloat the secondary star significantly.

4.6.4 A hidden 'redback'?

Evidence has been built over the past two decades to indicate strongly irradiated companions of several AMXP systems during quiescence. Optical light curves of SAX J1808.4-3658, IGR J00291+5934 and XTE J1814-338 all showed large-amplitude, sinusoidal modulations at the known orbital period (Homer et al., 2001; Campana et al., 2004; D'Avanzo et al., 2007, 2009). As first pointed out by Burderi et al. (2003), the irradiating luminosity necessary to account for the observed optical flux is about two orders of magnitude *higher* than the quiescent X-ray luminosity L_X ($\lesssim 10^{32}$ erg s^{-1}). On the other hand, the release of rotational energy via a relativistic particle wind (the spin-down luminosity; ; $L_{sd} \sim 10^{34}$ erg s^{-1}) by a reactivated radio pulsar would be sufficient to illuminate the companion (Hartman et al., 2008).

From fitting multi-band, quiescent optical light curves of J1814 using a model for an irradiated secondary, Baglio et al. (2013) noted an apparent discrepancy between the inferred value of M_2 (consistent with the companion being an M-type main-sequence star) and the day-side surface temperature of the companion ($\sim$ 5500 K), which is typical of an earlier spectral type (G or K-type) star (see also D'Avanzo et al., 2009). By assuming that the relativistic wind of an active radio pulsar irradiates the companion and increases its surface temperature, an estimate of the irradiation luminosity, $L_{irr} = \sigma_{SB}(T^4_{day} - T^4_{night})$, can be related to the pulsar's spin-down energy as $L_{sd} = 4\pi a^2 L_{irr}/\epsilon_{irr}$, where σ_{SB} is the Stefan-Boltzmann constant, a is the orbital separation and ϵ_{irr} is the irradiation efficiency. For an efficiency in the range of 0.1 to 0.3 typical of irradiated black widow ($M_2 << 0.1\ M_{\odot}$) and redback MSP systems (Breton et al., 2013), the derived value of L_{sd} ($\sim [6 - 17] \times 10^{34}$ erg s^{-1}) is consistent with the spin-down luminosity of a 3.2 ms pulsar (Baglio et al., 2013). This finding, combined with the new dynamical mass constraints and the bloated nature of the companion, provides indirect evidence of a redback MSP during quiescence in XTE J1814-338 (although no evidence of pulsed radio emission of this source has been reported to date).

The presence of a redback MSP might shed some light on the emission spot seen in the Doppler map of He II λ5411 in Fig. 4.4. Since its V_y-coordinate is larger than the upper limit to K_2 derived from the N III λ4640/Bowen spot, it cannot be produced on the irradiated surface of the donor. Noticeable differences between the shape (or FWHM) of the He II λ5411 and the N III λ4640 spot suggest that the former might instead arise from a more extended structure, perhaps an intra-binary shock caused by the pulsar wind interacting with the ablated material from the donor. A puzzling behaviour that may be explained by the presence of a shock front was also noted by D'Avanzo et al. (2009). Quiescent optical light curves of J1814 exhibit a decrease in the V-band flux between phase 0.05 and 0.17. The deep minimum around phase 0 (inferior conjunction of the donor star) is likely caused by a shock front eclipsing a residual accretion disc if present during quiescence, as suggested in Baglio et al. (2013).

Chapter 5

Sco X-1

Based on:

Wang L., Steeghs D., Galloway D. K., Marsh T. R., Casares J.; *Precision ephemerides for gravitational-wave searches – III. Revised system parameters of Sco X-1*; submitted to MNRAS.

5.1 Introduction

Sco X-1 was the first LMXB discovered outside the Solar System (Giacconi et al., 1962) and the brightest persistent X-ray source in the sky. The orbital period of 18.9 hr was first reported by Gottlieb, Wright, & Liller (1975) from photometry of the optical counterpart V818 Sco (V $\sim$ 12.5) using 1068 plates spanning over 84 yr. Bradshaw, Fomalont, & Geldzahler (1999) measured the trigonometric parallax from Very Long Baseline Array (VLBA) radio observations, and obtained a distance of 2.8 $\pm$ 0.3 kpc. Further observations revealed the presence of twin radio lobes, which led to an estimate for the inclination of 44° $\pm$ 6°, assuming that the radio jet is perpendicular to the orbital plane (Fomalont, Geldzahler, & Bradshaw, 2001). It is believed to harbor a NS based on its X-ray behavior. However, no coherent pulsations or bursts have been observed so far from this source.

Sco X-1 has been a prime target for continuous GW searches for the Laser Interferometer Gravitational-Wave Observatory (LIGO). Due to its relative proximity to Earth and high mass accretion rate, it is predicted to be the strongest GW emitter among the family of known LMXBs within the relevant frequency passband (Abbott et al., 2007). Many directed GW searches on Sco X-1 have been carried out. So far only upper limits on the signal amplitude have been obtained. A key difficulty in searching for the GWs emitted by NSs in LMXBs is the lack of precise knowledge about the position and velocity of the NS in the binary orbit (Watts et al., 2008). Searching over possible values of unknown param-

eters carries a cost in a computationally-bound search, and many methods carry a trade-off between computational cost and sensitivity. The smaller the parameter space region that needs to be searched, the more sensitive the search can be made, given fixed computing resources.

The most important orbital parameters required by most directed searches include the orbital period (P_{orb}), the absolute phase of the system (for which we quote the epoch of inferior conjunction of the companion star T_0), and the eccentricity e (e.g., Watts et al. 2008). The projected semi-major axis of the NS ($a_x \sin i$) must also be searched over (Messenger et al. 2015; Leaci & Prix 2015; Whelan et al. 2015; Meadors et al. 2016; Sammut et al. 2014), and is related to the amplitude of the projected orbital velocity of the NS, K_1 (or $v_x \sin i$), as $K_1 = 2\pi\ a_x \sin i / P_{orb}$. For systems in active states, the optical emission is dominated by the reprocessing of hard X-rays in the outer accretion disc, which severely hampers the detection of the much fainter companion. A recent study by Mata Sánchez et al. (2015) found no evidence of companion spectral features for Sco X-1 even in the near-infrared (where the companion star could make a substantial contribution).

Galloway et al. (2014) (hereafter G14) presented the results of a pilot program for improving the precision of the orbital period and ephemeris of Sco X-1, using the proven Bowen diagnostic of the mass donor. In this follow-up study to G14, we provide revised constraints on key orbital parameters in direct support of GW observations of Sco X-1 in the Advanced-LIGO era.

5.2 Source data and RV determination

This study makes use of all available spectroscopic data previously obtained for Sco X-1 and initially presented in SC02 and G14. Two epochs of data separated by 12 years (1999 – 2011) were obtained using the Intermediate dispersion Spectrograph and Imaging System (ISIS) at the 4.2m William Herschel Telescope (WHT). In addition, Sco X-1 was observed at 44 random epochs between 2011 May 29 – August 23 with the Ultraviolet and Visual Echelle Spectrograph (UVES) on the European Southern Observatory (ESO) Very Large Telescope (VLT; programme 087.D-0278). The superior quality of the combined dataset allowed the application of several techniques for obtaining binary parameter constraints, enabling us to go beyond the initial results provided in G14. Table 5.1 shows a summary of source data. We used data available in the reduced form as input for our analysis. For details of the observations and data reduction procedures, we refer to SC02 and G14.

We first reanalyzed the Bowen emission components from the irradiated front face of the donor using the well-established radial velocity fitting method. Following SC02

Table 5.1: Observations of Sco X-1.

Date	Instrument	$N_{\rm obs}$	Phase coverage	Resolution (Å)	Reference
1999 Jun 28–30	ISIS/WHT	137	75%	0.84	SC02
2011 Jun 16–18	ISIS/WHT	157	75%	0.32	G14
2011 May 29–Aug 23	UVES/VLT	44	34%	0.1	G14

and G14, we used the MOLLY[1] *mgfit* routine for fitting multiple Gaussians to time-resolved, continuum-normalised spectra and (for each Bowen profile) measuring the common RV of the three strongest narrow lines (N III $\lambda\lambda$4634 & 4640Å and C III λ4647). For the WHT data, we used the same multi-Gaussian model (with 6 free parameters) as was used in SC02 and G14. It is known that during certain phase ranges, especially near phase zero, the narrow lines could be much weaker than at other phases. The weakness of the narrow lines had such a dramatic impact on the RV fitting in G14 (see G14; Fig. 5) that the majority of the WHT measurements within ± 0.1 of phase 0 (i.e. the inferior conjunction of the donor star) were considered spurious and were thus eliminated from further analyses. To salvage some of the data points in this range, we can go one step further and take into account the spectrum-to-spectrum variation. For each spectrum, the expected RV of the narrow lines was calculated (using a sinusoidal model) and used as the initial fit value of RV to guide the optimizer to a reasonable optimum. The quality of individual Gaussian fits was also carefully assessed by visual inspection, especially for spectra taken near the inferior conjunction of the companion (see also Section 2.1.1).

In order to exploit the potential of our highest resolution VLT data (see, e.g., G14, Fig. 4), we modified the model for extracting UVES velocities. Instead of fixing the FWHM of all the Gaussians, we fixed the width of the underlying broad component to the value used in G14 but left the (common) width of the narrow components free to vary. This yielded a revised set of UVES RVs that are fully consistent with the values reported in G14 (within the formal errors) as well as the fitted width of the sharp N III/C III components. We found that the model with 7 free parameters fitted the UVES spectra better, and that the average statistical uncertainty of the VLT measurements was reduced to 1.1 km s^{-1} (compared to the previously reported precision of 2.2 km s^{-1}).

5.3 Determination of observables

The number of unreliable RVs that deviate significantly from the predicted values after applying the modified approach is substantially lower than previously estimated. Narrow lines from the donor are still present and can be detectable within the phase ranges −0.1 to

[1] http://deneb.astro.warwick.ac.uk/phsaap/software

+0.1 (albeit being rather weak since we are facing the un-irradiated side of the donor). The derived RVs within those ranges have noticeably larger error bars than data points at other phases but ought to be included in the RV fit (with correspondingly smaller weights). For these reasons, we refrain from screening data (as was introduced in G14 to eliminate a large fraction of spurious RVs), and choose to keep the total of 338 WHT & VLT measurements in the RV analyses of this paper to derive a revised set of Sco X-1 system parameters. The revised and refined RV datasets are provided in Appendix A.

5.3.1 Circular orbit fit

Assuming a negligible (intrinsic) eccentricity of the binary orbit ($e = 0$), the simplest model for the variation of the projected Bowen RVs is a sinusoid of the form (Eq 2.1). To fit the 4 free parameters (T_0, P_{orb}, K, and γ), we started with a least-squares method where each data point was weighted according to the associated error bar given by *mgfit* whilst giving no differentiation between separate VLT & WHT datasets. The reduced χ^2 value we obtained ($\chi^2_\nu = 11.3$ for 334 degrees of freedom) was greater than that obtained in G14 ($\chi^2_\nu = 8.5$ for 238 degrees of freedom) due to the inclusion of all the RV measurements, and much greater than unity. A high value of the χ^2-statistic can either be caused by limitation of the sine-wave model, or reflect the fact that the initial measurement uncertainties on the RVs are underestimated. The fit residuals we see are not consistent with those expected from irradiation effects (see Section 5.4). Therefore, for the purpose of parameter estimation, we considered that the measurement errors had been systematically underestimated by some fractional amount (efac).

Hence we proceeded to introduce additional 'multiplicative factors' into the sinusoidal model for adjusting errors on the RV data. To recognize that the data consists of three datasets with different spectral resolution/SNR contributions (1999 WHT, 2011 WHT and 2011 VLT; see Table 5.1), we invoked 3 multiplicative factors in total to rescale errors on individual multi-Gaussian fits per dataset. The 1999 and 2011 WHT observations (both covering 75% of the orbital cycle) were then refitted *separately* with the Bayesian Markov Chain Monte Carlo (MCMC) approach (using the PYTHON package `emcee`; Foreman-Mackey et al. 2013). In both cases, the resulting posterior distribution of the multiplicative factor was Gaussian (Figure 5.1), therefore we took the posterior mean ($efac_{1999} = 4.3$ and $efac_{2011} = 2.5$) as the best estimate of efac for the WHT datasets. It is also worth noting that the RV semi-amplitude for the 1999 data (77.6 ± 1.3 km s^{-1}; 68 per cent) is significantly higher than the 2011 K_{em} velocity (72.0 ± 1.0 km s^{-1}; 68 per cent). This finding is consistent with the discrepancy between the best-fit velocity semi-amplitude for the combined data ($K_{em} = 74.9 \pm 0.5$; G14) and the result of SC02 ($K_{em,\,1999} = 77.2 \pm 0.4$ km s^{-1}) based on the 1999 observations alone; and might be attributed to variations in the geometry of the line

emission over epoch, as discussed in G14.

To determine conservative parameter estimates, we scaled the WHT errors (up) by the efac values derived from the MCMC fit and repeated the least-squares analysis of the combined WHT and VLT data. At the final step, the VLT errors were scaled by a multiplicative factor ($\mathrm{efac_{VLT}} = 2.25$) which makes the final reduced χ^2 equal to 1.0. We also varied the initial parameter value of T_0 to obtain the smallest possible cross-term in the covariance matrix between P_{orb} and T_0 ($|V(P_{orb}, T_0)| = 3 \times 10^{-14}$). This yielded revised orbital parameters consistent (to within $\lesssim 2.6\sigma$) with those previously determined (by least-squares fitting to 242 RV measurements) in G14. Fig. 5.2 shows the improved RV curve (with the best fit sinusoid) consisting of a total of 338 measurements (cf. G14; Fig. 5).

The revised parameter estimates are summarized as follows for direct comparison with G14:

$$T_0 = 2455522.6668 \pm 0.0006 \text{ HJD(UTC)}$$
$$P_{orb} = 0.7873132 \pm 0.0000005 \text{ days}$$
$$\gamma = \text{-}113.6 \pm 0.2 \text{ km s}^{-1}$$
$$K_{em,\,RV} = 74.8 \pm 0.4 \text{ km s}^{-1}.$$

To compare our new T_0 constraint with that of G14, we added 1127 orbital cycles to give 2455522.6682 HJD (UTC), which differs from the estimate in this work by 121 seconds, within the 1σ uncertainty of G14's estimate propagated to 2010. The new T_0 measurement improves the constraint on the absolute phase of the system by a factor of two (both by being more precise and by being less correlated with P_{orb} when considering times after 2010) relative to the result of G14. On the other hand, the P_{orb} measurement is at the same precision as that in G14, but differs from that value by 2.6σ. In the next section, we perform tests to show that the new period and ephemeris constraints (derived from refined RV datasets) are indeed more accurate than previous findings.

5.3.2 Doppler tomography-based method

An alternative route towards orbital parameter estimation is provided by Doppler tomography. The technique has already been applied to the high SNR data of Sco X-1 to reconstruct maps for a range of emission lines present in the optical spectrum (see SC02; Fig. 4). The N III and C III maps in particular revealed a compact spot along the positive V_y-axis (consistent with an emission component from the irradiated donor), from which an independent estimate of K_{em} could be accurately derived through a two-dimensional Gaussian fit.

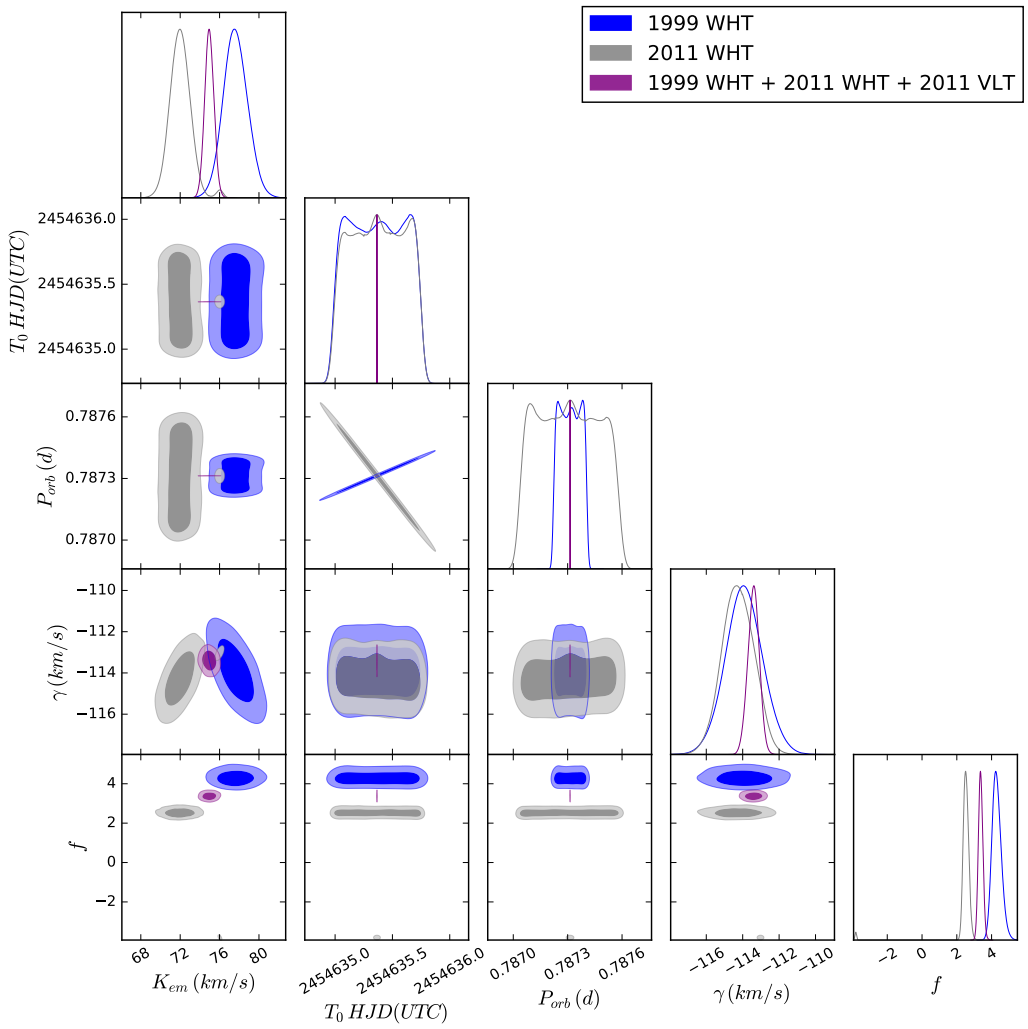

Figure 5.1: Corner plot of five parameters (including the multiplicative factor) from our MCMC analysis.

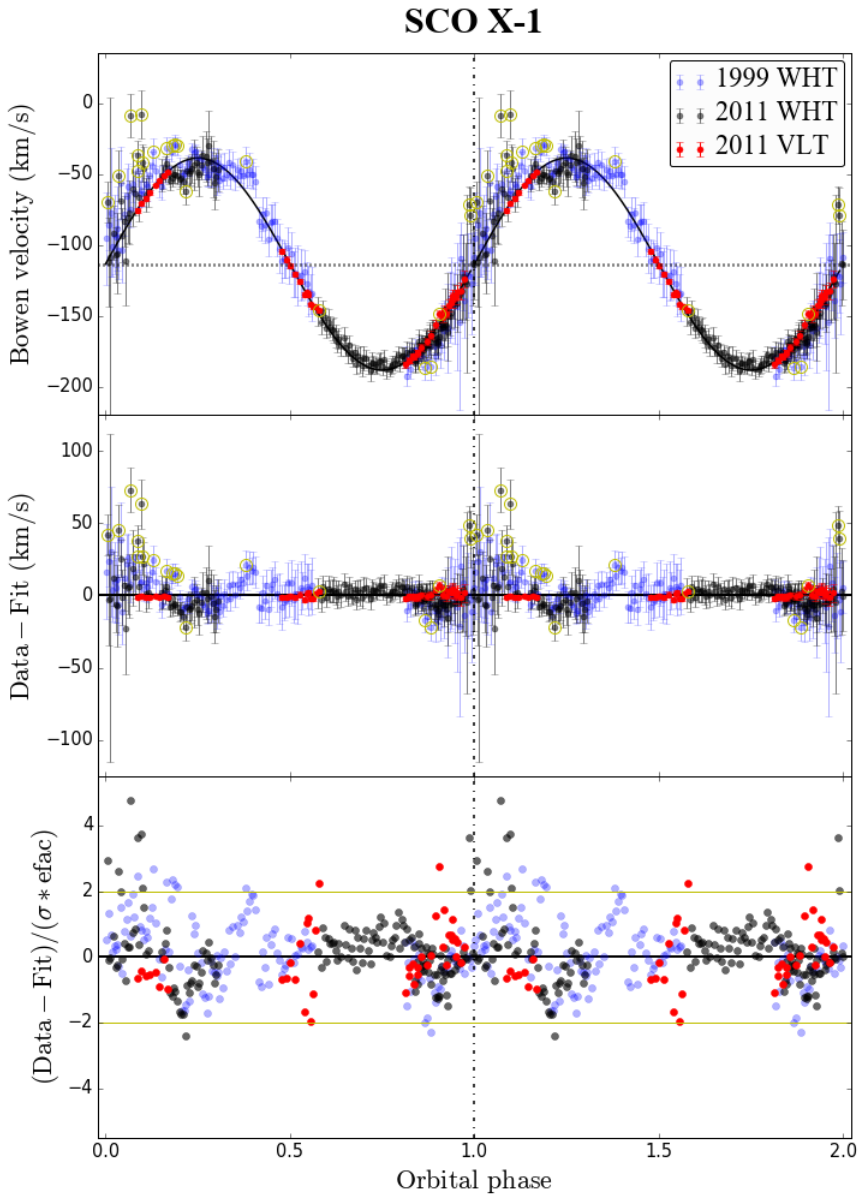

Figure 5.2: RVs of the Bowen emission components determined from the 1999 WHT (blue), 2011 WHT (black) and 2011 VLT (red) observations, with 1σ error bars after scaling by efac. The best-fitting sine wave is overplotted in black. Two cycles are shown for clarity purposes. Note that the RVs around phase zero have noticeably larger rescaled error bars (see Section 5.3.1) than data points at other phases. *Middle*: the residuals as a function of the orbital phase. *Bottom*: the residuals divided by rescaled error bars. Data points below/above the horizontal yellow line y = -2/y = 2 are identified as outliers and are marked by yellow circles in the upper and middle panels.

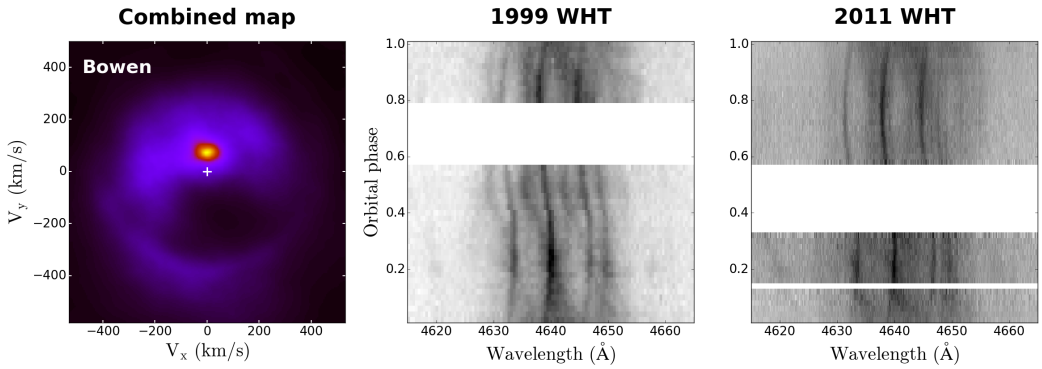

Figure 5.3: The combined Doppler tomogram of the Bowen blend (*left*) for the 1999 & 2011 WHT data (middle and right panels). The origin of the Doppler map (denoted by a white cross) corresponds to the center of mass of the system using $\gamma = -113.6$ km s^{-1}. The Bowen region is dominated by narrow 'S-wave' components produced on the irradiated face of the companion.

The Bowen map

To enable a direct comparison to be made between the K_{em} amplitude obtained from the RV fitting and the tomography-based method, we constructed new *Bowen Doppler images* (initially separately for the 1999 and 2011 WHT datasets; each covering 75% of the orbital cycle) by assigning the three strongest Bowen emission lines to the same image, and updating the input parameters to Doppler tomography (γ, T_0, and P_{orb}) with the values determined in Section 5.3.1. Both 1999 and 2011 WHT Bowen maps showed a prominent spot at the expected location of the companion, and a much fainter ring-like feature, most likely originating from the accretion disc. We note again that the centroid position of the 1999 donor emission spot is at a higher velocity ($V_x = 2$ km s^{-1} and $V_y = 76$ km s^{-1}) than that inferred from the 2011 donor spot ($K_{em,\,2011} = 72.2$ km s^{-1}). Furthermore, with the aid of the second-generation DOPPLER code[2] developed by T. Marsh (e.g., Manser et al. 2016), it is possible to construct one Bowen image for the *combined* 1999 and 2011 WHT data even though these have different spectral resolutions. The *combined map* and the phase-binned, trailed spectrograms of the Bowen region (from the WHT observations) are displayed in Fig. 5.3.

Bootstrap Doppler tomography

For robust estimation of K_{em} from the combined Bowen map we adopted the 'bootstrap Monte Carlo' approach, initially developed for statistical uncertainty derivation and, most importantly, robust significance testing for spot features in the low SNR cases (e.g. XTE

[2] https://github.com/trmrsh/trm-doppler

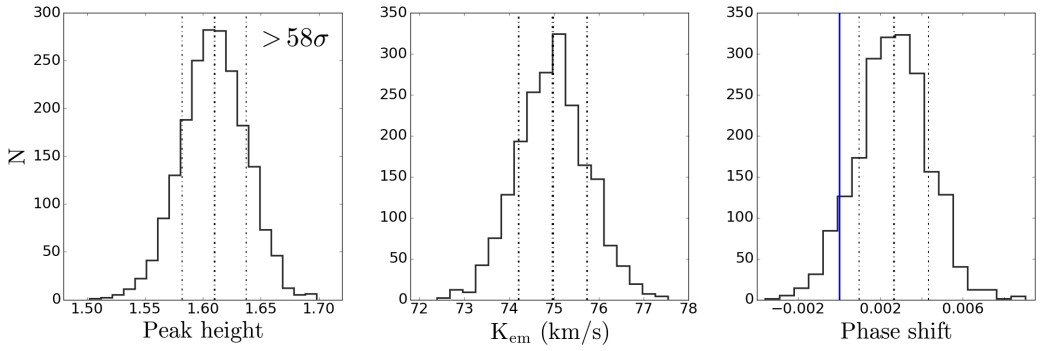

Figure 5.4: Number distributions of the peak height (left), RV semi-amplitude (middle) and phase shift (right) of the donor emission spot determined from 2000 combined, bootstrapped images. Dashed lines indicate the mean and the $\pm$ 1σ confidence intervals. The feature is significant at the >58σ level and the phase shift is consistent with zero (blue solid line) within 2σ using the orbital period, ephemeris and systemic velocity in Table 5.2.

J1814−338); but can be readily extended to the mid- to high-SNR regime. We created 2000 simulated images from 2000 independently generated bootstrapped datasets (Efron & Tibshirani, 1993) in the same manner as for the original map (see 2.2.1) using custom wrapper functions. Measurements of various spot properties (e.g., the centroid position and the peak intensity) were then performed for the ensemble of combined images.

Fig. 5.4 shows the histograms of the most relevant spot parameters as derived from the bootstrap samples. Firstly, we considered the distribution of the peak height in terms of a significance level of the (combined) donor signal. By fitting a Gaussian curve to the histogram plot in the left panel of Fig. 5.4, we deduce that the mean of the peak intensity distribution is above zero at the >58σ level. Moreover, in contrast to the results for the much lower SNR data of XTE J1814−338 (which indicated a 4σ detection of the mass donor), Fig. 5.4 (middle panel) shows that the combined Bowen image for Sco X-1 provides a tight constraint on the RV semi-amplitude, K_{em} = 75.0 $\pm$ 0.8 km s^{-1}, for an assumed value of γ = −113.6 km s^{-1}.

It is known that the choice of the input parameter γ can have an impact on the resulting reconstruction – and spot features in particular would appear out-of-focus and misplaced if an incorrect γ was used to obtain the image (e.g. Steeghs 2003a; Muñoz-Darias et al. 2009). Thus, we ran the same analysis using a range of γ values in steps of 2 km s^{-1}, centered on −113.6 km s^{-1}. Within a narrow range of γ values between −120 and −108 km s^{-1}, a >50σ donor detection was achieved, peaking near the expected value from our RV fit. The derived K_{em} velocity showed a small range of variation (with a maximum of 0.6 km s^{-1} deviation from 75 km s^{-1}; see Figure 2.15), therefore indicating the presence of a small systematic error on K_{em} due to the uncertainty in γ. We note that this constraint

on the systemic velocity ($\gamma = -114 \pm 6$ km s^{-1}) is looser compared to the best-fit value derived from the RVs (-113.6 ± 0.2 km s^{-1}) since it is not very sensitive to changes below the spectral resolution of the data. Based on the above results, we obtain

$$K_{em,\,doppler} = 75.0 \pm 0.8\ (stat) \pm 0.6\ (sys)\ km\ s^{-1},$$

in excellent agreement with the value derived from the traditional RV fitting method. Therefore the novel technique of bootstrap Monte Carlo delivers a robust and more conservative estimate of K_{em} for the combined observations, which we adopt as our best estimate of the Bowen K_{em} amplitude.

Since Doppler tomography exploits all spectra at once, the technique is also less affected by the problem of extremely weak features near phase zero (see G14; Fig. 2) compared to individual line profile fitting. This makes bootstrap Doppler tomography an attractive tool for deriving binary system parameters *across all SNRs*. The main disadvantage of the tomography-based method is that T_0 and P_{orb} are used as input, instead of being determined directly from the reconstruction. However, the phase shift ($\Delta\phi_{spot}$) between the donor spot and the vertical plane can provide a good indication of the accuracy of the input ephemeris.

With the correct ephemeris, emission from the donor should always be projected on the tomogram at the position $V_x = 0$ and $V_y = K_{em}$ (hence $\Delta\phi_{spot} = 0$), whereas phase errors tend to lead to a rotation of the image. In the right panel of Fig. 5.4 we show that $\Delta\phi_{spot}$ is consistent with zero (blue solid line) within 2σ for our best estimate of γ. A diagnostic plot of $\Delta\phi_{spot}$ as a function of the assumed γ (between -120 and -108 km s^{-1}) gives $\Delta\phi_{spot} = 0.003 \pm 0.002$ (statistical) ± 0.002 (systematic). It can thus be concluded that the donor spot is indeed centered on the positive V_y-axis using the revised binary period and ephemeris. Table 5.2 lists the final adopted values of T_0, P_{orb}, γ, K_{em} and the cross-term (needed to determine the propagated uncertainty on the future epoch of inferior conjunction; see G14).

A similar test using T_0 and P_{orb} of G14 yielded a significant (3σ) phase shift between the donor spot and the vertical plane, which indicates that the previous results included contributions from systematic errors. Since the revised period and ephemeris were derived from an improved RV curve (including all data points) using a refined analysis approach, and there is no measurable phase shift, the new estimates for orbital parameters presented in this work can be considered more reliable than the results of G14.

5.4 Estimation of binary parameters

So far we have exploited the proven Bowen emission line diagnostic that permits a robust and accurate RV study of the companion star in Sco X-1. To precisely constrain the remaining parameters for the purpose of GW searches, K_1 and e, requires a direct determination

of the neutron star orbit, which is particularly challenging due to the lack of NS pulsations. While coherent pulsations of Sco X-1 are not observed, we shall rely on the known set of parameter constraints and apply Kepler's laws to derive a more conservative K_1 estimate compared to that of SC02 obtained using broad disc emission features.

5.4.1 The K-correction

The deviation between the reprocessed light centre and the centre of mass of the Roche-lobe-filling donor ($K_{cor} = \frac{K_{em}}{K_2} < 1$) can be modelled by generating RV curves from simulated emission line profiles formed by isotropic irradiation on the illuminated hemisphere. Results of the most extensive study of K-correction modelling to date (Muñoz-Darias et al. 2005; hereafter, MCM05) suggest a weak dependence of K_{cor} on the orbital inclination (i); but a strong dependence on the mass ratio (q) and the disc opening angle (α). For Sco X-1, an estimate of the binary inclination is available from modelling of the orientation of radio lobes ($i = 44^\circ \pm 6^\circ$; Fomalont et al. 2001). However, the disc shielding parameter is unknown and therefore throughout the rest of our analysis, we consider the full range of possibilities – from the extreme case of neglecting disc shadowing ($\alpha = 0^\circ$; maximum displacement) to $\alpha = 18^\circ$ where the companion is nearly completely shadowed by the accretion disc (minimum displacement). The key ingredient for improving the K-correction then involves mainly the determination of constraints on q.

Center of symmetry search

The ring-like disc emission feature revealed using Doppler tomography (SC02 and this work) may be used to constrain the NS's projected RV (K_1). In Doppler coordinates, the projection of an ideal Keplerian disc is always centered on the expected position of the NS $(V_x, V_y) = (0, -K_1)$, as the disc gas should track the orbital motion of the accreting primary. Thus, although the accretor is rarely seen in emission, a search for the centre of symmetry (CoS) of the disc component in velocity space should, in principle, yield a valid solution for $K_1 \simeq K_{disc}$ (e.g. van Spaandonk et al. 2010; Longa-Peña et al. 2015).

For a reconstructed Doppler map, one first subtracts a symmetric component around an assumed centre ($V_x = 0$, $V_y = -K_{disc}$), followed by inspecting the resulting residual image for any remaining asymmetries not related to the primary, e.g., emission caused by the stream/disc impact. The process is then repeated for a wide range of K_{disc} values to select an optimal center that minimizes the residuals over a region of the map containing clean disc emission. Since non-disc components and hot spot contamination can be easily masked during the minimization, the method has the advantage of allowing one to remove the distortions by any asymmetries which would normally disrupt the outer disc, and focus on the

higher velocity emission arising from the (undisturbed) inner part of the disc (appearing further away from the origin in velocity space).

Under the assumption that the disc is axisymmetric around the NS primary, the technique was adopted in SC02 to obtain an initial K_1 estimate for Sco X-1 based on the location of the CoS for the Hβ image ($K_{\mathrm{disc,\,H}\beta}$ = 40 km s^{-1}). Here we focus on applying the method to the newly computed Bowen image – which reveals the best defined accretion disc among the maps reconstructed from principal spectral features (see, e.g., SC02; Fig. 4) – in order to assess the stability and the validity of the CoS measurement.

We cycled the assumed V_y-coordinate of the disc centre between −200 and +20 km s^{-1} in steps of 2 km s^{-1} (while keeping V_x fixed to 0) and measured the mean residuals in the lower half of the reconstruction (to exclude the region near the secondary emission). For the 1999 Bowen data the residuals showed a minimum at $V_y = -K_{\mathrm{disc}} = -84$ km s^{-1} (Figure 5.5). A similar result was obtained also for the 2011 Bowen image (K_{disc} = 90 km s^{-1}), suggesting that a significantly higher value of K_1 amplitude than previously estimated (using the same method but a different line feature) needs to be considered. Given the absence of a sharp disc ring in the 1999 Hβ map, compounded by the presence of enhanced emission in the bottom left quadrant, it is most likely that the best fit $K_{\mathrm{disc,\,H}\beta}$ value still failed to represent the NS's true projected RV. These significant differences between different lines show that extracting robust K_1 constraints from disk lines remains challenging. Hence we decided to adopt the greatest value for K_{disc} based on CoS measurements using maps of a range of emission lines as our most conservative maximum value of K_1. Using a new upper limit on

$$K_1 \simeq K_{\mathrm{disc,\,Bowen}} \leqslant 90 \text{ km s}^{-1},$$

and apply the K-correction (for $\alpha = 18°$) to K_{em}, we obtain an upper limit of $q \leq 0.76$.

Rotational line broadening

If we assume that the Bowen emission comes from the irradiated front face of the mass donor (as discussed in SC02 and Section 5.3) and the rotation to be the dominant line broadening mechanism, the observed width of the sharp N III/C III lines ($V_{\mathrm{rot}} \sin i_{\mathrm{em}}$) to K_2 can be used to set a strict lower limit on q. For a spectral feature that is produced throughout the Roche lobe, the expected width ($V_{\mathrm{rot}} \sin i$) is given by equation (1.18) (Wade & Horne, 1988). Since the donor is not fully illuminated, this becomes a limit as $V_{\mathrm{rot}} \sin i > V_{\mathrm{rot}} \sin i_{\mathrm{em}}$. By taking the weighted average of the set of 12 FWHM (N III/C III) values measured from the VLT spectra (see Section 5.2) near orbital phase 0.5 when the visibility of the irradiated face is maximum, we obtain an estimate for the width of the narrow components of FWHM = 51.9 ± 0.5 km s^{-1}. However, it should be cautioned that this preliminary

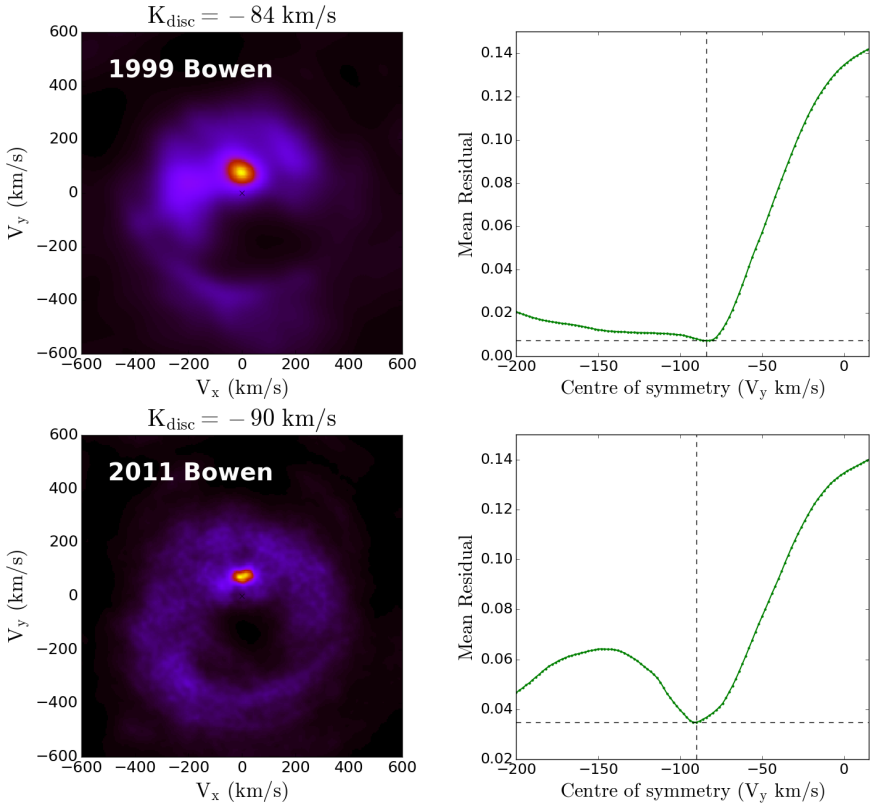

Figure 5.5: **Left:** the original Doppler tomogram of the Bowen blend for Sco X-1 for the 1999 & 2011 WHT data. **Right:** residual level calculated as a function of the assumed V_y-coordinate of the disc centre. A minimum residual is found for $V_y = -84$ km s^{-1} (dashed line; top right) for the 1999 Bowen image, and $V_y = -90$ km s^{-1} (dashed line; bottom right) for the 2011 image.

estimate does not provide a strict lower limit to V_{rot} sin$i$ as the measured widths include also the intrinsic broadening effect due to our instrumental resolution (8 km s^{-1}).

Following Casares et al. (2006), we corrected for the instrumental effect by broadening a Gaussian template of FWHM = 8 km s^{-1} using a Gray rotational profile (Gray, 1992) without limb-darkening (because fluorescence lines arise in optically thin conditions); and subsequently determined for each of the 12 VLT measurements the amount of rotational broadening required to reproduce the apparent FWHM (N III/C III). This leads to a weighted average of V_{rot} sini_{em} = 37.8 ± 0.4 km s^{-1}, which combined with the K-correction for α = 0°, gives a lower limit of $q \geq 0.22$. Since it has been shown in SC02 and Section 5.3 that the reprocessed light center traces the orbit of the companion, and emission lines arise not from the entire Roche lobe but the irradiated part only, we are confident that the observed width of the narrow lines provides a valid lower bound to true V_{rot} sin$i$, and hence a secure lower limit of q (by ruling out very small rotational broadening).

The lower limit of q can be further improved by applying a correction factor (defined as $V\sin i_{cor} = \frac{V\sin i_{em}}{V\sin i} < 1$) to convert the observed rotational broadening to true $V\sin i$, for the reasons mentioned above. In light of the results of the MCM05 study of K_{cor}, we estimate this correction factor $V\sin i_{cor}$ in the low inclination case (i = 40°) – suitable to be applied to the case of Sco X-1 – by following the same approach for modelling the K-correction described in MCM05. The details of the modelling are described in Appendix B. The solution for $V\sin i_{cor}$ at α = 0° represents the most conservative correction (see Appendix B), which can be safely adopted to yield an improved lower limit of q (at a value slightly higher than 0.22), and thereby also providing the best lower limit to K_1 (see Section 5.4.2).

5.4.2 Monte-Carlo analysis

Armed with the complete set of K-correction models solved by MCM05 and new limits on K_1 and the rotational broadening (see Section 5.4.1), we perform Monte Carlo simulations for deriving the probability density functions of Sco X-1 system parameters. Of particular note is the K_1 distribution (or $a_x \sin i = K_1 P_{orb}/(2\pi)$) required by most directed searches for continuous GWs.

As an initial, conservative estimate, we used the binary inclination inferred from the orientation of radio jets and results from the reanalysis of the combined Bowen data (Section 5.3) only. Synthetic values of P_{orb}, K_{em} and i were selected from a Gauss-normal distribution (with the mean and standard deviation equal to the values listed in Table 5.2). To perform the K-correction, we started with the most conservative scenario by simulating uniformly-distributed values of α and q over the entire ranges considered by MCM05 (covering values typical of XRBs) between $\alpha \sim 0°$ and 18°; $q \sim 0.05$ and 0.83. For each pair of randomly generated disc opening angle and mass ratio, we determined a precise value

of K_{cor} by interpolating over the grid of MCM05 models. After applying K_{cor} to K_{em}, we obtained the corresponding K_2 amplitude, which was then used (along with P_{orb}, i and q) as the input to the mass function equation (Eq 1.17) for deriving the mass of the compact primary M_1. At the end of each trial, the RV of the primary $K_1 = qK_2$ and the mass of the donor M_2 were also calculated; and the process was repeated 10^6 times. Assuming a NS accretor, only the outcomes of trials that yielded an M_1 value between the minimum (~ 0.9 $M_\odot$; e.g., Lattimer 2012) and the maximum stable NS mass (3.2 $M_\odot$) were assembled into the initial, conservative estimate of the PDF's (Figs 5.6 and 5.7; grey).

Radial velocity of the NS

As a next step we imposed an upper limit on K_1 determined from center of symmetry analyses of the disc component ($K_1 \lesssim 90$ km s^{-1}), which essentially sets a more realistic upper limit of q as discussed in Section 5.4.1. For each Monte Carlo trial, we additionally computed the minimum allowable $V\sin i$ value by applying the most conservative $V\sin i$-correction (derived in Appendix B). This is the case of $\alpha = 0°$, dependent only on q, and considering the lower limit on $V\sin i > 36.6$ km s^{-1} (99.7 per cent confidence) as estimated from the width of the sharp N III/C III lines. A conservative and stringent lower limit of q could therefore be established using the relationship between $V\sin i$ and q (equation 1.18). Finally, the output PDF's that reflect our current best knowledge of Sco X-1 parameters are shown in Figs 5.6 and 5.7 (green), with those derived only from the observed distributions of P_{orb} and K_{em}.

Because of these newly imposed constraints, the CIs for nearly all system parameters (except M_1) are narrowed down significantly. In particular, *the estimate of the centre of the disc component had such a strong impact that the upper K_1 limit was reduced from 165 to 90 km* s^{-1}*; and thus represents the most valuable determination in the context of refining the parameter space for GW searches*. Ruling out high values of K_1 (or $a_x \sin i$) has a double benefit, since high values of $a_x \sin i$ increase the required resolution in orbital phase (T_0). We also note that the new $V_{rot} \sin i$ constraint (combined with a minimum $V\sin i$-correction) provides a refined lower limit not only for q but also for both K_1 and K_2, due to the dependence of K_{cor} on q. This yielded the current best hard limits on K_1 of 40–90 km s^{-1}, or equivalently,

$$1.45 \text{ light-second} \leq a_x \sin i \leq 3.25 \text{ light-second}.$$

This range of K_1 is significantly broader than the previous constraint (40 ± 5 km s^{-1}) derived solely from centre of symmetry measurements from the Hβ Doppler map (SC02). In the recent search for continuous gravitational-waves from Sco X-1 (e.g., Abbott et al. 2017c),

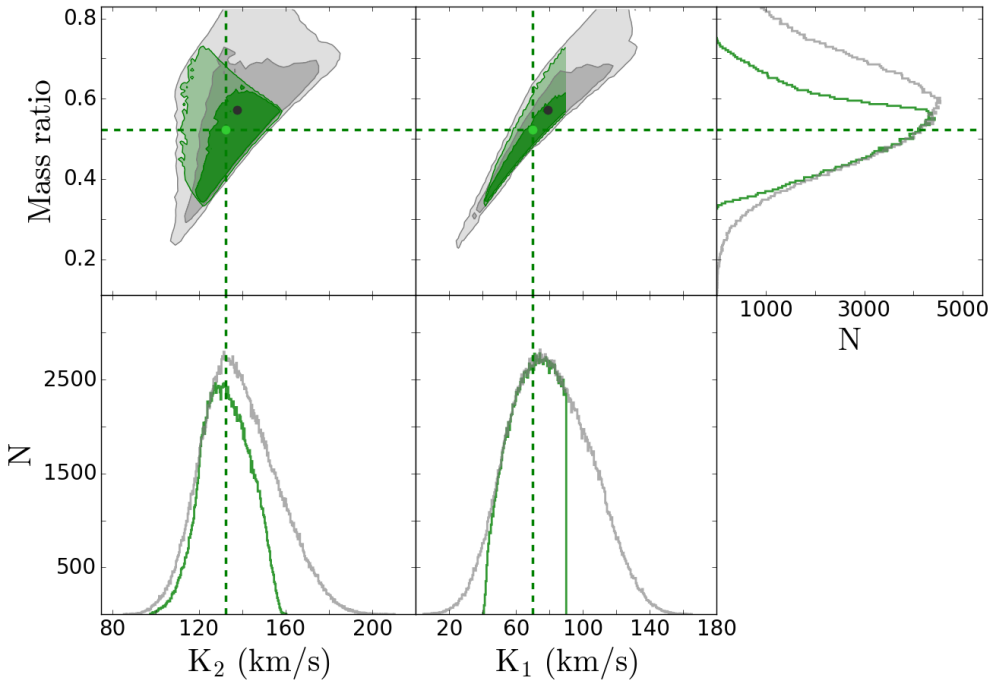

Figure 5.6: The 68 per cent and 95 per cent confidence regions and projected PDF's for K_1, K_2 and q derived from the Monte Carlo binary parameter calculations (10^6 trials). Our best estimates for the PDF's (after applying the newly derived K_1 and $V\sin i$ constraints; see Section 5.4.1) are shown in green, compared to the results of the most conservative possible scenario (grey). Dashed lines indicate the locations of the 50$^{\text{th}}$ percentile (median). The best estimates for the system parameters and their associated 95 per cent confidence intervals (CI) error bars are given in Table 5.2.

the range for the projected semi-major axis has been expanded in order to cover the full parameter space.

Determination of the component masses

Despite the fact that the RV semi-amplitude of the Bowen emission can be measured with a precision of ~1 per cent, the true projected RV of the donor is not well constrained (K_2 = 132^{+20}_{-21} km s^{-1}; 95 per cent confidence) given the lack of knowledge of q and the disc shielding parameter. Using a geometric model for the reprocessing of X-rays in LMXBs, an average disc opening angle of ~12° has been proposed for other persistent sources, e.g., GR Mus and V4134 Sgr (de Jong et al., 1996). Similarly, for Sco X-1, an α-value at the lowest end of the range between 0° and 18° is perhaps unlikely (given also the clear presence of an accretion disc). However, we chose not to adopt any ad hoc α estimates in the Monte Carlo analyses, which could introduce potential biases into the resulting PDF's.

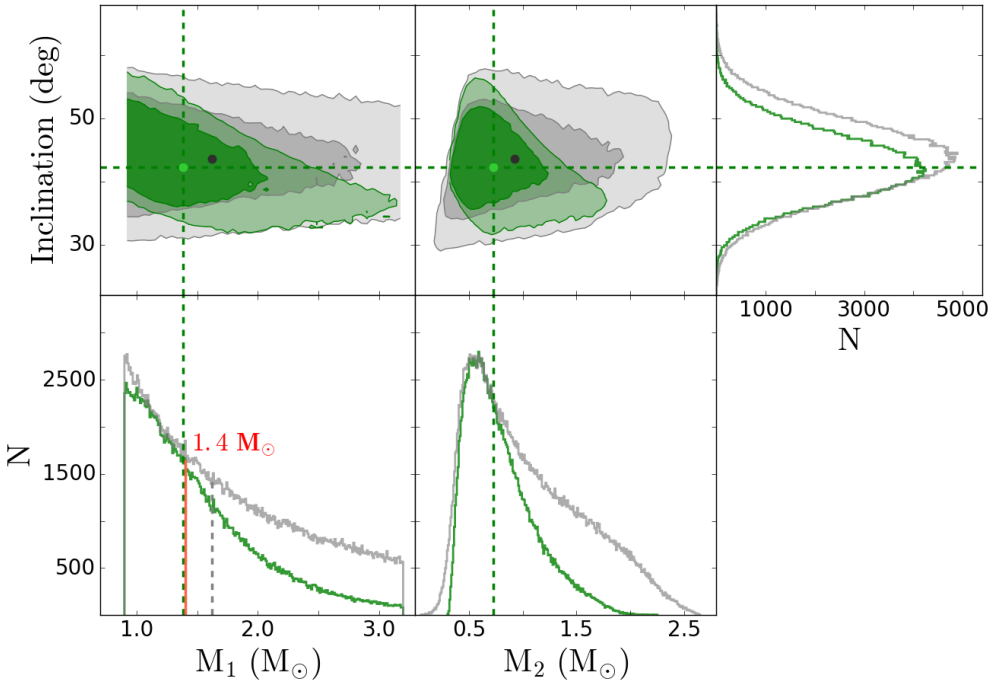

Figure 5.7: The 68 per cent and 95 per cent confidence regions and projected PDF's for M_1 and M_2 using the inclination estimate by Fomalont et al. (2001). Dashed lines indicate the locations of the 50th percentile (median). Note that including the observational constraints on K_1 and $V\sin i$ in the Monte Carlo analysis shifts the median exactly to the canonical NS mass of 1.4 $M_\odot$ (red solid line).

Table 5.2: Sco X-1 system parameters. Note that the $a_x \sin i$ constraints represent hard limits on the projected semi-major axis of the NS.

Parameter	Value
P_{orb} (d)	0.7873132(5)
T_0 HJD(UTC)	2455522.6668(6)
T_0 (GPS seconds)	974433600 ± 50
$\lvert V(P_{orb}, T_0)\rvert$ (d^2)	3×10^{-14}
γ (km s^{-1})	-113.6 ± 0.2
K_{em} (km s^{-1})	75.0 ± 0.8 (statistical) ± 0.6 (systematic)
K_1(km s^{-1})	70^{+19}_{-25} (95%)
$a_x \sin i$ (ls)	$[1.45, 3.25]^a$
K_2 (km s^{-1})	132^{+20}_{-21} (95%)
q (M_2/M_1)	$0.52^{+0.16}_{-0.15}$ (95%)
i (°)^b	44 ± 6
M_1 ($M_\odot$)	$1.4^{+1.4}_{-0.5}$ (95%)
M_2 ($M_\odot$)	$0.7^{+0.8}_{-0.3}$ (95%)

Notes.
[a]The range for the projected semi-major axis of the NS $a_x \sin i = K_1 P_{orb}/(2\pi)$ in light-seconds;
[b]Adapted from (Fomalont et al., 2001).

Due to the large uncertainties in the final values of K_2 (dominated by the unknown K-correction) and q ($0.52^{+0.16}_{-0.15}$; 95 per cent), it remains difficult to put strong constraints on the component masses. Using the inclination value of 44° ± 6° – inferred from the orientation of radio jets (assuming that the radio jet is perpendicular to the orbital plane) – we obtain a 95 per cent credible range of the NS mass between 0.9–2.8 $M_\odot$ and an M_2 range of 0.4–1.5 $M_\odot$ (95 per cent). Interestingly though, the median of our best estimate for the M_1 PDF (after applying the K_1 and $V \sin i$ constraints) coincides with the 'canonical' value of 1.4 $M_\odot$ – in support of the presence of a ∼ 1.4 $M_\odot$ neutron star.

The complete set of dynamical system parameter constraints, derived from the latest RV measurements as well as Monte-Carlo simulations, are provided in Table 5.2.

5.4.3 The eccentricity problem

One complication of the Bowen technique is that the established RV curve is not expected to be perfectly sinusoidal owing to the effect of non-uniform flux distribution at the surface of the irradiated donor star. This is a particular handicap for attempts to constrain any true orbital eccentricity, e, of the binary.

The influence of irradiation effects can be clearly seen in Fig. 5.8, where we display the simulated residual RV curves obtained by subtracting the sinusoidal fit from the irradiation model (described in Appendix B) for the most probable mass ratio of Sco X-1 ($q \simeq 0.5$; as calculated by the Monte Carlo method) and different α-values. As noted in the appendix and in previous studies, the amount of deviation of the simulated RVs from a sinusoidal wave form increases with decreasing disc opening angle (see also MCM05; Fig. 2). Closer inspections reveal that for all α values the deviations increase at small and large orbital phases ($\lesssim 0.2$ and $\gtrsim 0.8$), consistent with the distortions as seen, for example, in the observed RV curves of the pre-cataclysmic binary NN Ser (see Parsons et al. 2010; Fig. 8). Based on results from both observations and simulations, we conclude that RV distortions caused by irradiation effects would dominate those produced by any small intrinsic e of the binary orbit. Although they are not described by an eccentric model, attempting to fit such RV curves with an eccentric orbit would inevitably produce an *apparent eccentricity* (aE), which varies strongly with disc opening angle[3].

Worse still, Fig. 5.8 also shows that the WHT data do not yet offer the RV precision high enough for differentiating between the irradiation and the circular orbit model. Not even the 2011 UVES/VLT data has the precision high enough to firmly differentiate between residual RVs for low and high α angles, thus making it currently infeasible to accurately infer the value of the disc opening angle necessary to clearly disentangle aE from any true orbital eccentricity.

Due to the inherent limitations of the method, as well as limitations of the current data sets, in this paper we only attempt to place a crude upper bound on e by running an MCMC analysis (to fit the combined RV data) and assuming an elliptical orbit model. By leaving the spurious eccentricity (E) and periastron angle as free parameters, we obtained a 95 per cent credible range of the eccentricity parameter E between 0.00086-0.082 (using a Jeffreys prior on E); and $E < 0.097$ (95 per cent) with a uniform prior (Figure 5.9). However, we stress that the nominal upper bound of 0.082 or 0.097, determined *without* taking account of any irradiation effects (note that $a\mathrm{E}/e \gg 1$), cannot accurately represent the limit to the true orbital e, which is expected to be much closer to zero for a Roche-lobe overflow XRB with a high mass-accretion rate (e.g., Sco X-1).

5.5 Conclusions

In light of our new constraints on orbital parameters, the ranges of search parameters T_0 and $\mathrm{P_{orb}}$ should be updated with the refined period and ephemeris. More importantly, the

[3]As we mentioned in the appendix, the amount of deviation of RVs from a pure sinusoid increases with increasing mass ratio, therefore aE varies also with q.

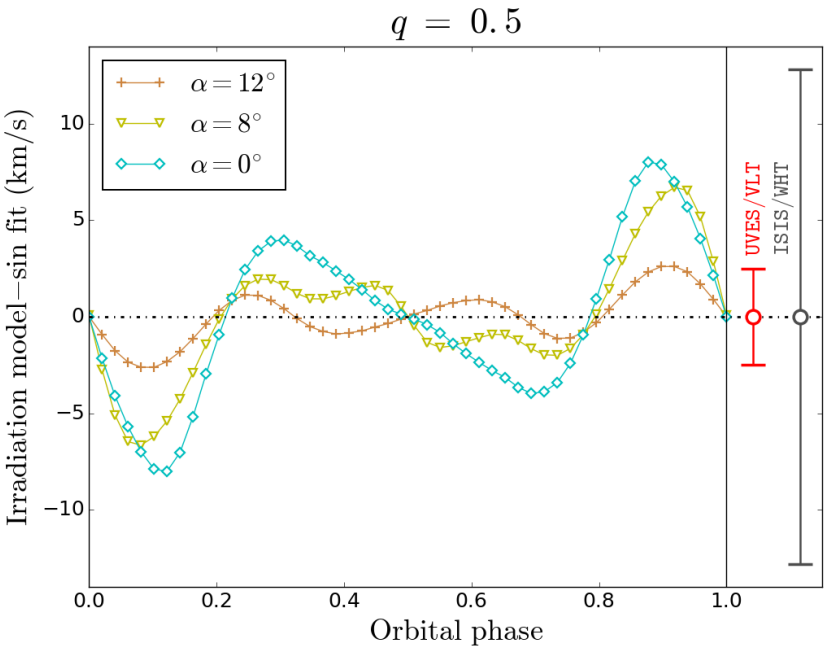

Figure 5.8: Plot of simulated residual RVs obtained by subtracting the sinusoidal fit from the irradiation model (computed in the appendix) for a probable mass ratio of Sco X-1 ($q = 0.5$) and three different disk flaring angles. The grey and red error bars represent respectively the average (rescaled) RV uncertainties for the WHT and UVES/VLT measurements. Neither WHT nor the highest resolution UVES/VLT data could offer a high enough RV precision to firmly differentiate between residual RVs for low and high α values, which makes it infeasible to clearly disentangle any spurious eccentricity produced by irradiation effects from the true orbital eccentricity (in the case of Sco X-1).

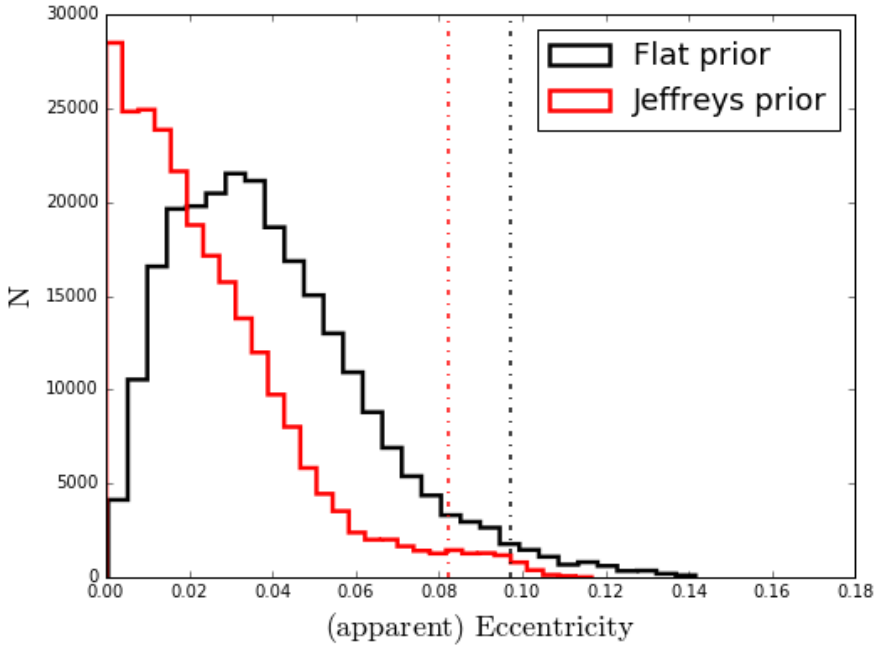

Figure 5.9: Posterior PDFs for the apparent eccentricity derived from combined RV data of Sco X-1. Dash-dot lines denote the upper bounds of the 95% confidence intervals.

range for the projected semi-major axis $a_x \sin i$ needs to be expanded and updated with the new confidence interval for K_1, which reflects a systematic uncertainty much greater in magnitude than the statistical error estimated in SC02. With the previous values (which spanned an unrealistically narrow range), there was a high probability of missing the GW signal. In the first Advanced LIGO observing run (O1) searches, a preliminary constraint of 10 km $s^{-1} \leq K_1 \leq 90$ km s^{-1} (available at the time the search was constructed) was adopted as the prior assumption. The best marginalized 95% upper limit on the signal amplitude (obtained by Abbott et al. 2017c) reaches 2.3×10^{-25}, which is a factor of ~ 7 stronger than the best upper limits set using data from initial LIGO science runs. In future runs, computing resources will be concentrated on the final refined range of 40 km $s^{-1} \leq K_1 \leq$ 90 km s^{-1}, making the search cheaper than in the O1 search, which allows a more sensitive search at the same computing cost.

Chapter 6

Conclusions and future work

Accurate mass determination of NSs and BHs have many important implications in astrophysics. NSs and BHs in compact binaries can be easily detected through accretion. Thus X-ray binary systems offer the best way to measure the mass of the accreting compact objects. Classical dynamical studies of LMXBs rely on the spectroscopic detection of the companion star at optical and/or near-infrared wavelengths. For systems in active states, the optical emission is dominated by the reprocessing of hard X-rays in the outer accretion disc, which severely hampers the detection of the much fainter companion. The so-called Bowen technique was developed to measure the orbital motion of the donor star using narrow emission lines arising from the X-ray illuminated atmosphere of the donor (first discovered in Sco X-1; Steeghs & Casares 2002).

Since the first detection of the donor star in Sco X-1, it has been shown for several other suitably bright persistent systems that the use of Bowen emission lines as tracers of counterpart radial velocities provides a unique opportunity to constrain their mass functions (Cornelisse et al., 2008). One of the main difficulties in applying the Bowen technique to persistent LMXBs and/or transients during outburst lies in the fact that in most cases the narrow emission lines are too faint to be detectable in individual spectra. The aim of this thesis is to further develop our methodology and apply the new, versatile set of analysis tools to different objects to obtain robust binary parameter constraints.

6.1 Summary of the method

To cope with weak emission features, the Doppler tomography technique is used to exploit all phase-resolved spectra at once to reconstruct the emission distribution of the Bowen region in velocity space. For most of the Bowen targets (SNR < 10), Doppler tomography provides the only way to detect emission from the donor, which should always be

mapped onto a compact spot along $V_x = 0$ km s^{-1} on the positive V_y-axis in the reconstructed Doppler image. Caveats are needed in the cases of the lowest SNRs, where the authenticity of a possible donor detection is of most concern. Furthermore, for all objects a robust estimate for the uncertainty of the measured RV semi-amplitude K_{em} is needed in order to derive the most robust limits on component masses. Thanks to the vast increases in computational power, these problems can now be tackled by introducing a Monte-Carlo style bootstrapping test.

By constructing a few thousand bootstrapped Doppler images, we first obtain histograms of various properties, e.g., the peak height and centroid of sharp emission features. Extensive testing on available datasets of LMXBs spanning a range of SNRs (Chapter 3) showed that these histograms can be well described by a Gaussian distribution. If the reality/significance of a possible companion feature can be confirmed (using, e.g., the peak height distribution), we then proceed to determine the best estimates for K_{em} as well as its 1σ statistical uncertainty. It has been noted in previous studies (e.g. Casares et al. 2006) that K_{em} can be weakly dependent on the assumed systemic velocity. We therefore consider the reconstructions using a reasonable range of γ values, and plot the significance and K_{em} velocity of the associated spot feature as functions of the assumed γ. In principle, one can expect that the best value of γ (the one that is the closest to the true value) would yield the maximum significance of secondary detection. From such a diagnostic diagram, we can evaluate the optimal solution and any systematic uncertainties of the derived K_{em}.

To this date, the detection of Bowen emission from the irradiated donor is the only opportunity for constraining dynamical masses of persistent LMXBs via the mass function (Eq 1.17). For all systems, we performed a Monte-Carlo analysis, combined with an advanced K-correction tool (to transform K_{em} to K_2; see Section 2.2.3), to establish the probability density functions of the unknown system parameters. The strategy described above can be easily extended to cataclysmic variable (CV) systems, where a different emission line diagnostic is used (e.g. Ca II; van Spaandonk et al. 2010). We remark that the method can also be used to characterize other features in Doppler maps, e.g., the accretion disc and spiral arms.

A schematic summarizing the steps of Bowen data analysis is given in Figure 3.2. The main results of the application of the newly developed method to a total of 7 systems (including 2 transients) are summarized in Table 6.1 ranked in decreasing order of optical brightness.

Table 6.1: A list of observed optically bright, active low-mass X-ray binaries with updated system parameters.

System	Type	Mag	P_{orb} (hr)	Significance	K_{em} (km/s)	M_1 ($M_\odot$)	Reference
Sco X-1	Persistent	B=12.2	18.9	$> 58\sigma$	75.0 ± 0.8 (statistical) ± 0.6 (systematic)	$1.4^{+1.4}_{-0.5}$ (95%)	[1]
X1822-371	Persistent	B=15.8	5.6	18σ	278 ± 2		[1]
V926 Sco	Persistent	B=17.9	4.7	$> 5\sigma$	200 ± 10 (statistical) ± 10 (systematic)	$2.2^{+0.9}_{-1.3}$ (95%)	[1]
V801 Ara	Persistent	B=18.2	3.8	$> 5\sigma$	251 ± 14	$1.9^{+1.2}_{-0.8}$ (95%)	[1]
GR Mus	Persistent	B=19.1	3.9	$> 4\sigma$	255 ± 19	$1.8^{+1.3}_{-0.9}$ (95%)	[1]
GX 339–4[a]	Transient	V~16–21[b]	42.1	–	–	2.3 – 9.5	[2]
Aql X-1	Transient	V~17–22[b]	18.9	$\gtrsim 13\sigma$	102 ± 6	1.2 – 3	[1], [3], [4]
XTE J1814−338	Transient/AMXP	V~17–23.3[b]	4.2	$> 4\sigma$	315 ± 28 (statistical) ± 8 (systematic)	$2.0^{+0.7}_{-0.5}$	[1], [5]

References.
(1) This thesis
(2) Heida et al. (2017)
(3) Mata Sánchez et al. (2017)
(4) Jiménez-Ibarra et al. (2017)
(5) Wang et al. (2017)

Notes.
[a]NIR spectroscopy of GX 339-4 taken during quiescence (May–September 2016) revealed absorption lines from the donor star. The 1.76 d orbital period was confirmed and the projected RV of the donor was measured to be lower than the K_{em} value reported in Hynes et al. (2003). The discrepancy between the previously reported K_{em} value and the new K_2 solution ruled out the donor star origin of the Bowen emission and further illustrates that in the case of transients, the Bowen blend may not always be dominated by the donor. See Section 3.3 and Chapter 6.
[b] The range between the quiescent magnitude and the peak outburst magnitude in the V-band.

6.2 Persistent systems

Our tests have confirmed the significance of previously detected donor signals ($\geq 4\sigma$) in all cases of low SNRs. Since we used essentially the same diagnostic features identified in previous works, our new estimates for the observed RV semi-amplitude are consistent with published results (see Table 1.1) but with new bootstrap estimates of statistical errors (and, in some cases, systematic uncertainties).

The method can be readily extended to the mid- to high-SNR regime to extract uncertainties of K_{em}, which has not been tackled in any previously published analyses. As can be seen from Table 6.1, the statistical significance of the detected features decreases as the B magnitude increases, and the (statistical) errors increase with decreasing significance. In contrast to the results for the low SNR data of GR Mus (K_{em} = 255 ± 19 km s^{-1}), the combined dataset for Sco X-1 provides a much tighter constraint on the RV semi-amplitude (K_{em} = 75.0 ± 0.8 ± 0.6 km s^{-1}). Hence, the new method behaves as expected. It can also be concluded that the precision of the observable K_{em} is only limited by the SNR of the dataset. In the highest SNR case of Sco X-1, a 1 km s^{-1} level precision (less than 2 per cent) can be achieved.

Despite a precise determination of the apparent RV K_{em} ($< K_2$) of the donor of Sco X-1, a determination of the mass ratio ($= K_1/K_2$) is challenging due to the lack of knowledge of K_1. This is a common problem in all other methods for obtaining dynamical system parameter constraints for LMXBs. Thanks to the availability of an inclination constraint from observations of the radio jets, we can solve for the component masses of Sco X-1 by including the full propagation of parameter uncertainties. Assuming no *a priori* knowledge of the disc flaring angle, a firm upper confidence limit on the mass of the neutron star ($M_1 <$ 2.8 $M_\odot$; 95%) was obtained. Similarly, in most other cases the major source of uncertainty that affects the final mass determination is linked to the measurements of K_1 and/or the system inclination angle (but not K_{em}). Nevertheless, our method is versatile, and any new findings, such as a robust K_1 estimate from burst oscillations (e.g. in the case of V801 Ara), can be easily incorporated into our Monte Carlo binary parameter calculations as they become available.

So far, the ADC source X1822−371 is the best candidate on which to apply the method, since both the binary inclination and the RV of the NS are precisely known. Armed with a new, robust determination of K_{em} (this thesis), all that remains to be measured for getting the most accurate mass constraints is the disc opening angle. A complete determination of the system parameters, as well as discussions on the evolution of this system, will be presented in a future paper (Muñoz-Darias et al.; in prep.).

6.3 Transients

XTE J1814−338

The new method was also applied to the 5^{th} accreting millisecond X-ray pulsar J1814. Although the weak donor signal (4σ) yielded the largest uncertainties of K_{em} among all the objects presented in this thesis, in this case we have the significant advantage of knowing K_1 very accurately (47.848 ± 0.001 km s^{-1}). As a result, both the estimates of true K_2 and the binary mass ratio can be robustly derived with 1σ errors of less than 10%. Using a random distribution of inclination angles, the dynamical constraints on component masses finally provided firm evidence for an M-type main-sequence companion ($M_2 \sim 0.2\ M_\odot$) that has been significantly bloated due to irradiation by the compact object. Our findings, combined with results from studies of the quiescent optical counterpart of J1814, suggest the presence of a rotation-powered millisecond pulsar in this 'redback' like system during quiescence. The successful detection of the donor of J1814 (in outburst) demonstrates the power of the Bowen technique for systems that are otherwise too faint to pursue using RV studies while in the quiescent state.

Aql X-1

In the case of Aql X-1 where the true RV of the donor is obtained from NIR spectroscopy in quiescence ($K_2 = 136 \pm 4$ km s^{-1}), an independent determination of K_{em} (with additional modelling) would allow us to place solid constraints on the vertical structure of the accretion disc for the first time. We analysed 65 optical spectra taken during the outburst (in 2011, 2013 and 2016), and covering a complete orbital cycle. By using Doppler tomography of N III 4640.64/4641.84, we unambiguously detected Bowen emission from the donor with a velocity amplitude ($K_{em} = 102 \pm 6$ km s^{-1}) fully compatible with the true RV amplitude. Given that K_{em}, K_2 and also q are constrained, we carried out a Monte Carlo analysis to determine the range of the disc flaring angle compatible with the observables (an inversion procedure developed earlier). Our result ($\alpha = 15.5^{+2.5}_{-5}$ deg) is consistent with an irradiation driven thick accretion disc.

It is worth noting that the upper limit to α is roughly consistent with the maximum disc opening angle for the donor to be irradiated at all. If the opening angle is indeed close to this limit, any small changes in the vertical structure of the disc (due to variable X-ray irradiation) might, at some outburst stages, increase it further and prevent the donor from being irradiated. This might explain the complex and very variable evolution of the Aql X-1 Bowen blend components, as is demonstrated by our complementary RV analysis including also the 2004 outburst data (see Figure 3.21). The reanalysis of the 2004 dataset (with a limited phase coverage), in particular, revealed no evidence of the donor signature

(although those spectra showed somewhat narrow peaks), suggesting that the Bowen lines must be emitted in a different location in the system at that time, possibly some localized regions of the disc. Hence, one should be careful when applying the technique to transients, especially for datasets with uneven phase coverage, as the Bowen blend may not always be dominated by the donor.

GX 339−4 (BH XRB)

In a study of the only BH candidate in the Bowen survey, GX 339−4, during the 2002 outburst, Hynes et al. (2003) found dynamical evidence for a BH using Bowen emission lines modulated on a period of 1.7557 days. The best fit RV amplitude (317 ± 10 km s^{-1}) implied a mass function of $f(M) = 5.8 \pm 0.5\ M_{\odot}$, which is surprisingly large given that the binary inclination is believed to be low (Wu et al., 2001).

A recent spectroscopic study of GX 339−4 during a quiescent phase (Heida et al., 2017) confirmed the orbital period of Hynes et al. (2003). However, the best-fit projected RV using absorption lines from the photosphere of the donor (K_2 = 219 ± 3 km s^{-1}) was significantly lower than the previously reported K_{em} value derived from emission components present only in part of the orbit (see Figure 3 of Hynes et al. 2003). The discrepancy between K_{em} and the new K_2 solution ruled out the donor star origin of the Bowen emission, and further illustrates that other components might contribute to the Bowen lines at various outburst stages. Thus, **in the cases of transients, a complete phase coverage is needed to ensure the extracted RV curve is valid**. From the updated set of system parameters, the mass of the accretor was constrained between 2.3–9.5 $M_{\odot}$ (95%). Without the binary inclination, a massive NS primary is not ruled out. A low inclination, on the other hand, would allow for a BH more massive than 5 $M_{\odot}$ (beyond the 'mass-gap' of 2–5$M_{\odot}$).

6.4 Future work

Sco X-1 is the most important Bowen blend system for benchmarking our method as well as CW searches, and thus remains a target for pursuing further observations. Figure 6.1 shows that without any additional data, our current ephemeris will continue to degrade. Obviously, the more epochs of data that can be secured over several observing periods, the bigger the gain. In the future, we will combine RV measurements provided by our ongoing campaign of UVES/VLT observations (93 epochs observed; 65 to come) with the 1999 and 2011 measurements to further refine the binary period and ephemeris, and ensure a good ephemeris is available throughout the Advanced-LIGO era.

Superior RV precision derived from future UVES data may also allow us to rule out low values of α by matching the observed residual RVs to the simulated residuals. This

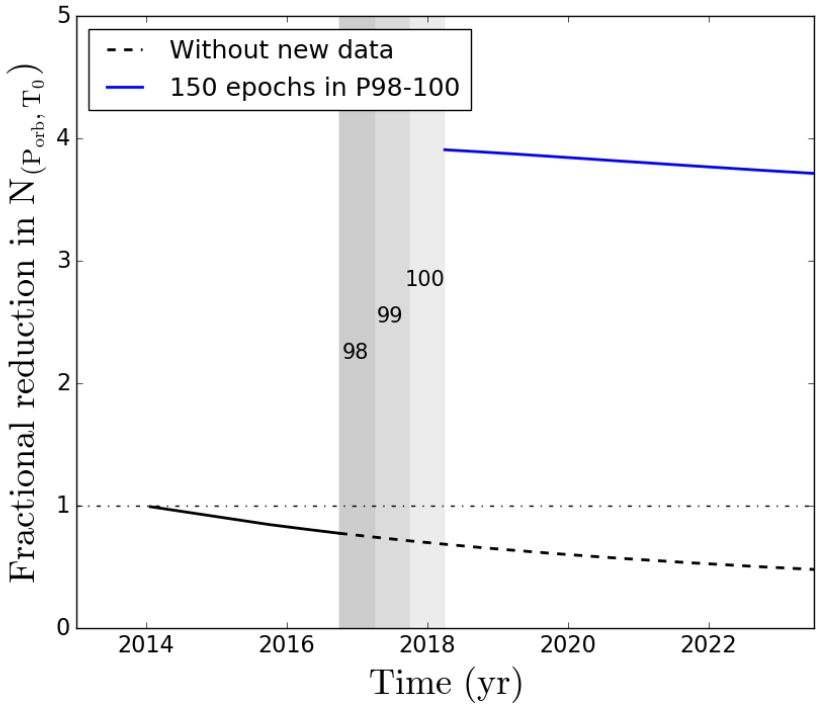

Figure 6.1: Impact of the quality of the ephemeris on GW searches during the A-LIGO era. The parameter uncertainties of the two principal orbital elements P_{orb} and T_0 sets the number of matched templates that need to be searched over in a GW signal search ($N_{P_{orb}T_0}$, see Watts et al. 2008). Our current ephemeris will continue to degrade in the absence of additional data (lowest black curve). The approved campaign (Period 98–101) will lead to a significant reduction in the template search space when compared to the scenario of taking no further data.

effort would directly improve the K-correction, and thereby improve the constraints on K_2 and K_1. Additionally, we will seek to exploit the more complete phase coverage of the UVES/VLT data to compute Doppler tomograms for the VLT spectra, which may provide further insights into the value of $K_{disc} \simeq K_1$. The determination of e will remain difficult due to our poor knowledge of both q and α. Lastly, we remark that the first detection of X-ray pulsations in Sco X-1 (although no pulsations have been observed so far for the brightest LMXBs) would offer the best prospects for constraining K_1 and e.

Table 6.1 contains an almost complete sample of suitably bright persistent LMXBs to apply the Bowen technique ($B \lesssim 19$). Although the significance of previously detected donor signal could all be confirmed in cases of low SNRs, it would be difficult to push the limit of observations to sources fainter than our 4σ limiting case (GR Mus) with existing 8-m class instruments that we were already using. Future improved instrumentation [e.g. for the European Extremely Large Telescope (E-ELT)] will be needed to expand the list

of persistent systems to include fainter sources and obtain more NS mass measurements through the same technique.

The recent application to the neutron star transient Aql X-1 unambiguously showed that the technique also works for transients during outburst. Furthermore, its role in the derivation of K_2 for the binary millisecond pulsar XTE J1814−338 has proved its value for RV studies of transients that are too faint in the optical after returning to quiescence (V $\gtrsim$ 23). The list of Bowen targets can be further expanded as new transient outbursts are detected and the associated optical counterparts can be identified, which might provide us with the opportunities to find stellar-mass BHs (e.g., in the newly discovered X-ray transient MAXI J1820+070; Kawamuro et al. 2018). As discussed earlier, the Bowen blend may not always be dominated by the donor, hence one should be careful to separate sharp donor features from spurious emission originating from the accretion flow and/or the hot spot. It is also anticipated that the donor may sometimes be completely shielded by the irradiation driven thick accretion disc (as is the case of Aql X-1 at some outburst stages). For these reasons, both careful scheduling of the observations (to ensure a good phase coverage) and rigorous data analyses are required to extract valid donor RVs of transient XRBs.

So far, effort has been devoted to constraining the statistical significance of sharp features in Doppler maps almost exclusively. A shortcut to a full interpretation of any reconstruction would be to compute Doppler tomography significance maps by, e.g., combining the Monte Carlo method with binning techniques. This kind of significance maps would allow us to identify all statistically significant features in Doppler maps, e.g., the hot spot, the accretion disc and spiral arms. Other options to compute significance maps have been suggested by Marsh (2001). Future works can also explore the possibilities of incorporating fitting to a constant entropy within the DOPPLER code, rather than using wrapper functions to adjust the target χ^2. Furthermore, new models of Doppler tomography using better suited regularisation statistics may be developed (see, e.g., Uemura et al. 2015), which would allow the better recovery of localised and sharp-edged features.

Appendix A

Sco X-1 radial velocity data

The radial velocity measurements and 1σ errors (before scaling by efac) from the WHT & VLT observations are provided here.

Table A.1: RVs of the Bowen emission components determined from 1999 WHT observations of Sco X-1.

Time (in HJD)	RV (km s^{-1})	σ_{RV} (km s^{-1})
2451358.41909639	-179.32357753997863	1.7887655867076997
2451358.42273047	-192.59813554683387	1.6319584692329798
2451358.42626039	-182.71765957787449	1.9255252479136395
2451358.4296167	-187.68502932604764	1.6514740901838307
2451358.43297301	-176.03491672416965	1.5464622482367556
2451358.43693115	-178.52529383022193	1.4337204445138918
2451358.44087771	-174.3721143199036	1.7426019537904371
2451358.44484742	-180.2670335196171	1.751455772011933
2451358.44877084	-173.55927352917288	2.0016638445677835
2451358.45276369	-178.3368868832502	1.73610630870413
2451358.46152483	-186.65935074133964	1.974146494343507
2451358.46563342	-182.6769658224224	1.845145896280009
2451358.47069104	-171.78994528933433	2.1853047899414957
2451358.47504267	-185.68658863119714	2.1986501891562638
2451358.48074841	-171.854723083292	2.282446655622299
2451358.484857	-177.9546564318956	3.1496588038037787
2451358.48898874	-168.32054743358495	2.832262537149703
2451358.49309733	-170.88441189543065	3.6363932640560295
2451358.49720592	-158.24524839921395	4.058645066804812
2451358.50130294	-160.29293116943694	4.834998800387911
2451358.50982103	-158.45384506925794	7.301697361946266
2451358.51391805	-143.7058547886292	5.828631260533574
2451358.51803821	-136.93442496059032	6.638401301407951
2451358.52213523	-139.74723887225704	4.603714698130966

2451358.52624382	-141.331548965671	6.702443323104921
2451358.53035241	-143.4473154533742	10.434918862209152
2451358.534461	-154.51258536305608	14.373146332380303
2451358.53855802	-109.95156807985364	5.918136163176673
2451358.54266661	-119.51709423935434	6.155433387114713
2451358.54678677	-139.4034786783923	6.0769081847710815
2451358.55336052	-121.68891006607457	6.886926933428025
2451358.55746911	-121.97160590846053	5.9749880032709415
2451358.56158927	-127.85962472900249	8.291739311030952
2451358.56569786	-108.81924049772785	4.11151379987681
2451358.56980645	-95.5052509419024	7.59012103228247
2451358.57391504	-85.62086339978875	4.21013096486311
2451358.57803521	-77.080641546129	10.473071068468405
2451358.5821438	-101.24872588808412	4.91236664103415
2451358.58625239	-92.96752199014999	6.477629586181052
2451358.59037256	-94.81335517777987	4.82290277045661
2451359.37794858	-88.60509007433909	6.852891749317955
2451359.38212661	-103.35933629549234	4.788586461455367
2451359.38633936	-56.28028902839704	5.932504140866603
2451359.39056368	-103.73823609228874	5.293274553740303
2451359.39477643	-78.34110530581667	3.4711078293352022
2451359.39895445	-65.39034310008093	4.516171465157892
2451359.40315563	-58.86968157610835	3.760613508107406
2451359.40732208	-74.83548275470915	3.050363587450783
2451359.4115001	-56.84524746275806	2.9274860476423115
2451359.41568971	-62.65475750698849	3.0064012957444164
2451359.42301572	-47.337674136164416	2.584488163971693
2451359.42715902	-64.0300128117396	2.2021817594455775
2451359.43133705	-61.40314401328301	2.6828133264857237
2451359.43556137	-64.03245179006507	1.9946858942673236
2451359.4397394	-57.464964561978064	2.714130752241687
2451359.44397529	-58.5347012688137	2.4038508328017496
2451359.44816489	-51.450196099444625	2.210645169986308
2451359.45236606	-44.620741908180214	2.516881312114599
2451359.45653252	-34.35367061893028	2.1745450275725684
2451359.4606874	-47.703601008601225	2.2375178021915065
2451359.46860366	-55.24351194254318	2.539166719173982
2451359.47280483	-58.9042750743483	2.1892823051110804
2451359.47701758	-51.568680443083885	1.9407280946581476
2451359.48123032	-48.46099182849304	1.8954812661458542
2451359.4854315	-31.573282788693	1.7700998979188365
2451359.48963267	-46.45889984296712	1.734613820347164
2451359.49379912	-34.39142245568707	1.617778309883489
2451359.497954	-30.264330508328417	1.4975445338611164
2451359.50215518	-29.08877135155309	1.620970942137191
2451359.50635635	-30.11679734687762	1.460770632685206

2451359.51325414	-43.810376624840416	1.2449006443616872
2451359.51740902	-50.89500779428558	1.3222810286091242
2451359.52163334	-49.705726230303824	1.2489820583724067
2451359.52581137	-47.365910400871876	1.12676897390791
2451359.53005883	-41.768549040124896	1.1409695347317625
2451359.53424843	-46.2651922477914	1.1871142242819748
2451359.53843803	-32.88386935424517	1.1720084432701365
2451359.54262763	-35.34912576891191	1.1740785551947208
2451359.54682881	-33.89497043921205	1.1856826239269536
2451359.5510184	-38.19148224872737	1.2570893888854855
2451359.55788148	-39.932175311113284	1.2880454698213575
2451359.56200164	-45.158211770012464	1.2586997806358147
2451359.56614494	-47.236192817811116	1.4949210960690704
2451359.57032297	-51.913691736973156	1.6711680788815342
2451359.5744547	-50.29661003549749	2.0040398875896956
2451359.57866745	-41.92954433867392	2.420384349176468
2451359.58286862	-46.591111024483425	2.8941714382907118
2451359.58704664	-46.180995948864144	2.2431684594858807
2451359.59125939	-50.833856160699405	3.3036363784798493
2451359.59540269	-48.23917089701192	2.4339852854309383
2451360.37903043	-42.005907046294666	2.447715143861326
2451360.3831853	-54.48909850822936	2.0207857574794623
2451360.38758322	-44.67892502701768	2.077128505260137
2451360.3916918	-52.53006701580291	1.785280799824437
2451360.39585825	-44.958543569808775	2.2218550823417202
2451360.40005942	-50.71721251314622	1.7009204060485257
2451360.40424901	-41.611022406149864	2.0982281907152993
2451360.40840388	-51.91068320326377	1.9151771300543374
2451360.41259348	-43.27313569598725	2.054249682104832
2451360.41679465	-52.78343657858661	1.919707700488969
2451360.42328736	-47.17866071534595	1.9148593966786087
2451360.42747695	-51.25660422680789	1.704374546597995
2451360.43163183	-47.64059760024713	2.0964154946224927
2451360.43579827	-51.236767137559575	1.9245014149042265
2451360.44004574	-40.78882917751592	2.337683888040163
2451360.44423533	-50.040682111897176	2.29165792686529
2451360.4483902	-46.51553087648496	2.645964988109522
2451360.45259137	-50.70844902324749	2.0616982860347233
2451360.45680411	-50.075630228508274	2.450505257232404
2451360.46097056	-55.541890651729666	2.588022824733305
2451360.46877107	-83.53067781912196	2.4753880997142876
2451360.47291437	-86.86389286124992	2.309085110568543
2451360.47710397	-78.20381046230273	2.772368180399077
2451360.48127041	-86.17458239641286	2.912209245947646
2451360.48551788	-77.76703990739888	2.613807252145208
2451360.48970747	-96.20454921820217	2.6462241006821023

2451360.49387392	-84.43746205950349	2.9829835785055017
2451360.49802879	-83.3894242174685	2.687759813086598
2451360.50220681	-83.00690347023712	3.0161413341825565
2451360.50638483	-94.83740784351944	3.0266475658932723
2451360.51346779	-102.53976208831946	4.056892194741313
2451360.51757637	-111.19714791912091	3.5572178278550033
2451360.52176596	-110.0409778982094	2.970146112528862
2451360.52596713	-110.7969150706746	2.84566085150961
2451360.53009886	-101.76916375244446	3.3258791430589207
2451360.53430002	-114.83943631638506	3.0181291891817645
2451360.53848962	-106.55900799868402	3.6812392239298974
2451360.54270236	-120.74019199983547	3.7403652065439896
2451360.54682251	-119.43832495229621	3.9543235289104
2451360.55102368	-121.52630009120023	4.886832512773695
2451360.55792146	-121.31260332777751	4.231955262678297
2451360.56205319	-126.01285422370255	2.9441111461395253
2451360.56623121	-119.39081017621847	3.7027305002672186
2451360.57044395	-127.65987591922809	3.5584334363274746
2451360.57458725	-132.42493289373417	4.142228950391537
2451360.57879999	-134.94411348081005	3.2488008565209245
2451360.58300116	-134.52626013230628	4.4825749586212496

Table A.2: RVs of the Bowen emission components determined from 2011 WHT observations of Sco X-1.

Time (in HJD)	RV (km s^{-1})	σ_{RV} (km s^{-1})
2455729.397	-146.87740943109296	4.073569029678792
2455729.404	-154.8003071767694	3.2844589036613208
2455729.407	-147.0735088122837	2.90658138148077
2455729.411	-151.4490326557727	2.651045790456662
2455729.415	-158.4242274916276	2.795732472908467
2455729.419	-154.49753254476977	3.571531635236099
2455729.422	-157.9277744772516	2.8881381695782027
2455729.426	-159.4019162933333	3.0712896093687636
2455729.43	-160.34009840148673	3.5325507054158654
2455729.434	-164.47891361876367	3.3013094697341265
2455729.437	-168.21207227226233	3.0654632943002813
2455729.441	-166.1231852942478	2.8840658277179503
2455729.445	-170.57209508513063	3.049507118022791
2455729.452	-165.69750732697835	3.1709172212912056
2455729.456	-172.09059987940861	2.6178718772164773
2455729.46	-176.13362211874264	2.766816276204085
2455729.463	-171.10772946449669	2.726984557907258
2455729.467	-176.49103695450873	2.7017144096224275

2455729.471	-180.06287551975646	2.2492431480686936
2455729.475	-175.95641055107157	2.1866043167711733
2455729.478	-183.93556154659362	2.6945626986834603
2455729.482	-178.41264942647027	2.536037962624975
2455729.486	-180.89363398856122	3.566889324011507
2455729.49	-185.27029856277596	3.124771411183089
2455729.493	-180.01036496121787	3.304349018498248
2455729.5	-180.37449101420717	2.649697237415323
2455729.504	-185.40485669580093	2.3035060490448114
2455729.508	-188.67009039621826	3.027206748549088
2455729.512	-183.47900281181361	2.982221482530709
2455729.515	-183.6732749698692	2.143872678844911
2455729.519	-184.59501826345985	2.279058516372073
2455729.523	-185.6021213320874	2.225860992200911
2455729.527	-182.5896756500669	2.4401773142109957
2455729.53	-181.581515940505	2.2494391232089734
2455729.534	-186.0241118597858	2.194722101977704
2455729.538	-181.23548475240005	2.78875804557675
2455729.542	-188.01978526862766	2.4412281885175138
2455729.549	-187.843762021991	1.8622814402817653
2455729.552	-185.67256184348108	2.224108474766914
2455729.556	-184.07519448174173	2.415864444783285
2455729.56	-183.67499173337958	2.0799585277468156
2455729.564	-180.89603279285402	2.2395871981081905
2455729.567	-177.48364100497133	2.431337097268692
2455729.571	-183.52220123844774	2.2880921317181353
2455729.575	-178.16733643938608	2.1720222781512857
2455729.579	-178.22709915906097	2.2021031113870495
2455729.582	-179.73562995373186	2.812315679224746
2455729.586	-175.6696170365939	2.9053370149938713
2455729.59	-176.83891023747367	3.1043066222825133
2455729.597	-173.97299752297198	3.2714644944466253
2455729.601	-176.01031062846602	2.495366709314814
2455729.605	-181.72462747677287	2.905920242161874
2455729.608	-181.0574331713542	2.5783204354174654
2455729.612	-168.22014682536104	3.3571668030772552
2455729.616	-170.91789806217497	2.8842674323593784
2455729.62	-173.44157030403915	3.2451903651647505
2455729.623	-173.69763533007978	3.2198212452157757
2455729.627	-170.97553665974786	4.02214471970566
2455729.631	-170.608118333059	3.3090665598379068
2455729.635	-166.13643073098177	4.571404051074238
2455729.638	-171.47002120709755	3.5652115337548937
2455729.646	-166.22668863644196	4.577824843505381
2455729.649	-165.2542355891471	4.782277269480112
2455729.653	-169.64559316774452	4.270796615507213

2455729.657	-159.24212546829457	4.464612157667118
2455729.661	-156.1692632698795	4.595633987271242
2455729.665	-157.7447980330643	5.676088730571976
2455729.669	-145.07436928996339	5.648318488906131
2455729.672	-150.57254143846933	12.240629663346887
2455730.392	-183.82024230077838	2.671144765858814
2455730.396	-176.21933486860414	2.783507279585622
2455730.4	-170.91040955856917	3.04111716298817
2455730.403	-176.06450531681588	2.842655231555172
2455730.407	-172.16831133155108	3.2943308634901536
2455730.411	-171.65168715619643	2.9251992352663816
2455730.415	-166.17393546988794	2.6357420324028253
2455730.418	-166.22929724795463	2.9909813921046267
2455730.422	-164.50580606178337	3.1522766412304217
2455730.426	-161.2943681193088	3.3061183432703927
2455730.43	-161.16613791767577	3.1393281437406384
2455730.434	-168.67230808574277	2.7910759456063947
2455730.439	-168.26342261113373	3.382923254097273
2455730.443	-164.55989470413067	3.0144762499139803
2455730.446	-153.6992987861219	2.833898247935647
2455730.45	-158.17905308007158	3.4382965859037355
2455730.454	-156.10724925942569	4.482480150481805
2455730.458	-157.30754992422723	3.237189698697484
2455730.461	-161.21590359343801	3.96492576227758
2455730.465	-150.56444198828333	5.252029044369113
2455730.469	-147.54894576054642	4.523155097527245
2455730.473	-139.78508171183256	4.864128900521067
2455730.477	-143.15019677398996	5.7804167295944096
2455730.48	-141.04430983155976	8.090037521296965
2455730.487	-135.02693907507185	7.154721260061829
2455730.491	-132.62785021456367	8.816807464584558
2455730.495	-122.27617439454221	11.768485803255192
2455730.498	-125.79653639297223	10.796419525097296
2455730.502	-127.8334185054836	24.920181491987883
2455730.506	-71.83908422106643	5.300379589974688
2455730.51	-79.01559923220313	7.701208983776551
2455730.513	-113.13413513457957	11.832934557367526
2455730.517	-113.98351739432121	9.750310989980633
2455730.521	-69.64285793666501	5.692321068155788
2455730.525	-112.324429417719	12.493384477447348
2455730.528	-109.1081486934998	44.939149200518976
2455730.535	-91.50496376589004	7.529256577480132
2455730.539	-107.08295401088466	7.597418738148943
2455730.542	-105.85514800422695	11.214878613698389
2455730.546	-51.1515401022418	6.960254200836717
2455730.55	-68.79501933550085	5.128307512077094

2455730.554	-93.21858143384652	7.54537772394684
2455730.557	-83.22385297004726	7.100320054056764
2455730.561	-110.98252582773573	12.635348103952193
2455730.565	-80.68826847801316	7.098100181988464
2455730.569	-77.11043382947214	8.819051408029264
2455730.572	-9.030927614723215	6.088515812115012
2455730.576	-60.827393423122416	10.344027226392603
2455730.582	-63.691086692129765	6.071247886748823
2455730.585	-37.07791899486481	4.155375004482444
2455730.589	-66.57893294033319	6.765853203002165
2455730.593	-7.9080455500888585	6.718415724190799
2455730.597	-42.11985167199022	5.137393348939228
2455730.6	-45.74020231051761	5.778653377428805
2455730.604	-64.81289252086361	4.820307180363058
2455730.608	-62.264401123296935	4.299336653381478
2455731.424	-50.87696402676037	4.561616054045585
2455731.428	-51.850800919658056	3.3540953282186106
2455731.432	-46.38857282071308	3.5036220890210212
2455731.435	-43.081196597329665	2.992255760072969
2455731.439	-50.145886838825014	2.796771933362261
2455731.443	-54.60865331969531	2.8096700294851997
2455731.447	-53.10384677494798	2.4046048896548835
2455731.45	-50.60211508015486	2.3416818474232306
2455731.454	-50.24086786522095	2.32280823317953
2455731.458	-51.00244193081066	2.263940899222067
2455731.462	-53.59638387774971	2.6349818140694574
2455731.465	-52.79890190621352	2.4689501734917165
2455731.471	-55.73345466026779	3.3307984566646622
2455731.475	-62.252932424329664	3.5889011234249906
2455731.479	-48.14408152169039	3.701953524954634
2455731.483	-49.53675134057154	3.677014461651283
2455731.486	-47.844015715811636	4.145844917057172
2455731.49	-46.31548129756791	4.053835601096258
2455731.494	-43.51620175665727	6.919598561273762
2455731.498	-42.07185953108206	4.54210180877506
2455731.501	-48.48046028926367	4.190361192182077
2455731.505	-50.68403555715211	6.0135822093326965
2455731.509	-43.6213599349844	3.9266439623663016
2455731.513	-36.64943273327174	5.449056620583096
2455731.519	-37.680988390164615	7.105015329772961
2455731.522	-41.53230436167464	6.631901720954147
2455731.526	-29.660507159157763	9.512762711431382
2455731.53	-41.139719625548516	7.28836064855092
2455731.534	-46.42722236047814	7.8782394524650545
2455731.537	-56.56356501071874	7.279797089537688
2455731.541	-51.63590815009873	6.5823712339003535

2455731.545	-47.14939071726588	5.986068303912075

Table A.3: RVs of the Bowen emission components determined from 2011 VLT observations of Sco X-1.

Time (in HJD)	RV (km s^{-1})	σ_{RV} (km s^{-1})
2455710.786702	-138.73564599554598	2.3647932841913115
2455710.795621	-136.5444973904921	2.3350134536547724
2455710.804543	-132.47530080305563	2.7530837994908794
2455710.813465	-124.30050868097761	2.7226647231852814
2455811.542501	-151.59323874492	1.196764727327043
2455811.551421	-148.51106677566034	1.3649756824085935
2455811.560339	-140.6970678774696	1.512607054109777
2455811.56926	-135.81812679056668	1.7309089637068507
2455796.587935	-145.93891129092793	1.297716648605742
2455796.596856	-142.71727848951403	1.8151250334362226
2455796.605778	-135.88732841478037	1.7955979265941853
2455796.6147002	-133.3329246036553	2.158694183918057
2455796.550618	-168.33544241448104	1.1957522922817219
2455796.559537	-163.73760462521804	1.284040264615416
2455796.568454	-156.1562329457953	1.2849511328068488
2455796.5773709	-148.38027819192087	1.1522484405843767
2455796.512413	-181.35019235461775	0.882914791560703
2455796.521332	-178.63880619645727	0.8632224647007676
2455796.530255	-176.60597497331486	1.0586786331817688
2455796.539174	-172.1663413495952	1.0778881817692043
2455784.4839984	-133.3765366680464	0.520787529178209
2455784.492918	-141.99390064067887	0.5306128986610689
2455784.501841	-143.58779970549173	0.5290281053903699
2455784.510759	-146.53567977821135	0.5535653897429463
2455776.597158	-125.81185600227003	0.8251438368872807
2455776.606077	-134.77619919441202	0.7821022467529893
2455776.6150007	-134.83013823020556	0.7902080968930794
2455776.623925	-143.8555110698082	0.7607086867659254
2455776.5586505	-104.87273363175235	0.7541251902630118
2455776.567568	-110.15567275476369	0.8036994187407183
2455776.5764902	-114.63099390425569	0.8414374632104125
2455776.585414	-120.93932076280123	0.8210342480220949
2455756.605669	-57.78419213773975	0.4874936543134999
2455756.614588	-54.83027141734282	0.45198147574614217
2455756.623512	-50.8956681501265	0.4135210961298332
2455756.632429	-48.964054578440674	0.393592730928509
2455756.5673701	-75.6598663489728	0.6532125981742745
2455756.57629	-70.85816786820811	0.6437204907219477

2455756.585211	-67.05158737354456	0.7834861276233059
2455756.594132	-62.88779892263268	0.6880039334170427
2455717.773151	-184.64499511102974	0.8086072500534954
2455717.782074	-181.47991086143114	0.7748775823876929
2455717.790993	-179.44288859824204	0.811584808059858
2455717.799912	-175.6468000203424	0.8599248581574961

Appendix B

Irradiation modelling

Using the *lprofile* code (within the LCURVE package) provided by T. Marsh (e.g. Southworth et al. 2009; Parsons et al. 2010), we started by generating phase-resolved synthetic line profiles from an irradiated donor for all possible α-values and different mass ratios between the newly determined range of q of 0.22 – 0.76. In order to derive the most appropriate $V\sin i_{\rm cor}$ factors, limb darkening effects were not included in the simulations for the optically thin regime examined here. Other key input parameters representing the instrumental setup (e.g., the exposure length and the FWHM spectral resolution) were fixed at values that match our UVES/VLT observations.

Next, we fitted a 1D Gaussian profile to the model data sets and measured the widths of the emission components as a function of orbital phase, which always exhibit a single peak at phase 0.5 for all possible combinations of α and q (see Figure B.1). Therefore, we take the width measurement at phase 0.5 (after correction for instrumental broadening) as the estimate for the observed $V\sin i_{\rm em}$ that leads to the largest correction factor (i.e. smallest deviation). Since both q and true K_2 are known, the true $V\sin i$ can be calculated using equation (1.18) and hence the ratio of $\frac{V\sin i_{\rm em}}{V\sin i}$ can be determined for each irradiation model.

Meanwhile, by establishing synthetic RV curves (through 1D Gaussian fits to the line profiles), it can clearly be seen that the RVs of the donor emission may deviate significantly from a sinusoid at high mass ratios or low disc opening angles (more details in Section 5.4.3). We reconstructed synthetic Doppler maps to extract $\rm K_{em}$ (by computing the centroid of the donor emission spot; see Section 5.3.2), from which we could independently estimate $\rm K_{cor} = \frac{K_{em}}{K_2}$, to offer a comparison to MCM05.

Fig. B.2 presents example results of our simulations of $V\sin i_{\rm cor}$ (black) and $\rm K_{cor}$ (blue) versus q (for the cases of $\alpha = 0°$ and $4°$), with the K-correction of MCM05 produced by a different binary code overplotted (as blue dashed lines) for comparison. One can see that both factors are always significantly below unity, and this can be exploited to derive

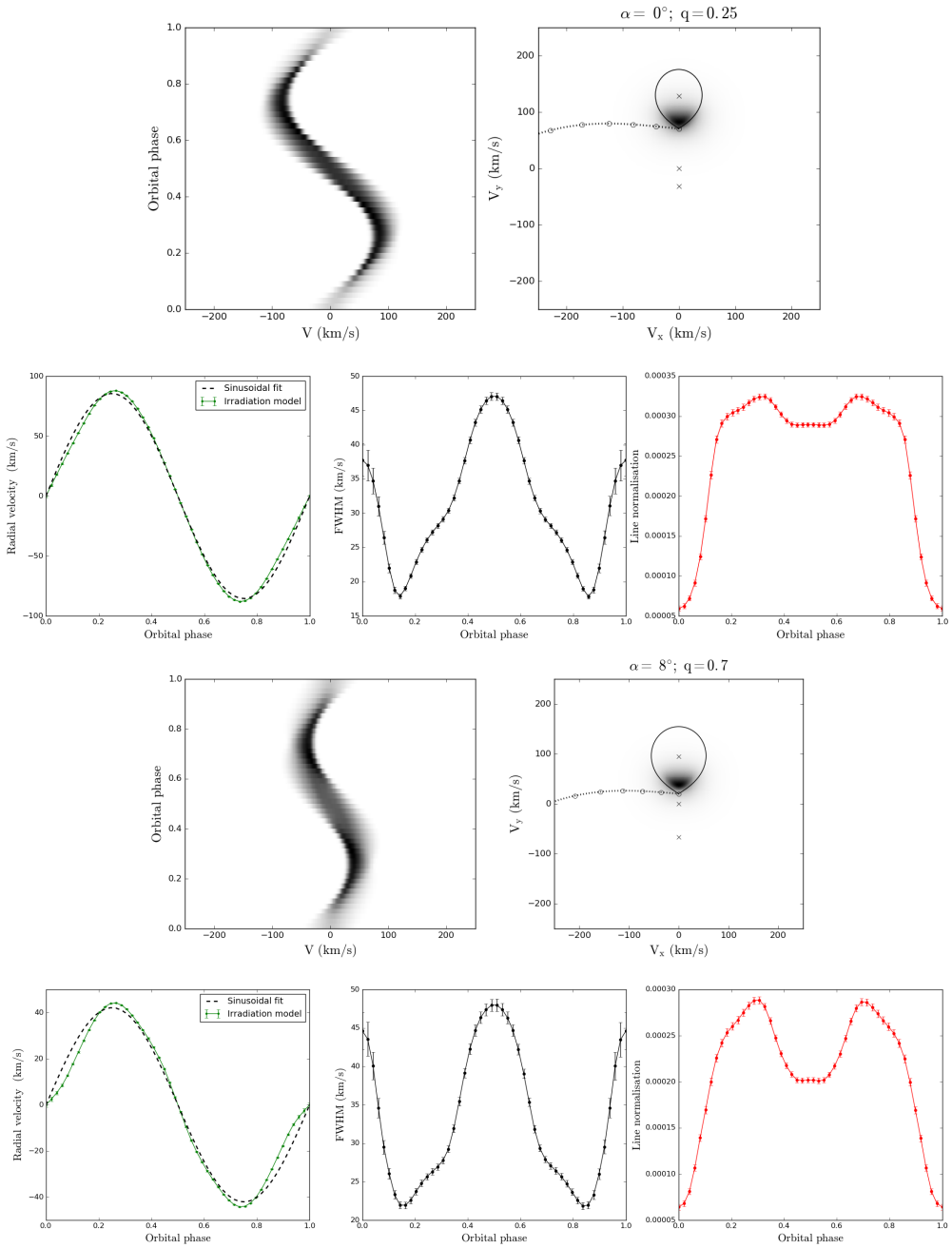

Figure B.1: Example irradiation models with two different combinations of α and q. **Top:** example synthetic data (*left*) and the corresponding reconstructed Doppler tomograms (*right*). **Bottom:** synthetic RV curves (*bottom left*), widths of the emission component (*bottom middle*) and normalization (*bottom right*) as a function of orbital phase obtained from 1D Gaussian fits to the line profiles. The measured widths always exhibit a single peak at phase 0.5 for all possible combinations of α and q. Note also that the RVs of the donor emission may deviate significantly from a sinusoid.

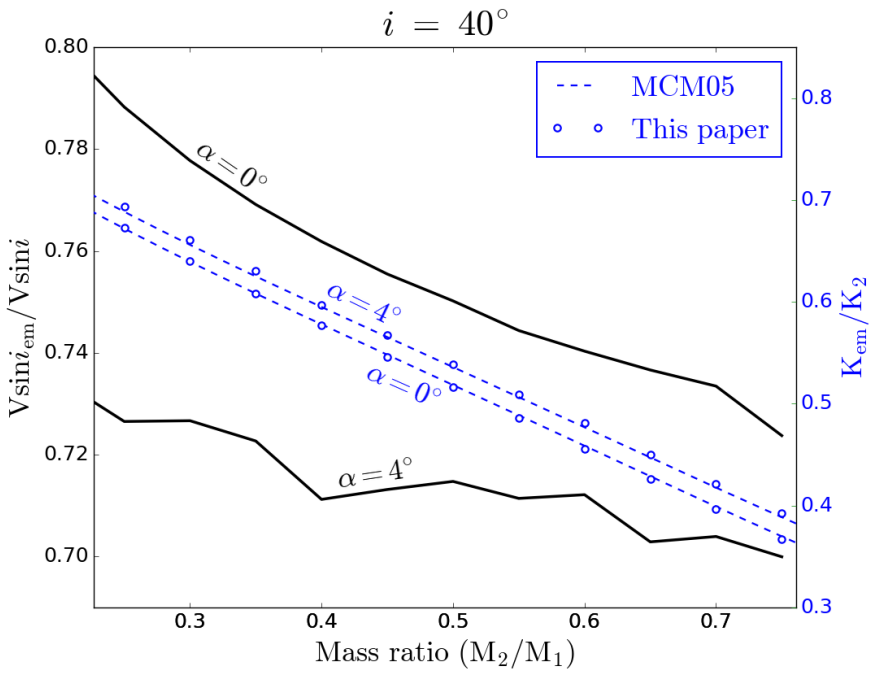

Figure B.2: Plot of $V\sin i$– (black) and K-correction (blue) determined from our simulations (for the low inclination case of i = 40°) as a function of q for α = 0° and 4°, with the fourth-order polynomial models provided in MCM05 overplotted (as blue dashed lines) for comparison. The minimum $V\sin i_{cor}$-correction (α = 0°) should be applied to yield the most stringent lower limits of the system parameters (q, K_1 and K_2) of Sco X-1.

Table B.1: The $V\sin i$-correction factor for $\alpha = 0°$ and $i = 40°$.

Mass ratio	$V\sin i$-correction
0.25.....	0.78827
0.3.....	0.77774
0.35.....	0.76912
0.4.....	0.76185
0.45.....	0.75547
0.5.....	0.75019
0.55.....	0.74437
0.6.....	0.74032
0.65.....	0.73663
0.7.....	0.73346
0.75.....	0.72375

firmer limits. The K-correction decreases smoothly with both α and q, and has already been approximated by a set of fourth-order polynomials by MCM05 for α from 0° to 18° in steps of 2°. For small disc opening angles ($\alpha \leq 4°$), our solutions for K_{cor} coincide almost exactly with the numerical models of MCM05 (as shown in Fig. B.2). The results were also in good agreement (within 3.5 per cent) for $\alpha > 4°$. The $V\sin i$-correction factor, on the other hand, tends to decrease as α increases; yet at any given α-angle the estimated value of $V\sin i_{cor}$ does not vary smoothly with q, fluctuating increasingly randomly with increasing α. Thus the minimum $V\sin i_{cor}$-correction ($\alpha = 0°$; provided in Table B.1) can be applied to yield the most stringent lower limits of the system parameters.

Bibliography

Abbott, B., et al., 2007, Phys. Rev. D, 76, 082001

Abbott, B. P., et al., 2016, Physical Review Letters, 116, 061102

Abbott, B. P., et al., 2017a, Physical Review Letters, 118, 121102

Abbott, B. P., et al., 2017b, Physical Review Letters, 119, 161101

Abbott, B. P., et al., 2017c, ApJ, 847, 47

Alpar, M. A., Cheng, A. F., Ruderman, M. A., Shaham, J., 1982, Nat, 300, 728

Andersson, N., 1998, ApJ, 502, 708

Andersson, N., 2003, Classical and Quantum Gravity, 20, R105

Antoniadis, J., et al., 2013, 340, 448

Archibald, A. M., et al., 2009, 324, 1411

Arzoumanian, Z., 1995, Radio Observations of Binary Pulsars: Clues to Binary Evolution and Tests of General Relativity., Ph.D. thesis, PRINCETON UNIVERSITY.

Augusteijn, T., van der Hooft, F., de Jong, J. A., van Kerkwijk, M. H., van Paradijs, J., 1998, A&A, 332, 561

Backer, D. C., Kulkarni, S. R., Heiles, C., Davis, M. M., Goss, W. M., 1982, Nat, 300, 615

Baglio, M. C., D'Avanzo, P., Muñoz-Darias, T., Breton, R. P., Campana, S., 2013, 559, A42

Barnes, A. D., Casares, J., Cornelisse, R., Charles, P. A., Steeghs, D., Hynes, R. I., O'Brien, K., 2007, 380, 1182

Bassa, C. G., et al., 2014, 441, 1825

Beer, M. E., Podsiadlowski, P., 2002, 331, 351

Belczynski, K., Wiktorowicz, G., Fryer, C. L., Holz, D. E., Kalogera, V., 2012, ApJ, 757, 91

Bhattacharyya, S., Strohmayer, T. E., Miller, M. C., Markwardt, C. B., 2005, ApJ, 619, 483

Bildsten, L., 1998, ApJ Lett., 501, L89

Bradshaw, C. F., Fomalont, E. B., Geldzahler, B. J., 1999, ApJ Lett., 512, L121

Brandt, N., Podsiadlowski, P., 1995, 274, 461

Breton, R. P., et al., 2013, ApJ, 769, 108

Burderi, L., Di Salvo, T., D'Antona, F., Robba, N. R., Testa, V., 2003, 404, L43

Burderi, L., Di Salvo, T., Riggio, A., Papitto, A., Iaria, R., D'Aì, A., Menna, M. T., 2010, 515, A44

Campana, S., et al., 2004, ApJ Lett., 614, L49

Casares, J., Charles, P. A., 1994, 271, L5

Casares, J., Charles, P. A., Naylor, T., 1992, Nat, 355, 614

Casares, J., Steeghs, D., Hynes, R. I., Charles, P. A., O'Brien, K., 2003, ApJ, 590, 1041

Casares, J., Steeghs, D., Hynes, R. I., Charles, P. A., Cornelisse, R., O'Brien, K., 2004, in Tovmassian, G., Sion, E., eds., Revista Mexicana de Astronomia y Astrofisica Conference Series, vol. 20 of *Revista Mexicana de Astronomia y Astrofisica Conference Series*, p. 21

Casares, J., Ribó, M., Ribas, I., Paredes, J. M., Martí, J., Herrero, A., 2005, 364, 899

Casares, J., Cornelisse, R., Steeghs, D., Charles, P. A., Hynes, R. I., O'Brien, K., Strohmayer, T. E., 2006, 373, 1235

Casares, J., Jonker, P. G., Israelian, G., 2017, X-Ray Binaries, p. 1499

Casella, P., Altamirano, D., Patruno, A., Wijnands, R., van der Klis, M., 2008, ApJ Lett., 674, L41

Chakrabarty, D., Morgan, E. H., Muno, M. P., Galloway, D. K., Wijnands, R., van der Klis, M., Markwardt, C. B., 2003, Nat, 424, 42

Cook, G. B., Shapiro, S. L., Teukolsky, S. A., 1994, ApJ Lett., 423, L117

Corbet, R. H. D., Thorstensen, J. R., Charles, P. A., Menzies, J. W., Naylor, T., Smale, A. P., 1986, 222, 15P

Coriat, M., Fender, R. P., Dubus, G., 2012, 424, 1991

Cornelisse, R., Casares, J., Steeghs, D., Barnes, A. D., Charles, P. A., Hynes, R. I., O'Brien, K., 2007a, 375, 1463

Cornelisse, R., Steeghs, D., Casares, J., Charles, P. A., Barnes, A. D., Hynes, R. I., O'Brien, K., 2007b, 380, 1219

Cornelisse, R., Steeghs, D., Casares, J., Charles, P. A., Shih, I. C., Hynes, R. I., O'Brien, K., 2007c, 381, 194

Cornelisse, R., Casares, J., Muñoz-Darias, T., Steeghs, D., Charles, P., Hynes, R., O'Brien, K., Barnes, A., 2008, in Bandyopadhyay, R. M., Wachter, S., Gelino, D., Gelino, C. R., eds., A Population Explosion: The Nature & Evolution of X-ray Binaries in Diverse Environments, vol. 1010 of *American Institute of Physics Conference Series*, p. 148

Courvoisier, T. J.-L., Parmar, A. N., Peacock, A., Pakull, M., 1986, ApJ, 309, 265

Cutler, C., 2002, Phys. Rev. D, 66, 084025

D'Avanzo, P., Campana, S., Covino, S., Israel, G. L., Stella, L., Andreuzzi, G., 2007, 472, 881

D'Avanzo, P., Campana, S., Casares, J., Covino, S., Israel, G. L., Stella, L., 2009, 508, 297

de Jong, J. A., van Paradijs, J., Augusteijn, T., 1996, 314, 484

de Martino, D., et al., 2014, 444, 3004

Demorest, P. B., Pennucci, T., Ransom, S. M., Roberts, M. S. E., Hessels, J. W. T., 2010, Nat, 467, 1081

Done, C., Gierliński, M., 2003, 342, 1041

Efron, B., Tibshirani, R. J., 1993, An Introduction to the Bootstrap, Chapman & Hall, New York, NY

Eggleton, P. P., 1983, ApJ, 268, 368

Farr, W. M., Sravan, N., Cantrell, A., Kreidberg, L., Bailyn, C. D., Mandel, I., Kalogera, V., 2011, ApJ, 741, 103

Fomalont, E. B., Geldzahler, B. J., Bradshaw, C. F., 2001, ApJ, 558, 283

Fonseca, E., et al., 2016, ArXiv e-prints

Foreman-Mackey, D., Hogg, D. W., Lang, D., Goodman, J., 2013, PASP, 125, 306

Frank, J., King, A., Raine, D. J., 2002, Accretion Power in Astrophysics: Third Edition

Friedman, J. L., Ipser, J. R., Parker, L., 1986, ApJ, 304, 115

Fryer, C. L., Kalogera, V., 2001, ApJ, 554, 548

Galloway, D. K., Muno, M. P., Hartman, J. M., Psaltis, D., Chakrabarty, D., 2008, 179, 360

Galloway, D. K., Premachandra, S., Steeghs, D., Marsh, T., Casares, J., Cornelisse, R., 2014, ApJ, 781, 14

Giacconi, R., Gursky, H., Paolini, F. R., Rossi, B. B., 1962, Physical Review Letters, 9, 439

Giles, A. B., Hill, K. M., Strohmayer, T. E., Cummings, N., 2002, ApJ, 568, 279

Gomez, S., Mason, P. A., Robinson, E. L., 2015, ApJ, 809, 9

Gottlieb, E. W., Wright, E. L., Liller, W., 1975, ApJ Lett., 195, L33

Gray, D. F., 1992, The observation and analysis of stellar photospheres.

Griffiths, R. E., Gursky, H., Schwartz, D. A., Schwarz, J., Bradt, H., Doxsey, R. E., Charles, P. A., Thorstensen, J. R., 1978, Nat, 276, 247

Hartman, J. M., et al., 2008, ApJ, 675, 1468

Hasinger, G., van der Klis, M., 1989, 225, 79

Haskell, B., Jones, D. I., Andersson, N., 2006, 373, 1423

Haskell, B., Samuelsson, L., Glampedakis, K., Andersson, N., 2008, 385, 531

Heida, M., Jonker, P. G., Torres, M. A. P., Chiavassa, A., 2017, ApJ, 846, 132

Heinz, S., Nowak, M. A., 2001, 320, 249

Hellier, C., Mason, K. O., 1989, 239, 715

Homer, L., Charles, P. A., Chakrabarty, D., van Zyl, L., 2001, 325, 1471

Horne, K., 1986, PASP, 98, 609

Horne, K., 1994, in Gondhalekar, P. M., Horne, K., Peterson, B. M., eds., Reverberation Mapping of the Broad-Line Region in Active Galactic Nuclei, vol. 69 of *Astronomical Society of the Pacific Conference Series*, p. 23

Hynes, R. I., Steeghs, D., Casares, J., Charles, P. A., O'Brien, K., 2003, ApJ Lett., 583, L95

Jiménez-Ibarra, F., Muñoz-Darias, T., Wang, L., Casares, J., Mata Sánchez, D., Steeghs, D., Armas Padilla, M., Charles, P. A., 2017, ArXiv e-prints

Jiménez-Ibarra, F., Muñoz-Darias, T., Wang, L., Casares, J., Mata Sánchez, D., Steeghs, D., Armas Padilla, M., Charles, P. A., 2018, 474, 4717

Jonker, P. G., van der Klis, M., 2001, ApJ Lett., 553, L43

Jonker, P. G., et al., 2003, 344, 201

Kalogera, V., Webbink, R. F., 1998, ApJ, 493, 351

Kawamuro, T., et al., 2018, The Astronomer's Telegram, 11399

King, A. R., Kolb, U., Burderi, L., 1996, ApJ Lett., 464, L127

King, A. R., Frank, J., Kolb, U., Ritter, H., 1997a, ApJ, 484, 844

King, A. R., Kolb, U., Szuszkiewicz, E., 1997b, ApJ, 488, 89

Krauss, M. I., et al., 2005, ApJ, 627, 910

Lasky, P. D., 2015, Proc. Astron. Soc. Aust., 32, e034

Lasota, J.-P., 2001, 45, 449

Lattimer, J. M., 2012, Annual Review of Nuclear and Particle Science, 62, 485

Lattimer, J. M., Prakash, M., 2004, Science, 304, 536

Lattimer, J. M., Prakash, M., 2007, 442, 109

Leaci, P., Prix, R., 2015, Phys. Rev. D, 91, 102003

Lewin, W. H. G., van Paradijs, J., Taam, R. E., 1993, Space Sci. Rev., 62, 223

Lewin, W. H. G., van Paradijs, J., Taam, R. E., 1995, X-ray Binaries, 175

Linares, M., Shahbaz, T., Casares, J., 2018, ArXiv e-prints

Longa-Peña, P., Steeghs, D., Marsh, T., 2015, 447, 149

Manser, C. J., et al., 2016, 455, 4467

Markwardt, C. B., Swank, J. H., 2003, 8144

Markwardt, C. B., Strohmayer, T. E., Swank, J. H., 2003, The Astronomer's Telegram, 164

Marquardt, D. W., 1963, SIAM Journal on Applied Mathematics, 11, 431

Marsh, T. R., 2001, in Boffin, H. M. J., Steeghs, D., Cuypers, J., eds., Astrotomography, Indirect Imaging Methods in Observational Astronomy, vol. 573 of *Lecture Notes in Physics, Berlin Springer Verlag*, p. 1

Marsh, T. R., Horne, K., 1988, 235, 269

Marsh, T. R., Robinson, E. L., Wood, J. H., 1994, 266, 137

Mason, K. O., Middleditch, J., Nelson, J. E., White, N. E., Seitzer, P., Twohy, I. R., Hunt, L. K., 1980, ApJ Lett., 242, L109

Mata Sánchez, D., Muñoz-Darias, T., Casares, J., Steeghs, D., Ramos Almeida, C., Acosta Pulido, J. A., 2015, 449, L1

Mata Sánchez, D., Muñoz-Darias, T., Casares, J., Jiménez-Ibarra, F., 2017, 464, L41

Meadors, G. D., Goetz, E., Riles, K., 2016, Classical and Quantum Gravity, 33, 105017

Meadors, G. D., Goetz, E., Riles, K., Creighton, T., Robinet, F., 2017, Phys. Rev. D, 95, 042005

Melatos, A., Payne, D. J. B., 2005, ApJ, 623, 1044

Messenger, C., et al., 2015, Phys. Rev. D, 92, 023006

Meyer, F., Meyer-Hofmeister, E., 1982, 106, 34

Motch, C., Pedersen, H., Courvoisier, T. J.-L., Beuermann, K., Pakull, M. W., 1987, ApJ, 313, 792

Muñoz-Darias, T., Casares, J., Martínez-Pais, I. G., 2005, ApJ, 635, 502

Muñoz-Darias, T., Casares, J., O'Brien, K., Steeghs, D., Martínez-Pais, I. G., Cornelisse, R., Charles, P. A., 2009, 394, L136

Nice, D. J., Sayer, R. W., Taylor, J. H., 1996, ApJ Lett., 466, L87

Orosz, J. A., Bailyn, C. D., 1997, ApJ, 477, 876

Osaki, Y., 1974, PASJ, 26, 429

Paczyński, B., 1967, 17, 287

Paczyński, B., 1971, ARA&A, 9, 183

Papaloizou, J., Pringle, J. E., 1978, 184, 501

Papitto, A., di Salvo, T., Burderi, L., Menna, M. T., Lavagetto, G., Riggio, A., 2007, MNRAS, 375, 971

Papitto, A., et al., 2013, Nat, 501, 517

Parsons, S. G., Marsh, T. R., Copperwheat, C. M., Dhillon, V. S., Littlefair, S. P., Gänsicke, B. T., Hickman, R., 2010, 402, 2591

Patruno, A., 2010, ApJ, 722, 909

Patruno, A., Watts, A. L., 2012, ArXiv e-prints

Pedersen, H., van Paradijs, J., Lewin, W. H. G., 1981, Nat, 294, 725

Rappaport, S., Verbunt, F., Joss, P. C., 1983, ApJ, 275, 713

Riles, K., 2017, Modern Physics Letters A, 32, 1730035

Roberts, M. S. E., 2011, in Burgay, M., D'Amico, N., Esposito, P., Pellizzoni, A., Possenti, A., eds., American Institute of Physics Conference Series, vol. 1357 of *American Institute of Physics Conference Series*, p. 127

Roy, J., et al., 2015, ApJ Lett., 800, L12

Sammut, L., Messenger, C., Melatos, A., Owen, B. J., 2014, Phys. Rev. D, 89, 043001

Sanford, P. W., Ives, J. C., Bell Burnell, S. J., Mason, K. O., Murdin, P., 1975, Nat, 256, 109

Schneider, D. P., Young, P., 1980, ApJ, 238, 946

Shafter, A. W., 1985, in Lamb, D. Q., Patterson, J., eds., Cataclysmic Variables and Low-Mass X-ray Binaries, vol. 113 of *Astrophysics and Space Science Library*, p. 355

Shahbaz, T., Ringwald, F. A., Bunn, J. C., Naylor, T., Charles, P. A., Casares, J., 1994, 271, L10

Skilling, J., Bryan, R. K., 1984, 211, 111

Smale, A. P., Corbet, R. H. D., 1991, ApJ, 383, 853

Southworth, J., Hickman, R. D. G., Marsh, T. R., Rebassa-Mansergas, A., Gänsicke, B. T., Copperwheat, C. M., Rodríguez-Gil, P., 2009, 507, 929

Stappers, B. W., et al., 2014, ApJ, 790, 39

Steeghs, D., 2003a, 344, 448

Steeghs, D., 2003b, 8155

Steeghs, D., Casares, J., 2002, ApJ, 568, 273

Steeghs, D., McClintock, J. E., Parsons, S. G., Reid, M. J., Littlefair, S., Dhillon, V. S., 2013, ApJ, 768, 185

Strohmayer, T. E., Markwardt, C. B., 2002, ApJ, 577, 337

Strohmayer, T. E., Markwardt, C. B., Swank, J. H., in't Zand, J., 2003, ApJ Lett., 596, L67

Swank, J. H., Becker, R. H., Boldt, E. A., Holt, S. S., Pravdo, S. H., Serlemitsos, P. J., 1977, ApJ Lett., 212, L73

Tauris, T. M., van den Heuvel, E. P. J., 2006, Formation and evolution of compact stellar X-ray sources, p. 623

Thorstensen, J., Charles, P., Bowyer, S., 1978, ApJ Lett., 220, L131

Tout, C. A., Pols, O. R., Eggleton, P. P., Han, Z., 1996, 281, 257

Uemura, M., Kato, T., Nogami, D., Mennickent, R., 2015, PASJ, 67, 22

Ushomirsky, G., Cutler, C., Bildsten, L., 2000, 319, 902

van Kerkwijk, M. H., van Paradijs, J., Zuiderwijk, E. J., 1995, 303, 497

van Paradijs, J., 1998, in Buccheri, R., van Paradijs, J., Alpar, A., eds., NATO Advanced Science Institutes (ASI) Series C, vol. 515 of *NATO Advanced Science Institutes (ASI) Series C*, p. 279

van Paradijs, J., White, N., 1995, ApJ Lett., 447, L33

van Paradijs, J., van der Klis, M., Pedersen, H., 1988, 76, 185

van Spaandonk, L., Steeghs, D., Marsh, T. R., Torres, M. A. P., 2010, 401, 1857

Verbunt, F., 1982, Space Sci. Rev., 32, 379

Wade, R. A., Horne, K., 1988, ApJ, 324, 411

Wagoner, R. V., 1984, ApJ, 278, 345

Wang, L., Steeghs, D., Casares, J., Charles, P. A., Muñoz-Darias, T., Marsh, T. R., Hynes, R. I., O'Brien, K., 2017, 466, 2261

Watson, C. A., Dhillon, V. S., 2001, 326, 67

Watts, A. L., Strohmayer, T. E., Markwardt, C. B., 2005, ApJ, 634, 547

Watts, A. L., Krishnan, B., Bildsten, L., Schutz, B. F., 2008, 389, 839

Whelan, J. T., Sundaresan, S., Zhang, Y., Peiris, P., 2015, Phys. Rev. D, 91, 102005

White, N. E., Holt, S. S., 1982, ApJ, 257, 318

White, N. E., Marshall, F. E., 1984, ApJ, 281, 354

White, N. E., van Paradijs, J., 1996, ApJ Lett., 473, L25

Wijnands, R., van der Klis, M., 1998, Nat, 394, 344

Wolszczan, A., 1991, Nat, 350, 688

Wu, K., Soria, R., Hunstead, R. W., Johnston, H. M., 2001, 320, 177